Effects of Aspect Ratio on Flow Characteristics on Free Surface-mounted Rectangular Cylinders

By

Kwasi Hyiah Agyei-Agyemang

A Thesis Submitted to the Faculty of Graduate Studies of The University of Manitoba in Partial Fulfillment of the Requirements of the Degree of

MASTER OF SCIENCE

Department of Mechanical Engineering

University of Manitoba

Winnipeg

Abstract

The turbulent flow characteristics around free surface-mounted rectangular cylinders of different streamwise aspect ratios (AR = 1, 2, 2.5, 3, 4, 5, and 8 denoted as AR1, AR2, AR2.5, AR3, AR4, AR5, and AR8, respectively) at a Reynolds number based on the freestream velocity and cylinder height, Re = 11100, were investigated experimentally using a time-resolved particle image velocimetry system. The results reveal distinct flow behaviors for different aspect ratios. The separated shear layer is shed directly into the wake for AR1, while AR2 and AR2.5 exhibits intermittent reattachment on the cylinder and direct shedding into the wake. However, for AR ≥ 3 cylinders, the separated shear layer reattaches onto the cylinder and is later shed into the wake after subsequent separation from the trailing edge of the cylinder. Comparative analysis with previous studies on rectangular cylinders in uniform flow and wall-mounted conditions demonstrates similarities in reattachment behavior on the cylinder to uniform flow cases and wake reattachment mechanism akin to wall-mounted cylinders subjected to a thin turbulent boundary layer. The Reynolds stresses, turbulence production, and vortex shedding patterns examined with frequency spectra and proper orthogonal decomposition of velocity fluctuations exhibit significant dependence on streamwise aspect ratio.

Acknowledgements

I thank the Lord God Almighty for grace and guidance throughout my master's program. I would like to extend my appreciation to my academic supervisor, Prof. Mark F. Tachie, for his enormous support, guidance, encouragement, patience, and for all his efforts that contributed to my achievements during my program. I am also deeply grateful to my academic co-supervisor, Dr. Ebenezer Essel for his sacrifices, support, and guidance. Special thanks to Mr. Sedem Kumahor, and all my colleagues within the research group for their love, friendship, encouragement, and invaluable input throughout the program. I would also like to acknowledge the technical support by Dave Tataryn throughout the experiments.

To my parents, Prof. Anthony Agyei-Agyemang, and Mrs. Elizabeth Agyei-Agyemang, and my brothers Kwabena Adubofour Agyei-Agyemang and Kwabena Agyei-Agyemang, thank you for your support, love, guidance since childhood, and most importantly your prayers. A big thank you to Gloria Ayumu and all my friends and loved ones for their support in every aspect of my life.

Table of Contents

Abstract i

Acknowledgements ii

List of Tables v

List of Figures vi

Nomenclature x

1. Introduction 1

  1.1 Background and Motivation 1
  1.2 Thesis Outline 5

2. Literature Review 6

  2.1 Literature Review 6
    2.1.1 Uniform flow 6
    2.1.2 Wall-mounted cylinder 11
    2.1.3 Semi-submerged cylinder 14
  2.2 Objective 15

3. Experimental Setup and Measurement Procedure 17

  3.1 Test Facility 17
  3.2 Experimental Setup 18
  3.3 Particle Image Velocimetry System and Measurement Procedure 19
  3.4 Measurement Uncertainty 21

4 Results and Discussion 23

  4.1 Mean Flow 23
    4.1.1 Contours of Mean Velocity 23
    4.1.2 Characterization of the recirculation bubbles 26
  4.2 Reynolds Stresses and Turbulent Kinetic Energy 28

4.2.1 Reynolds Normal Stresses 28
4.2.2 Reynolds Shear Stress and Turbulent Kinetic Energy 31
4.3 Probability Density Functions and Joint Probability Density Functions 33
4.3.1 Probability Density Functions 33
4.3.2 Joint-Probability Density Functions 33
4.4 Analysis on Streamwise evolution and comparison of Mean Velocities and Turbulence Statistics 35
4.5 Turbulence Production and Transport of TKE 40
4.5.1 Turbulence Production 40
4.5.2 Turbulence Transport 44
4.6 Frequency Spectra and Proper Orthogonal Decomposition (POD) 45
4.6.1 Frequency Spectra 45
4.6.2 Proper Orthogonal Decomposition 46
5 Conclusions and Recommendations 55

5.1 Summary and Conclusions 55
5.2 Recommendations for Future Work 56
References 58

A. Appendix 63

List of Tables

Table 2.1 Summary of previous studies of rectangular cylinders in various boundaries, WM (Wall-mounted), UF (Uniform flow), and FS (Free surface). B & A (Bergeles and Athanassiadis), K & G (Kindere and Ganapathisubramani), F & T (Fang and Tachie), K & T (Kumahor and Tachie). 7

List of Figures

Figure 1.1 (a) Flooding closes roads, bridge in Brewton, East Brewton (Source: The Brewton Standard), (b) Old Martuwarra Fitzroy River bridge destroyed by major flooding (Source: National Indigenous Times). 2

Figure 2.1 Mean flow topology of a long rectangular cylinder in a uniform flow. 8

Figure 2.2 Mean flow topology of a rectangular cylinder mounted on a wall 12

Figure 2.3 Schematic diagram of the salient flow features around sufficiently long rectangular 2D cylinder mounted on a free surface. The reattachment length on the cylinder measured from the leading edge is denoted as L_T, and onto the free surface measured from the trailing edge is denoted as L_W. 15

Figure 3.1 A picture of the recirculating water channel at the Turbulence and Hydraulic Engineering Laboratory (THEL). 18

Figure 3.2 Schematic view of the experimental setup and the fields of view (not to scale) 19

Figure 3.3 A picture of the particle image velocimetry (PIV) system at the THEL. 21

Figure 4.1 Contours of streamwise mean velocity (left) with $U = 0$ (red solid line) isopleth, and vertical mean velocity (right) with $V = 0$ isopleth (blue dashed line) and mean streamlines for (a, b) AR1, (c, d) AR2, (e, f) AR4, and (g, h) AR8. The (+) symbol denotes the location of the peak streamwise mean velocity with the magnitude. 24

Figure 4.2 Variation of reattachment length (a) on the cylinder measured from the leading edge and (b) on the free surface measured from the trailing edge with aspect ratio. Wall-mounted and uniform flow cases are denoted by WM and UF respectively. 27

Figure 4.3 Contours of streamwise Reynolds normal stress, $\overline{u'u'}$ (left) and vertical Reynolds normal stress, $\overline{v'v'}$ (right) and mean streamline for (a, b) AR1, (c, d) AR2, (e, f) AR4, and (g, h) AR8. 30

Figure 4.4 Contours of Reynolds shear stress, $\overline{u'v'}$ (left) and turbulent kinetic energy, $k = 0.5(\overline{u'u'} + \overline{v'v'})$ (right) and mean streamline for (a, b) AR1, (c, d) AR2, (e, f) AR4, and (g, h) AR8. 32

Figure 4.5 Probability density functions of u' at maximum $\overline{u'u'}$ (a) on top of the cylinder and (b) maximum $\overline{v'v'}$ in the wake for AR1, AR2, AR4, and AR8. 34

Figure 4.6 Joint probability density function of velocity fluctuations at maximum $\overline{u'v'}$ for (a) AR1, (b) AR2, (c) AR4, (d) AR8. 35

Figure 4.7 Streamwise variation of maximum Reynolds stresses for AR1, AR2, AR4, and AR8. x/L – Streamwise length along the cylinder length, x^*/h – Streamwise length from the trailing edge of the cylinder. 36

Figure 4.8 Streamwise variation of vertical location of the maximum Reynolds stresses for AR1, AR2, AR4, and AR8. x/L – Streamwise length along the cylinder length, x^*/h – Streamwise length from the trailing edge of the cylinder. 38

Figure 4.9 Profiles of streamwise mean velocity (U) (left), and TKE (right) at selected streamwise locations for AR1, and AR4, where $x/L_T = 1.0$ and $x^*/L_W = 1.0$ are the reattachment points on the cylinder and in the wake, respectively. FS (Free surface), WM (Wall-mounted) and UF (Uniform flow). 39

Figure 4.10 Contours of production of turbulent kinetic energy, P_k, and mean streamline for (a) AR1, (b) AR2, (c) AR4, and (d) AR8. 41

Figure 4.11 Profiles of the individual production terms at (a - c) maximum P_k, maximum (d - f) TKE on top of the cylinder and (g - i) in the wake for AR1 (left), AR2 (middle), and AR4 (right). 43

Figure 4.12 Contours of turbulence transport of TKE by velocity fluctuations u' (left) and v' (right) superimposed with the center of the mean shear layer (black dotted line) for (a, b) AR1, (c, d) AR2, (e, f) AR4, and (g, h) AR8. 45

Figure 4.13 Pre-multiplied energy spectra of u' at maximum $u'u'$ (a) on top of the cylinder and (b) in the wake for AR1, AR2, AR4, and AR8. 47

Figure 4.14 Relative contribution of streamwise and vertical velocity fluctuations to the total turbulent kinetic energy for the first four modes of (a) AR1, (b) AR2, (c) AR4, and (d) AR8. 49

Figure 4.15 Contours of the first four spatial POD modes of the vertical velocity fluctuations superimposed with mean velocity streamline for (a) AR1, and (b) AR2. The (+) symbols mark the centres of the vortices in each mode. 50

Figure 4.16 Contours of the first four spatial POD modes of the vertical velocity fluctuations superimposed with mean velocity streamline for (a) AR4, and (b) AR8. The (+) symbols mark the centres of the vortices in each mode. 51

Figure 4.17 Time signal of the mode coefficients (left), phase portraits (middle) and radius (right) of the first two modes of (a – c) AR1, (d – f) AR2, (g – i) AR4, and (j – l) AR8. 53

Figure 4.18 Pre-multiplied energy spectra of first two POD mode coefficients of (a) AR1 and AR2, and (b) AR4 and AR8. 54

Figure A.1 Vertical profiles of (a) streamwise mean velocity, (b) streamwise Reynolds normal stress, (c) vertical Reynolds normal stress, and (d) turbulent kinetic energy at the midpoint of the recirculation region (*x/h* = 6.42) for AR1 at different samples sizes... 63

Figure A.2 Contours of streamwise mean velocity (left) with $U = 0$ (red solid line) isopleth and vertical mean velocity (right) with $V = 0$ isopleth (blue dashed line) and mean streamlines for (a, b) AR2.5, (c, d) AR3 and (e, f) AR5. The (+) symbol denotes the location of the peak streamwise mean velocity with the magnitude. 64

Figure A.3 Contours of streamwise Reynolds normal stress, $\overline{u'u'}$ (left) and vertical Reynolds normal stress, $\overline{v'v'}$ (right) and mean streamline for (a, b) AR2.5, (c, d) AR3, and (e, f) AR5..... 65

Figure A.4 Contours of Reynolds shear stress, $\overline{u'v'}$ (left) and turbulent kinetic energy, $k = 0.5(\overline{u'u'} + \overline{v'v'})$ (right) and mean streamline for (a, b) AR2.5, (c, d) AR3, and (e, f) AR5. 66

Figure A.5 Probability density functions of u' at maximum $\overline{u'u'}$ (a) on top of the cylinder and (b) maximum $\overline{v'v'}$ in the wake for AR2.5, AR3, and AR5. 67

Figure A.6 Joint probability density function of velocity fluctuations at maximum $\overline{u'v'}$ for (a) AR2.5, (b) AR3, (c) AR5.. 68

Figure A.7 Streamwise variation of maximum Reynolds stresses for AR2.5, AR3, and AR5. *x/L* – Streamwise length along the cylinder length, *x*/h* – Streamwise length from the trailing edge of the cylinder.. 69

Figure A.8 Streamwise variation of vertical location of the maximum Reynolds stresses for AR2.5, AR3, and AR5. *x/L* – Streamwise length along the cylinder length, *x*/h* – Streamwise length from the trailing edge of the cylinder. 70

Figure A.9 Profiles of streamwise mean velocity (*U)* (left), and TKE (right) at selected streamwise locations for AR8, where $x/L_T = 1.0 \;\; and \; x^*/L_W = 1.0$ are the reattachment points on the cylinder and in the wake, respectively. FS (Free surface), and WM (Wall-mounted). 71

Figure A.10 Contours of production of turbulent kinetic energy, P_k, and mean streamline for (a) AR2.5, (b) AR3 and (c) AR5. 72

Figure A.11 Profiles of the individual production terms at (a, d, g, j) maximum P_k, maximum TKE (b, e, h, k) on top of the cylinder and (c, f, i, l) in the wake for AR2.5 (a - c), AR3 (d - f), AR5 (g – i), and AR8 (j - l).. 73

Figure A.12 Contours of turbulence transport of TKE by velocity fluctuations u' (left) and v' (right) for (a, b) AR2.5, (c, d) AR3, and (e, f) AR5.. 74

Figure A.13 Pre-multiplied energy spectra of u' at maximum $\overline{u'u'}$ (a) on top of the cylinder and (b) in the wake for AR2.5, AR3, and AR5. 75

Figure A.14 Pre-multiplied energy spectra of u' along the mean streamline (a, b) AR1, (c, d) AR2, and (e, f) AR2.5. 76

Figure A.15 Pre-multiplied energy spectra of u' along the mean streamline for (a, b) AR3, (c, d) AR4, and (e, f) AR5.. 77

Figure A.16 Pre-multiplied energy spectra of u' (a, b) along the mean streamline for AR8, and (c, d) at maximum $\overline{v'v'}$ on the cylinder, and in the wake, respectively, for all aspect ratios............ 78

Figure A.17 Relative contribution of streamwise and vertical velocity fluctuations to the total turbulent kinetic energy for the first four modes of (a) AR2.5, (b) AR3, and (c) AR5............... 79

Figure A.18 Contours of the first four spatial POD modes of the vertical velocity fluctuations superimposed with mean velocity streamline for (a) AR2.5, and (b) AR3. The (+) symbols mark the centres of the vortices in each mode. 80

Figure A.19 Contours of the first four spatial POD modes of the vertical velocity fluctuations superimposed with mean velocity streamline for AR5. The (+) symbols mark the centres of the vortices in each mode... 81

Figure A.20 Time signal of the mode coefficients (left), phase portraits (middle) and radius (right) of the first two modes of (a – c) AR2.5, (d – f) AR3, and (g – i) AR5....................................... 82

Figure A.21 Pre-multiplied energy spectra of first two POD mode coefficients of (a) AR2.5, (b) AR3, and (c) AR5. 83

Nomenclature

Acronyms

AR	Streamwise aspect ratio
BR	Blockage ratio
FOV	Field of view
Fr	Froude number
JPDF	Joint-probability density function
PDF	Probability density function
PIV	Particle image velocimetry
POD	Proper Orthogonal Decomposition
Q1	JPDF quadrant 1 $(+u', +v')$
Q2	JPDF quadrant 2 $(-u', +v')$
Q3	JPDF quadrant 3 $(-u', -v')$
Q4	JPDF quadrant 4 $(+u', -v')$
Re	Reynolds number based on the cylinder height and freestream velocity
St	Strouhal number
TBL	Turbulent boundary layer
TKE	Turbulent kinetic energy, k
Tu	Turbulence intensity

Symbols

F_u	Flatness factor for streamwise velocity fluctuations
F_v	Flatness factor for transverse velocity fluctuations

g	Acceleration due to gravity
h	Submerged vertical height of cylinder
H	Total vertical height of cylinder
L	Streamwise length of cylinder
L_T	Mean reattachment length on cylinder
L_W	Mean reattachment length onto the free surface from trailing edge
P_k	Turbulence production
S_k	Stokes number
U	Streamwise mean velocity
U_c	Convective velocity
U_e	Freestream velocity
U_{max}	Maximum streamwise velocity
U_{min}	Maximum backflow
U_s	Slip velocity of seeding particle
x	Streamwise coordinate
x^*	Streamwise coordinate originating from the trailing edge
y	Vertical coordinate

Greek Letters

ν	Kinematic viscosity of water
μ_f	Dynamic viscosity of water
ρ_f	Density of water
ρ_p	Density of seeding particles

τ_{flow}	Smallest characteristic timescale
τ_p	Relaxation time
τ_o	Largest characteristic timescale
δ	Turbulent boundary layer thickness
λ	Wavelength

Subscripts and Superscripts

$(.)'$	Fluctuating velocity component
$\overline{(.)}$	Time-averaged component
$(.)_{rms}$	Root-mean-square value

1. Introduction

This chapter presents the background and motivation of the present study along with the outline of the subsequent chapters of this thesis.

1.1 Background and Motivation

Turbulent flow separation around bluff bodies has many engineering and environmental applications including flow around bridge decks, buildings, vehicles, wind turbines, and offshore structures. The flow fields in these applications are characterized by the shedding of vortices and unsteady wakes which can lead to adverse effects such as flow-induced structure vibration and acoustic noise. These phenomena can degrade the performance of many engineering systems and result in fatigue failure (Cermak, 1976), impacting the environment. Several studies have explored turbulent flow separation over bluff bodies in unbounded flows and in configurations where free surface effects are absent. Consequently, dynamics of flow separation at the free surface remain relatively unexplored. Such insight is critical for applications such as heaving-buoys, breakwaters, and the installation of solar panels on the surfaces of rivers or lakes as shown in Figure 1.1. In other engineering applications, the effects of flow separations are utilized to improve systems, such as convective heat transfer. To devise effective flow control strategies and promote efficient mixing and convective heat transfer, it is crucial to understand the dynamics of separated and reattached turbulent flows over bluff bodies (Zhang et al., 2013; Liu et al., 2018). Numerous studies have been conducted to examine the turbulent flow dynamics around bluff bodies of various geometries, including circular cylinders (Bearman, 1969; Lin et al., 1995; Addai et al., 2024), rectangular cylinders (Okajima, 1982; Nakagawa et al., 1999; Kuroda et al., 2007), and

Figure 1.1 (a) A schematic of a floating heaving-buoy integrated floating breakwater (Zhang et al., 2019), (b) Solar panels installed on water surface (Source: Times of Malta).

trapezoidal cylinders (Miau et al., 2003; Kang and Tachie, 2023). These investigations show that flow separation and its dynamics of the flow are highly sensitive to the geometry of the bluff body, the Reynolds number (Re = $U_e h/\upsilon$, where U_e is the freestream velocity, h is the cylinder height, and υ is the kinematic viscosity of the fluid), blockage ratio (BR = h/D, where h and D are the cylinder height and the depth of fluid, respectively), and turbulence intensity. Rectangular cylinders, with their simple geometry, have been used to study the fundamental characteristics of flow separation around bluff bodies. Flow past sharp-edged rectangular cylinders is significantly influenced by streamwise aspect ratio (AR = L/h, where L and h are the streamwise length and height of the cylinder, respectively). Most previous studies were performed with rectangular cylinders in a uniform flow (Okajima, 1982; Knisely, 1990; Nakagawa et al., 1999; Shi et al., 2010; Trias et al., 2015; Cimarelli et al., 2018; Kumahor & Tachie, 2022, 2023a; Liu et al., 2024) or wall-mounted conditions (Bergeles and Athanassiadis, 1983; Sherry et al., 2010; Essel et al., 2015; Nematollahi and Tachie, 2018; van der Kindere and Ganapathisubramani, 2018; Fang and Tachie, 2019b; Chalmers et al., 2021).

On the other hand, studies on free surface-mounted rectangular cylinders are limited, and the flow characteristics are not well understood. Unlike the wall-mounted cases, the approach flow upstream of the free surface-mounted cylinder has negligible mean shear and relatively low turbulence intensity. This is due to the free-slip condition which prevents the formation of a boundary layer upstream the cylinder. However, the free-slip condition promotes non-zero velocity component(s) parallel to the free surface and the velocity component perpendicular to the free surface is suppressed. As a result, the reattachment mechanism on the free surface and the wake dynamics behind the free surface-mounted cylinders may be different from those of wall-mounted and uniform flow cases.

Previous studies on wall-mounted and uniform flows (Bergeles & Athanassiadis, 1983; van der Kindere & Ganapathisubramani, 2018; Chalmers et al., 2021; Kumahor & Tachie, 2022, 2023a; Liu et al., 2024), have classified the reattachment of the separated shear layer into three regimes (unattached, intermittently reattached with no mean reattachment, and mean reattachment), based on the streamwise aspect ratio. In the cases of low aspect ratios, the separated shear layer is shed directly into the wake behind the cylinder. Meanwhile, for high aspect ratios, the separated shear layer reattaches onto the cylinder, followed by redevelopment of a boundary layer on the cylinder before subsequent separation at the trailing edge. For intermediate aspect ratios, the separated shear layer undergoes intermittent reattachment on the cylinder and direct shedding into the wake. While the critical aspect ratios for demarcating the three regimes have been extensively studied for wall-mounted (Bergeles and Athanassiadis, 1983; van der Kindere and Ganapathisubramani, 2018; Chalmers et al., 2021) and uniform flow (Kumahor & Tachie, 2022, 2023a; Liu et al., 2024) cases, our understanding remains limited for free surface-mounted cylinders. This study aims to enhance the understanding of the effects of aspect ratio on the flow characteristics on free surface-mounted rectangular cylinders using a planar time-resolved particle image velocimetry (TRPIV) system. The TRPIV provides whole-field velocity measurements at high sampling frequency, which makes it well-suited for evaluating the spatiotemporal characteristics of the separated flows.

1.2 Thesis Outline

The rest of the thesis is structured as follows: Chapter 2 presents a review of the relevant literature and Chapter 3 describes the experimental set-up and detailed measurement procedures. Chapter 4 covers the results and discussions, and Chapter 5 provides a summary of the major findings and conclusions along with recommendations for future research.

2. Literature Review

This chapter provides a review of previous studies on rectangular cylinders in various flow conditions, including cylinders in uniform flow, wall-mounted cylinders, free surface-mounted cylinders, which are pertinent to the current study.

2.1 Literature Review

Extensive investigations on flow around sharp-edged rectangular cylinders demonstrate that flow separation occurs at the sharp-leading edges of the cylinders. Flow around rectangular cylinders under various boundary conditions is significantly influenced by the flow conditions and aspect ratio, resulting in either similar or different flow characteristics. Table 2.1 presents a summary of pertinent previous investigations on rectangular cylinders mounted in a uniform flow, on a wall, and on the free surface. Here, the approach flow turbulence intensity is defined as $Tu = u'_{rms}/U_e$ (where $u'_{rms} = \sqrt{\overline{u'u'}}$ and u' is the fluctuating streamwise velocity).

2.1.1 Uniform flow

For rectangular cylinders in a uniform flow, the approach flow separates at both the top and bottom sharp leading edges for Re > 150 (Franke et al., 1990; Mashhadi et al., 2021). The separated shear layers feature small-scale Kelvin Helmholtz (KH) instabilities which pair up to form large-scale von-Kármán (VK) vortices. These vortices are alternatively shed from each side of the cylinder. The frequency at which the vortices are shed is commonly represented in dimensionless terms as the Strouhal number, $St = fh/U_e$, where f is the vortex shedding frequency, h is the cylinder height, and U_e is the freestream velocity. The presence of two separated shear layers results in a mean flow topology symmetric about the horizontal centreline of the cylinder as shown in

Table 2.1 Summary of previous studies of rectangular cylinders in various boundaries, WM (Wall-mounted), UF (Uniform flow), and FS (Free surface). B & A (Bergeles and Athanassiadis), K & G (Kindere and Ganapathisubramani), F & T (Fang and Tachie), K & T (Kumahor and Tachie).

Study	Boundary	Re	*Tu* (%)	BR (%)	AR
B & A (1983)	WM	26000	0.50	8.9	1, 2, 3, 4, 5, 6, 10
K & G (2018)	WM	20000	4.00	5.0	0.1, 1, 2, 4, 6, 8
Chalmers et al. (2021)	WM	13200	15.10	7.0	1, 2, 3, 4, 5, 6, 8
F & T (2019)	WM	12300	/	7.0	2.36
Nakagawa et al. (1999)	UF	3000	6.00	20.0	0.5, 1, 2, 3
Okajima (1982)	UF	500	0.50	2.5	2
Shi et al. (2010)	UF	1000	2.00	22.2	3, 6, 9
Liu et al. (2024)	UF	3000-21000	1.00	7.0	1, 2, 3, 4
K & T (2022)	UF	16200	1.20	7.0	1, 5
Moore et al. (2019a)	UF	13400-118000	/	6.4	1, 3, 5
Moore et al. (2019b)	UF	13000-120000	/	7.2	1, 3, 5
Abdul-Salam et al. (2023)	UF	3000, 7500, 15000	/	2.5 - 15	3
Fang et al. (2022)	FS	14400	1.30	7.0	33.3
Fang et al. (2023)	FS	55900 - 204000	1.30	2.4 – 17.7	33.3
Arslan et al. (2013)	FS	12100	14.00	/	3
Present	FS	11100	0.87	7.0	1, 2, 2.5, 3, 4, 5, 8

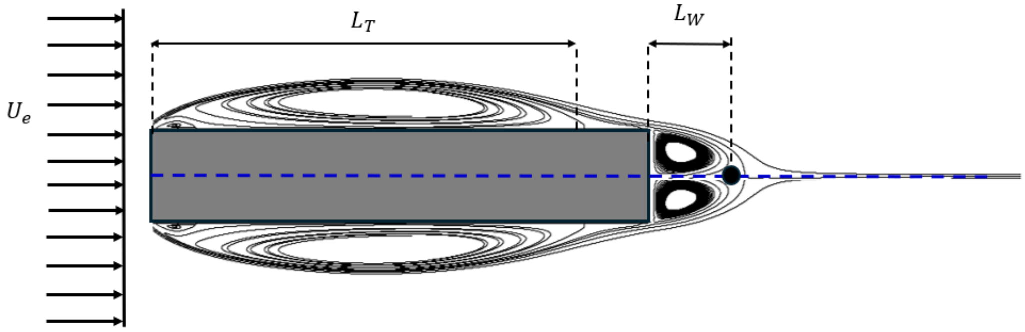

Figure 2.1 Mean flow topology of a long rectangular cylinder in a uniform flow.

Figure 2.1. The reattachment length on the cylinder, measured from the leading edge to the attachment point on the cylinder, is denoted as L_T. The reattachment length in the wake, L_W, characterized by the size of the wake vortex, is measured from the trailing edge to the point of reattachment onto the horizontal centerline. Previous studies on rectangular cylinders in a uniform flow reveal the formation of three distinct recirculation bubbles regardless of the flow regime: a primary vortex over the cylinder, a secondary vortex near the leading edge, and a wake vortex behind the cylinder. Although rectangular cylinders have a simple geometric shape, the flow topology and vortex dynamics around the cylinders can become significantly complex depending on the aspect ratio.

Previous studies on rectangular cylinders in a uniform flow reported no mean reattachment on cylinders of AR < 4, with cylinders of AR < 2 exhibiting direct shedding into the wake region (Kumahor and Tachie, 2022, 2023a, 2023b; Liu et al., 2024). Rectangular cylinders with an aspect ratio between 2 and 3.5 are known to exhibit a range of complex flow patterns, including both unattached to reattached flows (Okajima, 1982; Knisely, 1990; Norberg, 1993; Nakagawa et al., 1999). Liu et al. (2024) investigated the effects of aspect ratio (AR = 1 to 4, hereafter denoted as AR1-AR4), and Reynolds number (Re $= 3000$ to 21000) and observed no mean reattachment for AR1 and AR2, but reported mean reattachment for AR4, irrespective of the Reynolds number. The separated shear layer of AR1 is shed directly into the wake forming a small wake vortex. The AR2 cylinder falls in the intermediate regime where the separated shear layer intermittently reattaches onto the cylinder, and this results in a larger wake vortex compared to AR1 and AR > 2. The effects of Reynolds number revealed that for AR3, reattachment varies with the Reynolds number, with the separated shear layer reattaching right at the trailing edge for Re $= 7200$ with no reattachment at Re = 3000. It was noted that the recirculation lengths decrease with increasing Reynolds number, but asymptotes at Re ≥ 14700 for AR1, AR3 and AR4 cylinders. Moore et al. (2019a, 2019b) investigated the effects of Reynolds number around AR1, AR3, and AR5 cylinders and observed an upstream shift of the transition point from laminar to turbulence with increasing Reynolds number. In addition, direct shedding of the separated shear layer occurred for AR1, while mean reattachment occurred for AR5 irrespective of Reynolds number. However, different flow regimes (attached and unattached) were reported for the AR3 cylinder at Reynolds numbers between Re = 13000 and 120000, at two different blockage ratios (BR = 6.4% and 7.2%). Here, the Reynolds numbers are larger than the threshold Reynolds number for reattachment for AR3 (Re = 7200) by Liu et al. (2024) at BR = 7.0%. At a Reynolds number of 3000, Nakagawa et al. (1999) reported mean reattachment onto the AR3 cylinder at BR = 20.0% which is much larger than the BR = 7.0% by Liu et al. (2024), showing that the flow dynamics of the AR3 cylinder are also strongly influenced by blockage ratio.

Recently, Abdul-Salam et al. (2023) studied the effects of blockage ratio on flow around AR3 for Re $= 3000$ to 15000 and BR $= 2.5\%$ to 15.0%. It was reported that mean reattachment occurred for Re = 3000 and BR ≥ 10.0%, Re = 7500 and BR ≥ 5.0%, and Re = 15000 and BR = 15.0%. The study demonstrates that the flow topology for the unattached AR3 cases resembles that of the AR2 which is indicative of the intermediate regime (Okajima, 1982; Liu et al., 2024). While frequency spectra analysis on the reattached cylinders revealed distinct vortex shedding frequencies characterized by the large-scale VK vortices, multiple co-dominating frequencies were observed for the unattached cases. The results indicate that the dynamics of the flow over the cylinder is significantly influenced by both Reynolds number and blockage ratio.

Shi et al. (2010) investigated the effects of aspect ratio (AR3, AR6 and AR9) at $\mathrm{Re} = 1000$. The results showed that for AR3, the separated shear layer is shed directly into the wake creating a highly unstable wake due to the energetic leading-edge vortices. For AR6 and AR9, mean reattachment was observed. The study also revealed that the separated shear layer periodically reattaches onto the AR6 cylinder but always reattaches onto the AR9 cylinder. Proper orthogonal decomposition (POD) analyses showed that for AR3, the dominance of the growing leading-edge vortices in the separated shear layer significantly contributed to the fluctuating energy from the first POD mode (55.7%). In contrast, the contribution of the first POD mode to the total fluctuating energy is low for AR6 (17.8%) and AR9 (13.9%), due to the spatially constrained growth of the leading-edge vortices in the reattached shear layer.

Kumahor and Tachie (2022) studied turbulent flow around rectangular cylinders with different streamwise aspect ratios of AR1 and AR5 and more recently on AR1, AR2, and AR4 (Kumahor and Tachie, 2023a) at Re = 16200 as well as AR0.5 (Kumahor and Tachie, 2023b) at Re = 5100 to 21000. The results showed that for AR < 2, the separated shear layer is shed directly into the wake. The AR2 cylinder exhibited intermittent reattachment of the separated shear layer while mean reattachment was observed for AR4 and AR5. The fundamental shedding frequencies of the large-scale VK vortices were as follows: AR0.5 ($St = 0.150$), AR1 ($St = 0.138$), AR4 ($St = 0.134$), and AR5 ($St = 0.112$). Interestingly, AR2 exhibited two co-dominant shedding frequencies ($St =$

0.084 and *St* = 0.154) attributed to the intermittent reattachment of the separated shear layer onto the cylinder. POD analyses on AR0.5, AR1, AR2, and AR4 revealed that apart from AR2, the fundamental vortex shedding frequency was the dominant frequency, and the first POD mode pairs contain similar energy percentages, indicating regular shedding patterns of the VK vortices over the cylinders.

2.1.2 Wall-mounted cylinder

As shown in Figure 2.2, a boundary layer forms upstream of wall-mounted cylinders due to the no-slip boundary condition, resulting in significant mean shear close to the wall and higher levels of turbulence of the oncoming flow. The flow separates from the wall and reattaches onto the front face of the cylinder due to adverse pressure gradient. The reattached flow then separates from the sharp leading edge of the cylinder forming a separated shear layer over the cylinder.

Research on wall-mounted cylinders have used a forward-facing step (FFS) (Sherry et al., 2010; Essel et al., 2015; Essel and Tachie, 2017; Nematollahi and Tachie, 2018; Chalmers et al., 2021) and a backward facing step (BFS) (Wu et al., 2013; Essel and Tachie, 2015) as canonical geometries to investigate the interactions between boundary layers and bluff bodies. Flow over FFS is used to study separated and reattached turbulent flows characterized by two distinct separation bubbles: one upstream of the cylinder and the other downstream of the leading edge. The oncoming flow separates from the wall and reattaches onto the front face of the cylinder, with subsequent separation from the leading edge. In contrast, flow over BFS involves a separated shear layer from the trailing edge of the cylinder and reattaches onto the bottom wall interacting with both the freestream and a reverse flow region, resulting in a complex feedback mechanism. This interaction is a source of pressure loss and noise (Chun and Sung, 1996; Le et al., 1997). A more complex example of a wall-mounted cylinder exhibiting significantly more complex flow characteristics is the forward-backward-facing step (FBFS), which has a finite streamwise length

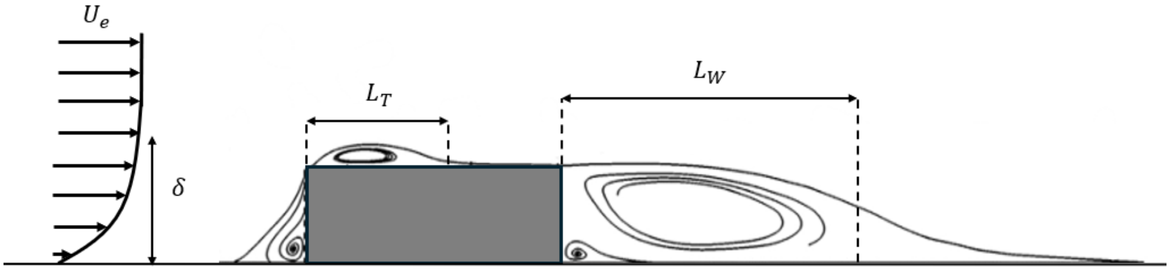

Figure 2.2 Mean flow topology of a rectangular cylinder mounted on a wall.

(Chalmers et al., 2021). The FBFS combines features of FFS and BFS, and may consist of either unattached or reattached flows depending on the aspect ratio. From the previous studies on wall-mounted rectangular cylinders, two separation bubbles are observed (one upstream, and the other downstream) for cylinders in the unattached regime (typically AR < 2). In the reattached cases (including FFS), an additional separation bubble forms on top of the cylinder of streamwise length L_T (measured from the leading edge to the point of reattachment on the cylinder), highlighting the complex dynamics of flow separation and reattachment around these structures. The mean flow reattachment on wall-mounted cylinders is primarily influenced by the characteristics of the oncoming boundary layer including turbulence intensity and blockage ratio.

Studies by Bergeles and Athanassiadis (1983) on AR1 to AR10 reported mean flow reattachment for AR ≥ 5 with an approach boundary layer thickness (δ/h) of 0.48 at constant length ($L_T/h \approx 3.7$·). van der Kindere and Ganapathisubramani (2018) investigated flow separation over cylinders of aspect ratio between AR0.1 and AR8 immersed in a thick, turbulent boundary layer (TBL) of $\delta/h = 1.37$, and observed mean reattachment for AR ≥ 4 constant at $L_T/h \approx 2.6$. With an approach flow of δ/h = 4.8, Fang and Tachie (2019b) reported mean reattachment at $L_T/h = 1.6$ onto a relatively shorter cylinder of AR = 2.36. Chalmers et al. (2021) studied the effects of aspect ratio of range AR1 and AR8 for a thick TBL of δ/h = 6.5, and observed reattachment at $L_T/h \approx 1.6$ for AR ≥ 2. Moreover, the authors noted that instantaneous flow reattachment occurs consistently for AR ≥ 4. The smaller critical aspect ratio for thicker boundary layers ($\delta/h \geq 4.8$) is ascribed to the higher incoming turbulence intensity, which promotes entrainment and results in shorter mean reattachment lengths on the cylinders (Nematollahi and Tachie, 2018). The reattached shear layer subsequently separates from the trailing edge and reattaches onto the wall at a length L_W from the trailing edge, forming a wake recirculation bubble. The size of the wake recirculation bubble decreases with increasing aspect ratio but asymptotes for the reattached cylinders (Bergeles and Athanassiadis, 1983; van der Kindere and Ganapathisubramani, 2018; Chalmers et al., 2021).

Comparative analysis on the length of the recirculation bubbles on AR4 cylinder by van der Kindere and Ganapathisubramani (2018) with other studies (Arie et al., 1975; Bergeles and Athanassiadis, 1983) of different boundary layer thicknesses revealed that the sizes of the separation bubbles are strongly influenced by the oncoming TBL. It was noted that a thick TBL leads to a shorter recirculation length on top of the cylinder but a longer wake recirculation length. On the other hand, a relatively thin TBL results in a longer recirculation length and shorter wake recirculation length.

Previous studies have investigated the effects of Reynolds number on wall-mounted cylinders and have consistently reported that the reattachment length on the cylinder increases with increasing Reynolds number, and asymptotes at a sufficiently higher Reynolds number. For instance, Essel et al. (2015) observed that the reattachment length increases until the Reynolds number reaches approximately 6380. Similarly, Sherry et al. (2010) found that the reattachment length increases up to Re ≈ 8500. Beyond these threshold Reynolds numbers, the reattachment length asymptotes.

The discrepancies in these threshold Reynolds numbers between the two studies can be attributed to variations in flow conditions, including differences in turbulence intensity and blockage ratio. Fang and Tachie (2019b) conducted frequency spectra analysis on an FFS and discovered that the upstream bubble exhibits a low-frequency flapping motion at $St = 0.075$, characterized by a quasi-periodic enlargement and shrinkage of the bubble. The dominant frequency of the separation bubble over the cylinder was lower, at approximately $St = 0.03$, with a subdominant shedding frequency similar to that of the upstream bubble. This indicates that the shedding frequency over the wall-mounted cylinder is strongly influenced by the upstream flow conditions. Chalmers et al. (2021) also found that the shedding frequency over the cylinders reflected the characteristic shedding frequency of the approach flow. However, a lower dominant shedding frequency was observed for the bubble over the AR2 cylinder compared to the other cylinders, which was attributed to the effects of the recirculation bubble in the wake.

2.1.3 Free surface-mounted cylinder

Research on semi-submerged cylinders explores the hydrodynamic interactions between partially submerged structures and surrounding fluid dynamics. A schematic of a rectangular cylinder of submerged thickness, h, is shown Figure 2.3. Arslan et al. (2013) conducted experimental and numerical studies on a semi-submerged AR3 cylinder at various submergence ratios ($h/H = 0.2$, 0.4, 0.6, and 0.8, where h is the submerged thickness, and H is the total height of the cylinder) at a Reynolds number of 12100. The findings indicate that the separated shear layer reattaches on the cylinder, forming a recirculation bubble on top of length L_T, and subsequently separates from the trailing edge forming a recirculation bubble of length L_W, in the wake. It was observed that increasing h increases the size of the recirculation bubbles. Fang et al. (2022) investigated the

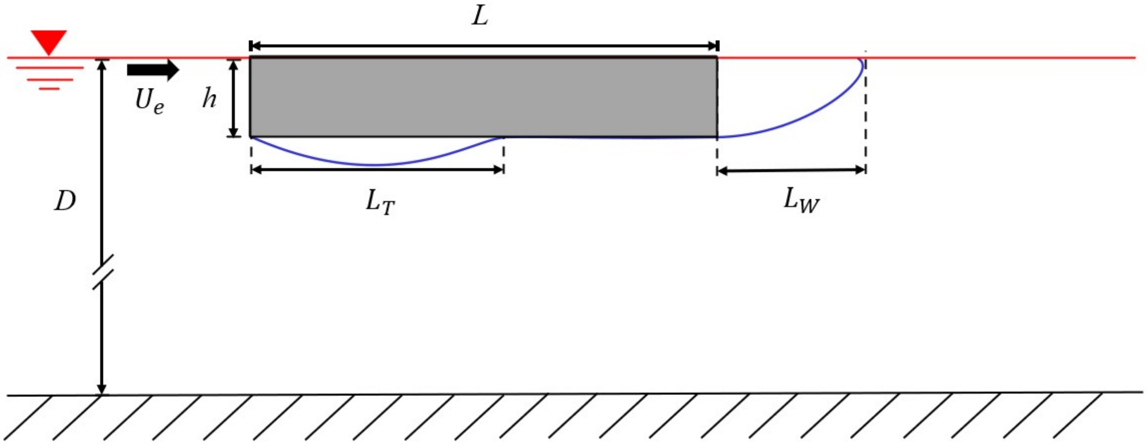

Figure 2.3 Schematic diagram of the salient flow features around sufficiently long rectangular 2D cylinder mounted on a free surface. The reattachment length on the cylinder measured from the leading edge is denoted as L_T, and onto the free surface measured from the trailing edge is denoted as L_W.

impact of undersurface roughness on flow separation and reattachment over a semi-submerged rectangular cylinder. The streamwise aspect ratio (AR33.3) was sufficiently large to ensure flow reattachment onto the cylinder and nullify the influence of the wake region on the flow separation near the leading edge. The results showed that the mean reattachment length in the smooth cylinder case agreed with the values reported for cylinders in a uniform flow (Kiya and Sasaki, 1983; Moore et al., 2019a) when properly scaled at similar Reynolds numbers. Fang et al. (2023) varied the ratio of the submerged thickness of the cylinder (h) to the water depth (D) between 0.02 and 0.18 and examined Reynolds numbers ranging from 55900 to 204000. Significant blockage effects were observed, showing a monotonic increase in reattachment length on the cylinder surface with increase in submerged thickness (h).

2.2 Objective

The effects of aspect ratio on rectangular cylinders have been extensively studied, primarily focusing on wall-mounted cylinders, and cylinders in a uniform flow, where the effects of the free surface on the flow dynamics is often overlooked. Investigations on semi-submerged rectangular cylinders have been limited to specific cylinder lengths with mean reattachment (Arslan et al., 2013; Fang et al., 2022, 2023). Consequently, the effects of varying streamwise extents on flow separation at the free surface remain inadequately explored. The literature clearly shows that the unsteady characteristics and flow regimes of free surface-mounted rectangular cylinders are not well understood.

Therefore, the present study aims to investigate the effects of streamwise aspect ratio on the flow characteristics of free surface-mounted rectangular cylinders. The results are also compared with the findings on studies on wall-mounted rectangular cylinders and cylinders in a uniform flow to identify similarities and differences across the various boundaries.

To achieve this objective, experiments were conducted at a fixed Reynolds number (Re $= 11100$) blockage ratio (BR = 7.0%), and Froude number ($Fr = U_e/\sqrt{gD}$ = 0.18, where g is the acceleration due to gravity) for seven (7) aspect ratios (AR1 – AR8) to examine the three main flow regimes. By maintaining a fixed Reynolds number and blockage ratio, the study isolates the impact of aspect ratio on flow behavior. This approach facilitates comparative analysis with previous studies in the uniform flow, and with wall-mounted conditions in the literature. The velocity measurements were performed using a time-resolved particle image velocimetry (TRPIV) system. The flow characteristics are examined using the mean flow, Reynolds stresses, probability density functions, joint probability density functions, turbulent kinetic energy, turbulence production, frequency spectra, and proper orthogonal decomposition.

3. Experimental Setup and Measurement Procedure

This chapter discusses the experimental setup and measurement procedure utilized for the velocity measurements. The chapter encompasses a detailed description of the test facility, an overview of the test cases, as well as the time-resolved particle image velocimetry (TRPIV) system used to measure the velocity fields, and the uncertainties associated with the velocity measurements are also presented.

3.1 Test Facility

The experiments were conducted in an open recirculating water channel in the Turbulence and Hydraulic Engineering Laboratory (THEL) at the University of Manitoba. The water channel consists of a flow conditioning unit, a variable frequency drive assembly, a test section, and a return pipe as shown in Figure 3.1. A perforated plate, hexagonal honeycomb, mesh screens of various sizes, and a 4.88:1 converging section make up the flow conditioning unit. The flow conditioning unit is utilized to minimize turbulence in the flow before entering the test section. The test section of the water channel is 6.00 m long, 0.60 m wide, and 0.45 m deep. The side and bottom walls of the test section are fabricated with smooth transparent Abrasion Resistant® acrylic plates to aid optical access from the walls of the test section. The flow leaving the test section enters a return plenum, which is fitted with a turning vane system which divides and redirects the flow. The flow then proceeds back to the conditioning unit through the return pipe. The flow is driven by a 30 kW variable speed motor pump which is able to continually vary the water velocity from 0.03 m/s to 2.00 m/s.

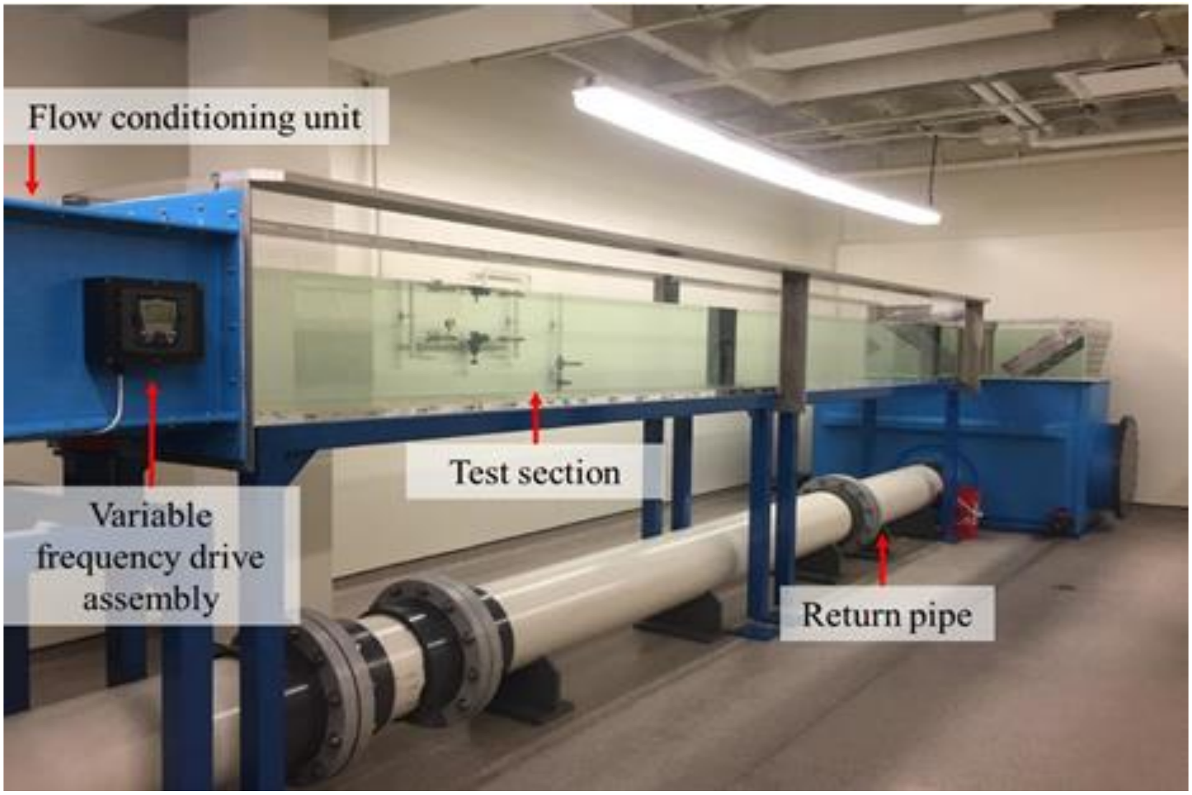

Figure 3.1 A picture of the recirculating water channel at the Turbulence and Hydraulic Engineering Laboratory (THEL).

3.2 Experimental Setup

Seven rectangular cylinders were fabricated from smooth acrylic plates with a height, $h = 0.030$ m, spanwise width, $B = 0.588$ m, and streamwise lengths, of $L = 0.030$ m, 0.060 m, 0.075 m, 0.090 m, 0.120 m, 0.150 m, and 0.240 m, resulting in aspect ratios AR = 1, 2, 2.5, 3, 4, 5, and 8, respectively. The rectangular cylinders were mounted in the test section screwed to two 6 mm thick side plates on either end. The side plates were placed at 0.7 m from the entrance of the test section. The upstream water depth was maintained at $D = 0.430$ m at a temperature of 20°C, and the cylinders were mounted at 0.400 m from the bottom wall of the test section. The cylinders were fully submerged such that there was no spill over the top surface of the cylinder. The blockage

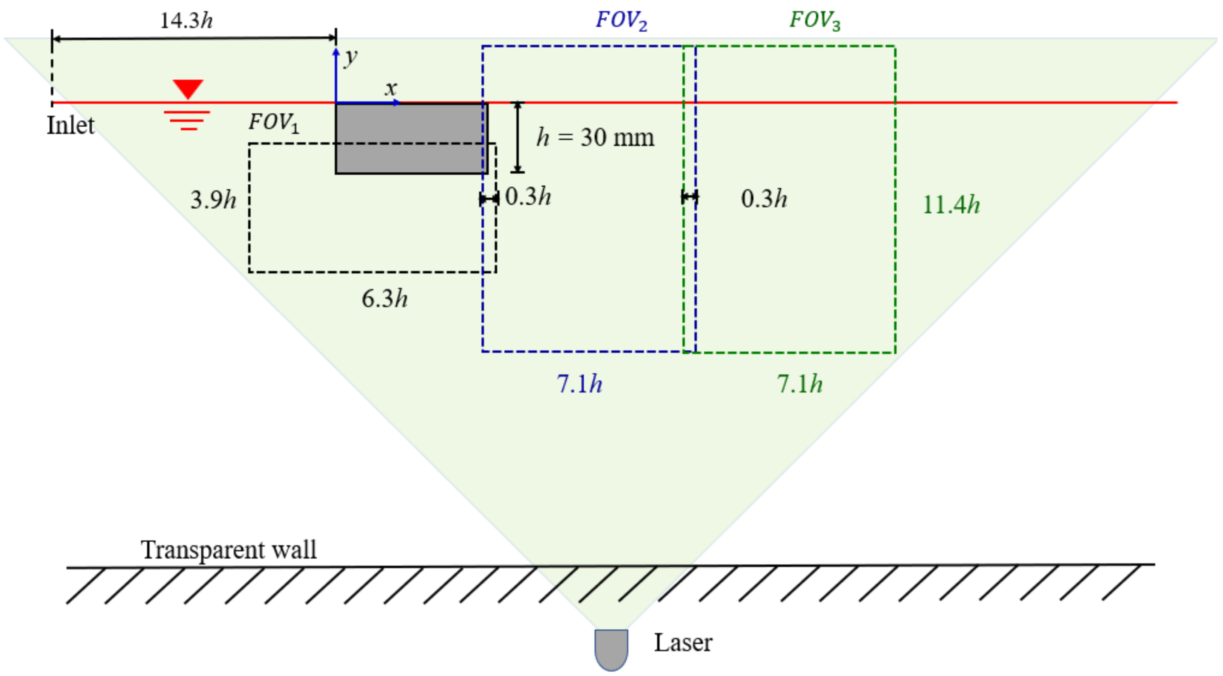

Figure 3.2 Schematic view of the experimental setup and the fields of view (not to scale).

ratio (BR) was 7%, and the spanwise aspect ratio $B/h = 19.6$, was large enough such that side-wall effects on the channel midspan are negligible (Fang and Tachie, 2019a). Figure 3.2 shows a schematic of the sideview of the cylinder mounted at the free surface with dimensions of the cylinder and fields of view (FOV) used in the experiment. The freestream velocity, $U_e = 0.37$ m/s and Reynolds number (Re) was 11100. The Froude number ($\frac{U_e}{\sqrt{gD}}$) was 0.18, implying negligible free surface distortion. The turbulence intensity (Tu) measured at the free surface in the absence of the cylinder was 0.87%. Using a Cartesian coordinate system (x, y), the origin was set at the top leading edge of the cylinder.

3.3 Particle Image Velocimetry System and Measurement Procedure

Time-resolved PIV system was used to measure the flow field at the midspan of the channel. As shown in Figure 3.3, the TRPIV system consists of a dual-cavity high-speed Neodymium-doped yttrium lithium fluoride (Nd: YLF) laser, three complementary metal oxide semiconductor (CMOS) cameras, and a data processing system. The flow was seeded with silver coated glass spheres, 10 μm (d_p) in size with a specific gravity of 1.4. The slip velocity (U_s) and particle relaxation time (τ_p) were calculated using the equations:

$$U_s = \left[{d_p}^2(\rho_p - \rho_f)g\right]/\left[18\mu_f\right] \tag{3.1}$$

$$\tau_p = U_s/g \tag{3.2}$$

The stokes number ($S_k = \tau_p/\tau_{flow}$) was used to characterize the response of the particles to the flow using the smallest characteristic timescale ($\tau_{flow} = \tau_o/\sqrt{\mathrm{Re}}$) where $\tau_o = h/U_e$). This resulted in S_k = 0.0029 which is orders of magnitude lower than the threshold of S_k = 0.05 (Samimy and Lele, 1991), demonstrating that the particles follow the flow faithfully. The particles were illuminated by a high-speed dual-cavity neodymium yttrium-lithium fluoride laser with wavelength 527 nm of 30 mJ/pulse maximum energy. The cylinders were coated with non-reflective black paint to reduce laser reflection. Three high-speed complementary metal oxide semi-conductor cameras with 2560 pixel×1600 pixel were used to capture three fields of view (FOV_1, FOV_2, and FOV_3). The cameras were fitted with EX SIGMA 105 mm lens and two Nikkon 60 mm lens for FOV_1, FOV_2, and FOV_3, respectively. Adjacent fields of view overlapped by 10 mm. The sampling frequency was set at 600 Hz and 60000 samples were taken.

The data collection and post-processing of velocity vectors were performed using a commercial software (DaVis version 10.0.5). To calculate the average particle displacement inside an interrogation area, the PIV images were post-processed using an adaptive multi-grid cross-correlation approach using a multi-pass fast Fourier transform with a 1-D Gaussian peak-fitting function. The first interrogation area was 128 pixel×128 pixel with 50% overlap and final size was

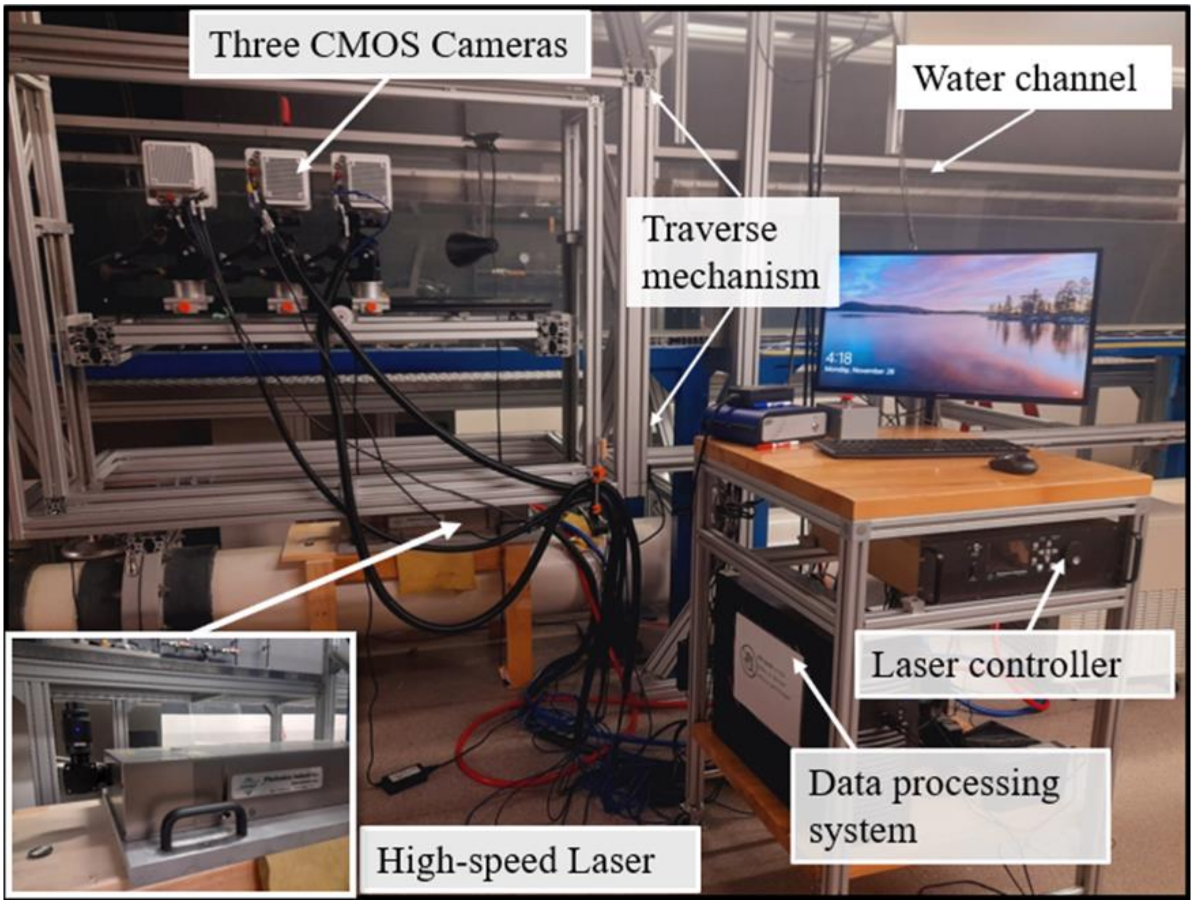

Figure 3.3 A picture of the particle image velocimetry (PIV) system at the THEL.

24 pixel×24 pixel with 75% overlap. The vector spacing was 0.44 mm for FOV_1 and 0.80 mm for both FOV_2 and FOV_3. In-house MATLAB scripts were used to post-process the instantaneous velocity vectors.

3.4 Measurement Uncertainty

Uncertainty measurements in the streamwise mean velocities (U), Reynolds normal stresses ($\overline{u'u'}$ and $\overline{v'v'}$) and Reynolds shear stress ($\overline{u'v'}$) were performed using the procedure outlined by Sciacchitano and Wieneke (Sciacchitano and Wieneke, 2016), and Bendat and Piersol (Bendat and Piersol, 2011) as follows:

$$\xi_U = \frac{Z_c}{\sqrt{N}} \frac{u'_{rms}}{U_e} \tag{3.3}$$

$$\xi_{\overline{u_i' u_i'}} = Z_c \sqrt{\frac{2}{N} \frac{\overline{u_i' u_i'}}{U_e^2}} \tag{3.4}$$

$$\xi_{\overline{u'v'}} = Z_c \sqrt{\frac{1 + \rho_{uv}^2}{N - 1}} \tag{3.5}$$

Where Z_c is the confidence coefficient (i.e., Z_c = 1.96 for 95% confidence level), ρ_{uv} is the correlation coefficient where $\rho_{uv} = \overline{u'v'}/(u'_{rms} \times v'_{rms})$ and N is the effective number of samples. In time-resolved measurements, the samples are not statistically independent. Therefore, the effective number of samples collected over a period T is determined by $N = T/2\tau$, where τ represents the integral time scale. The uncertainties in the mean velocity, Reynolds normal stress, and Reynolds shear stresses are approximately 2%, 6% and 4% respectively.

4 Results and Discussion

This chapter presents and discusses the results of the current study and compares the current results to those of the uniform flow and wall-mounted cases. The discussion is categorized into six sections. Section 4.1 focuses on the mean flow field around the cylinders. The turbulence statistics, including the Reynolds stresses and turbulent kinetic energy (TKE), are analyzed in Section 4.2. Section 4.3 discusses probability density function (PDF) and joint probability density function (JPDF). Analysis of the streamwise evolution and profiles from the mean flow and turbulence statistics are presented in Section 4.4. Section 4.5 focuses on turbulence production and transport of TKE. Lastly, Section 4.6 presents discussion on frequency spectra and proper orthogonal decomposition (POD) of the velocity fluctuations.

4.1 Mean Flow

4.1.1 Contours of Mean Velocity

Contours of streamwise mean velocity and vertical mean velocity superimposed with mean streamlines to reveal the mean flow features are presented in Figure 4.1 and Figure A.2. In the streamwise mean velocity contours, the $U = 0$ isopleth is used to demarcate the reverse flow region ($U < 0$) and determine the attachment points on the cylinder surface and the free surface. For conciseness, four cases, AR1, AR2, AR4, and AR8 are shown to represent the various flow regimes observed. The plots for the other cases are shown in the Appendix. The mean flow features for AR2.5 are qualitatively similar to AR2, while AR3 and AR5 share similar features as AR4. The flow separates at the sharp leading edge of the cylinder, regardless of the aspect ratio. For AR1, the separated shear layer is shed directly into the wake region, forming a large recirculation bubble

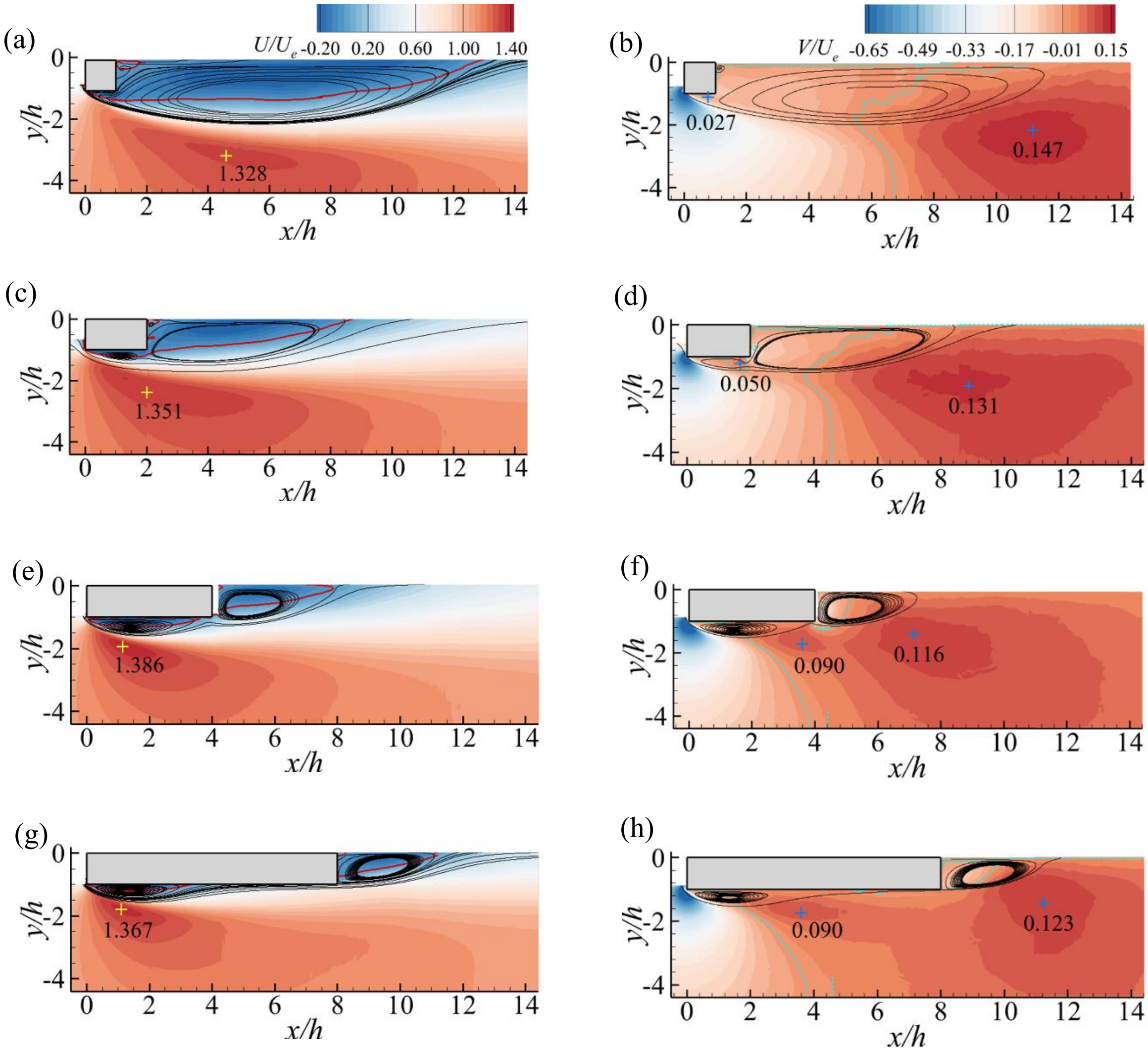

Figure 4.1 Contours of streamwise mean velocity (left) with $U = 0$ (red solid line) isopleth, and vertical mean velocity (right) with $V = 0$ isopleth (blue dashed line) and mean streamlines for (a, b) AR1, (c, d) AR2, (e, f) AR4, and (g, h) AR8. The (+) symbol denotes the location of the peak streamwise mean velocity with the magnitude.

spanning from the leading edge to the reattachment point on the free surface. In the case of AR2 and AR2.5, a recirculation bubble is formed on top of the cylinder coupled with another recirculation bubble in the wake, although there is no mean reattachment on the cylinders. This may signify the occurrence of intermittent reattachment of the separated shear layer onto the cylinders (Kumahor and Tachie, 2023a; Liu et al., 2024). In contrast, for AR ≥ 3, the separated shear layer from the leading edge reattaches onto the cylinder, and the attached shear layer subsequently separates from the trailing edge and reattaches on the free surface. In all cases, a secondary counter-rotating recirculation bubble forms behind the cylinder at the cylinder-free surface junction, however, the bubble is more pronounced as aspect ratio decreases. Moreover, the maximum mean velocity (U_{max}) of the accelerated flow over the cylinder increases for AR ≤ 4 but decreases for AR ≥ 4. The location of U_{max} moves closer to the leading edge ($x/h \in [1.25, 5.03]$) and surface of the cylinder ($y/h \in [-1.81, -3.19]$) as aspect ratio increases from AR1 to AR8.

Following previous studies on rectangular cylinders in uniform flow (Liu et al., 2024), AR3 is selected as the critical aspect ratio for the mean reattachment regime of the present free surface-mounted cylinders with Re = 11100, while AR2 and AR2.5 are categorized into the intermittent reattachment regime. The critical aspect ratio aligns with results reported for cylinders in uniform flow with Re ≥ 7200 and $BR \geq 7\%$ (Abdul-Salam et al., 2023; Liu et al., 2024). However, this value is lower than AR = 4 observed for wall-mounted cylinders in a thin boundary layer ($\delta/h \leq 1.37$) (van der Kindere and Ganapathisubramani, 2018) and higher than AR = 2 for those in a thick boundary layer ($\delta/h \geq 4.8$) (Fang and Tachie, 2019b; Chalmers et al., 2021).

A negative region of vertical mean velocity occurs near the leading edge regardless of aspect ratio, consistent with downward transport of high momentum fluid upon separation from the sharp leading edge. The positive region of V is linked to entrainment of ambient fluid into the separated shear layer (Addai et al., 2022). The $V = 0$ isopleth demarcates the regions of downward and upward mean flow deflections. The $V = 0$ isopleth in the wake is closer to the trailing edge of the cylinder for the reattached cylinders. There exists a positive region on the cylinder which increases in magnitude to an asymptotic value ($V/U_e = 0.090$) as aspect ratio increases. This positive region occurs in the reverse flow region for the unattached cylinders reducing the tendency of the separated shear layer reattaching onto the cylinder surface. Apart from AR8, the maximum V in the wake decreases with increasing aspect ratio. Consistent with the orientation of the separated shear layer, the results (particularly AR1) agree with the topology of semi-submerged circular cylinders (Addai et al., 2024).

4.1.2 Characterization of the recirculation bubbles

To characterize the effects of aspect ratio on the recirculation bubbles, the mean reattachment lengths on the cylinder (L_T/h) and in the wake (L_W/h) are shown in Figure 4.2. Previous results for wall-mounted and uniform flow cases (Bergeles and Athanassiadis, 1983; van der Kindere and Ganapathisubramani, 2018; Fang and Tachie, 2019b; Chalmers et al., 2021) are added to facilitate comparison. For the free surface-mounted cylinders, mean reattachment onto the cylinder occurs for AR ≥ 3, and the reattachment length L_T/h increased linearly from $L_T/h = 2.76$ for AR3 to a maximum value of $L_T/h = 4.20$ for AR5 followed by a reduction to $L_T/h = 3.39$ in the AR8. It is noteworthy that, the reattachment point for AR3-AR5 is $0.5h \pm 0.3h$ from the trailing edge of each cylinder, suggesting a strong interaction between the recirculation bubble on and behind the cylinder. However, the AR8 cylinder allowed for attachment and redevelopment, therefore suppressing interactions between the recirculation bubbles on and behind the cylinder, leading to a shorter L_T/h compared to AR4 and AR5. The reattachment length for AR3, AR4, and AR5 in the present study are comparable to results for cylinders in uniform flow with similar AR (Kumahor and Tachie, 2022; Liu et al., 2024). For the wall- mounted cylinders, the critical aspect ratio and L_T/h decreases with increasing δ/h, while L_T/h is independent of aspect ratio. The strong dependence of L_T/h on δ/h is attributed to the effects of turbulence intensity and mean shear, which are enhanced in thicker TBL, leading to reduced L_T/h (Fang and Tachie, 2019b; Chalmers et al., 2021). Accordingly, the L_T/h values for the present study are larger than values

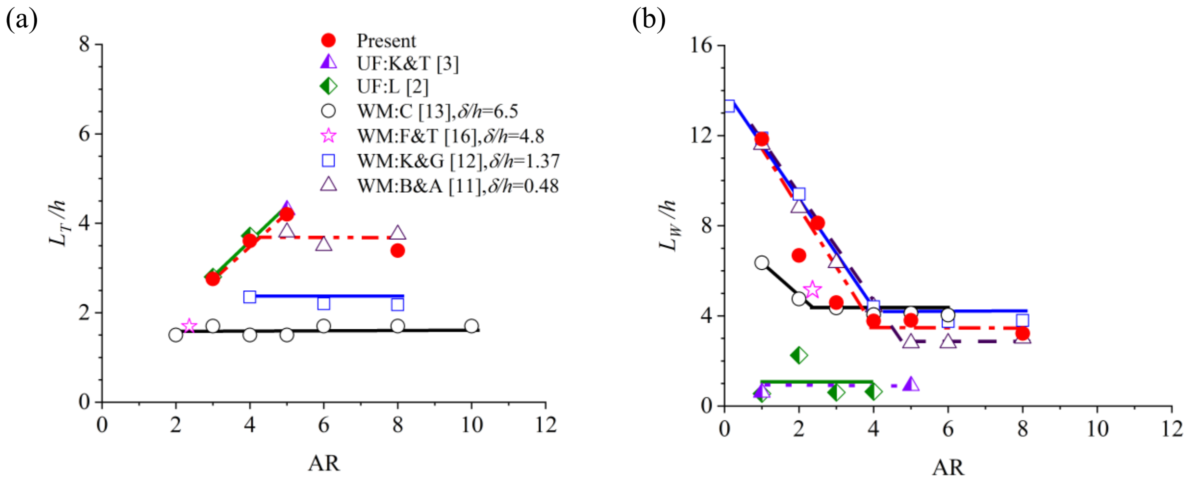

Figure 4.2 Variation of reattachment length (a) on the cylinder measured from the leading edge and (b) on the free surface measured from the trailing edge with aspect ratio. Wall-mounted and uniform flow cases are denoted by WM and UF respectively.

for the wall-mounted cylinders of $\delta/h > 0.48$, but comparable to those of $\delta/h = 0.48$, at similar aspect ratios. This is expected as the freestream turbulence intensity is low, and the mean shear is negligible for the present free surface cases and previous uniform flow studies (Kumahor and Tachie, 2022; Liu et al., 2024).

Figure 4.2(b) shows that the length of the wake recirculation bubble (L_W/h) tends to decrease as aspect ratio increases for AR1 to AR4 and asymptotes to $L_W/h = 3.5 \pm 0.3$. It is interesting to note that L_W/h for AR2.5 is larger than AR2 and AR3. The sudden increase in L_W/h for an aspect ratio that immediately precedes the critical aspect ratio has also been observed in previous uniform flow studies. For example, Kumahor and Tachie (2023a) and Liu et al. (2024) observed a sudden increase in L_W/h for AR2, which precedes the critical aspect ratio of AR3 for their uniform flow cases. This sudden increase in L_W/h may be attributed to the strong intermittency and interactions between the recirculation bubbles on and behind the cylinder as the flow transitions between the unattached and reattachment regimes.

The L_W/h values for the present free surface-mounted cylinders are substantially larger than the uniform flow cases (Kumahor and Tachie, 2022; Liu et al., 2024), but similar to those of the wall-mounted cylinders with low δ/h ($\delta/h = 0.48$ and 1.37) (Bergeles and Athanassiadis, 1983; van der Kindere and Ganapathisubramani, 2018). Additionally, the L_W/h for the free surface-mounted cylinders (AR3-AR5) in the reattachment regime are in good agreement with the corresponding wall-mounted cylinders subjected to a thicker TBL ($\delta/h = 6.5$) (Chalmers et al., 2021). The results of L_T/h and L_W/h reveal that the reattachment mechanism onto the free surface-mounted cylinder is similar to the uniform flow cases (Figure 4.2(a)) since in both cases, the cylinders are exposed to a uniform flow. In contrast, the kinematic boundary condition of the free surface results in wake dynamics that are similar to the wall-mounted cylinders (Figure 4.2(b)) provided the approach boundary layer thickness is relatively thin or the cylinder is in the reattachment regime for relatively thick boundary layers. The reduced L_W/h for cylinders in a uniform flow is due to flow separation at both the upper and lower edges which combine behind the cylinder, forming a pair of counter-rotating recirculation bubbles. These counter-rotating bubbles entrain more surrounding high-momentum fluid, thereby reducing their sizes compared to bubbles attached to a boundary.

4.2 Reynolds Stresses and Turbulent Kinetic Energy

4.2.1 Reynolds Normal Stresses

The Reynolds stresses and turbulent kinetic energy are used to examine the effects of aspect ratio on the turbulence characteristics. The streamwise and vertical Reynolds normal stresses, $\overline{u'u'}$ and $\overline{v'v'}$, are shown in Figure 4.3 and Figure A.3. Each of the Reynolds normal stresses reveals two peaks, one in the leading-edge separated shear layer and the other in the wake, regardless of the flow regime. For $\overline{u'u'}$, the peak in the leading-edge separated shear layer is comparatively stronger than the peak in the wake and increases with increasing aspect ratio. This observation is attributed to the enhancement of the mean shear ($\partial U/\partial y$) due to the formation of the recirculation bubbles on the cylinder as the aspect ratio increases. In contrast, the peak in the wake decreases with increasing aspect ratio, in agreement with reduction in mean shear due to the reduced size of the wake recirculation bubbles as aspect ratio increases. The presence of the $\overline{u'u'}$ peaks aligns with those in uniform flow and wall-mounted studies (Essel et al., 2015; Essel and Tachie, 2017; Chalmers et al., 2021, 2022; Liu et al., 2024). For the uniform flow cases, Liu et al. (2024) observed that the $\overline{u'u'}$ peak for AR1 was the largest and those for AR2, AR3, and AR4 are not considerably different from one another. However, the peak in the present study shows aspect ratio dependency with the maximum occurring on the AR8 cylinder.

For rectangular cylinders placed in a uniform flow, the maximum $\overline{v'v'}$ is located on the centerline in the wake region due to the alternate vortex shedding from either side of the cylinder and $\overline{v'v'}$ peak is greater than the maximum $\overline{u'u'}$ (Kumahor and Tachie, 2022; Liu et al., 2024). In the present study, the $\overline{v'v'}$ peak is located in the separated shear layer in the wake for the short cylinders (AR < 4), and on top of the cylinder for AR ≥ 4. The dominant Reynolds normal stress is the $\overline{u'u'}$ due to the absence of alternating vortex shedding from either side of the free surface-mounted cylinders, with the magnitude of $\overline{v'v'}$ peaking 2 to 3 times smaller than $\overline{u'u'}$. The $\overline{v'v'}$ peak in the leading-edge shear layer increases with increasing aspect ratio from AR1 to AR4 but are similar in magnitude for AR ≥ 4. In the wake, the peak values for AR ≤ 4 are similar but decrease as aspect ratio increases for AR ≥ 4. For wall-mounted cylinders, Chalmers et al. (2021) noted two $\overline{v'v'}$ peaks close to the leading edge, one upstream of the leading edge and the other on top of the cylinder. In contrast to the present study, due to the negligible mean shear upstream of the cylinder,

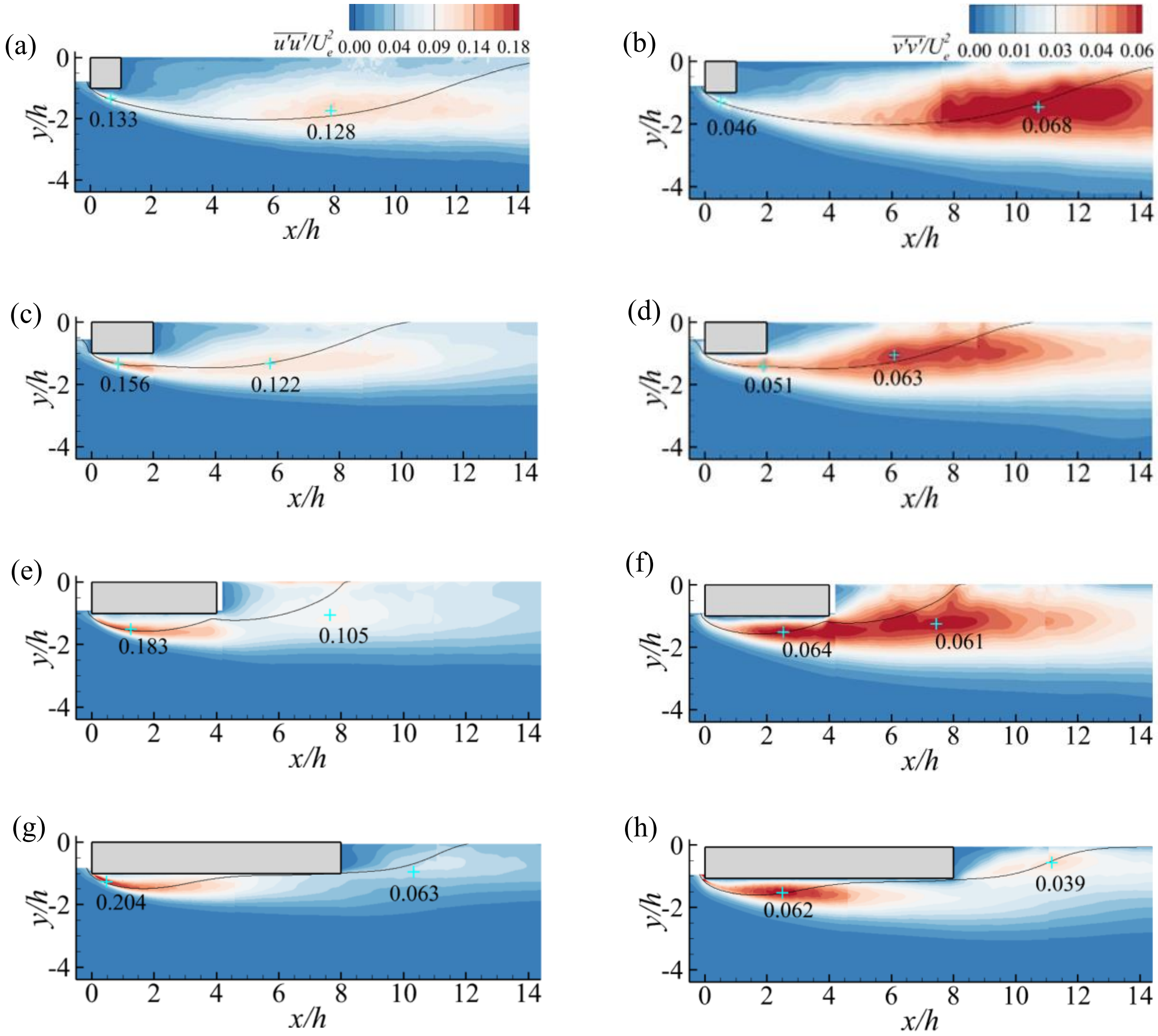

Figure 4.3 Contours of streamwise Reynolds normal stress, $\overline{u'u'}$ (left) and vertical Reynolds normal stress, $\overline{v'v'}$ (right) and mean streamline for (a, b) AR1, (c, d) AR2, (e, f) AR4, and (g, h) AR8.

no $\overline{v'v'}$ peak was formed upstream of the cylinder. Elevated regions of $\overline{v'v'}$ also emanates in the wake region of the wall-mounted cylinders along the shear layer as the flow reattaches onto the wall behind the cylinder (Chalmers et al., 2021, 2022). This is comparable to the present study as the separated flow reattaches onto the free surface. It was also reported that higher Reynolds stresses occur in the leading-edge separated shear layer for the wall-mounted cylinder (Chalmers et al., 2021), and $\overline{u'u'}$ >> $\overline{v'v'}$ similar to the free surface-mounted cylinders.

4.2.2 Reynolds Shear Stress and Turbulent Kinetic Energy

Figure 4.4 and Figure A.4 show contours of the Reynolds shear stress $\overline{u'v'}$ and turbulent kinetic energy (TKE). The negative peak of the Reynolds shear stress in the leading-edge separated shear layer tends to increase in magnitude with increasing aspect ratio but the positive peaks in the separated shear layers over the cylinder and in the wake ($\overline{u'v'}/U_e$= 0.046 ± 0.007) are independent of aspect ratio. Also, the maximum positive peak is located closer to the leading edge as aspect ratio increases. Based on the orientation of the shear layer, the signs of $\overline{u'v'}$ near the leading edge and in the separated shear layers over and behind the cylinders are consistent with previous uniform flow (Kumahor and Tachie, 2023a; M. Liu et al., 2024) and wall-mounted studies (Essel et al., 2015; Fang and Tachie, 2019b; Chalmers et al., 2021). For the cylinder in a uniform flow, an additional intense region of $\overline{u'v'}$ was observed in the recirculation bubbles behind the cylinder, with peaks that increase with decreasing aspect ratio (Liu et al., 2024). This intense $\overline{u'v'}$ region may be an artefact of the alternating vortex shedding from either side of the cylinder in a uniform flow, which is more pronounced as aspect ratio decreases.

The TKE is estimated as $k = 0.5(\overline{u'u'} + \overline{v'v'})$, since a planar PIV without measurements for the spanwise velocity is employed in this study. Similar to the behavior of the Reynolds normal stresses (especially $\overline{u'u'}$), the maximum TKE in the wake decreases as aspect ratio increases while the peak in the leading edge separated shear layer increases as aspect ratio increases. The topology of the TKE is different from those observed in uniform flow cases at similar AR. For example, the maximum TKE for AR1 in the uniform flow is located on the centerline (Kumahor and Tachie, 2023a; Liu et al., 2024), while that of the free surface-mounted cylinder is in the separated shear layer. As aspect ratio increases, the peak TKE for cylinders in uniform flow is drawn into the separated shear layer and decreases, eventually approaching the topology observed for the free

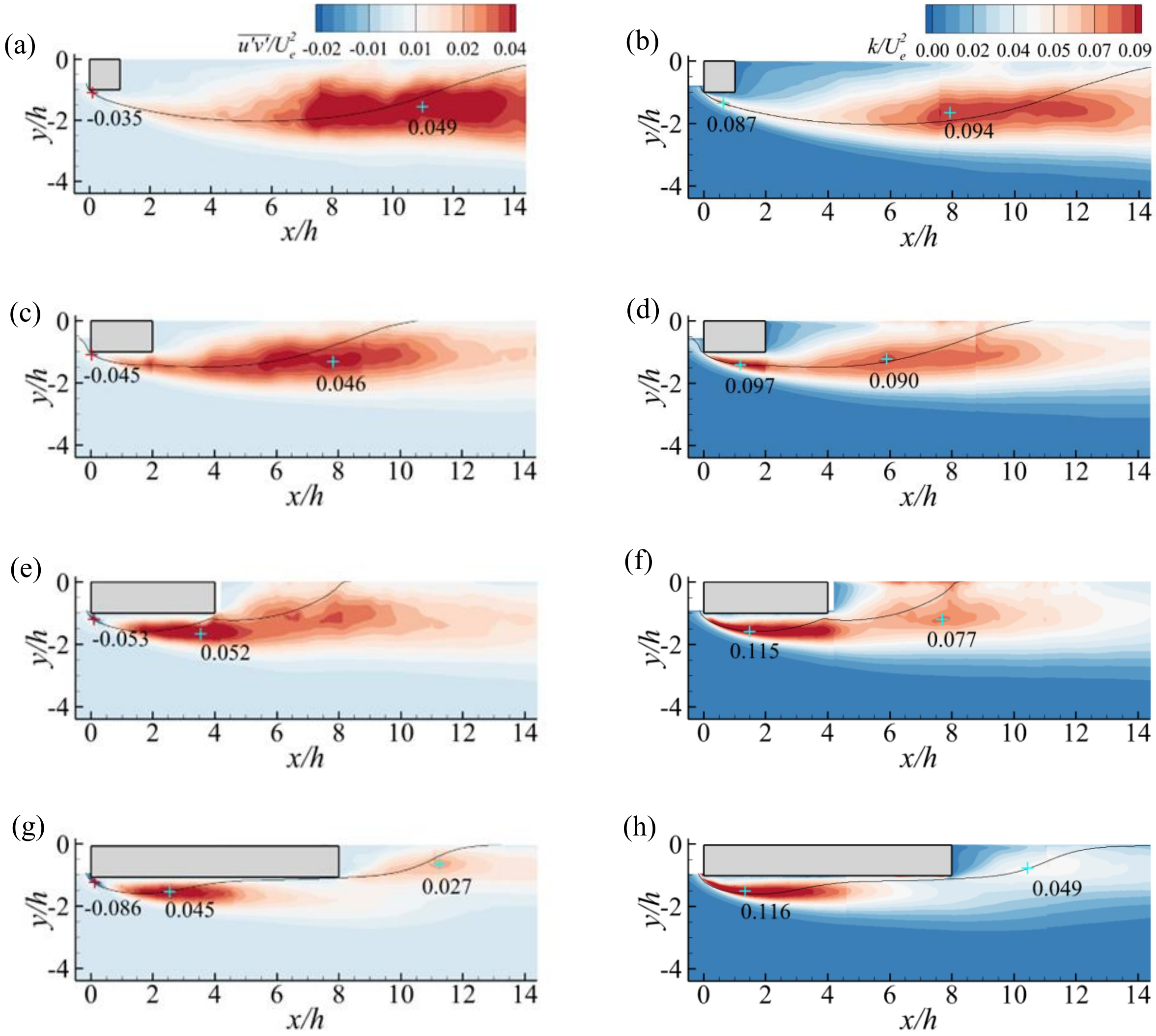

Figure 4.4 Contours of Reynolds shear stress, $\overline{u'v'}$ (left) and turbulent kinetic energy, $k = 0.5(\overline{u'u'} + \overline{v'v'})$ (right) and mean streamline for (a, b) AR1, (c, d) AR2, (e, f) AR4, and (g, h) AR8.

surface-mounted cylinders. This observation is consistent with the reduced dominance of $\overline{v'v'}$ due to associated decrease in strength of the alternating vortex shedding as the aspect ratio of the cylinders in the uniform flow increases (Kumahor and Tachie, 2023a; Liu et al., 2024). van der Kindere and Ganapathisubramani (2018) reported that the maximum TKE in the wake of the wall-mounted cylinders decreases as aspect ratio increases, similar to the present study.

4.3 Probability Density Functions and Joint Probability Density Functions

4.3.1 Probability Density Functions

To investigate the effect of aspect ratio on the dynamics of the separated shear layer, the probability density functions (PDF) of the streamwise velocity fluctuations (u') at the maximum $\overline{u'u'}$ (on top of the cylinder) and the vertical velocity fluctuations (v') at the maximum $\overline{v'v'}$ (in the wake), are presented in Figure 4.5 and Figure A.5. In general, the PDFs of both u' and v' show unimodal distributions and are close to a Gaussian distribution (especially at maximum $\overline{u'u'}$). The PDF at maximum $\overline{u'u'}$ on the cylinder are similar for AR1 and AR2. However, as aspect ratio increases, the probability of negative u' increases, particularly for AR8. This indicates frequent deceleration of the separated flow. The PDF in the wake reveals a higher probability of positive v' in the wake region regardless of the aspect ratio. Kumahor and Tachie (2022) observed a unimodal distribution for AR1 (u') and AR5 (u' and v') in a uniform flow, but bimodal distribution for the v' of AR1 along the centerline in the wake region where maximum $\overline{v'v'}$ is located. Liu et al. (2024) reported unimodal distribution of u' for AR2 (except for Re = 21000), AR3, and AR4 at maximum $\overline{u'u'}$, and bimodal distributions of v' at maximum $\overline{v'v'}$ (in the wake region along the centerline) for AR1, AR3, and AR4 at Re ≥ 7200. Due to lack of flow over the top of the cylinder, limiting alternating vortex shedding over the cylinder, this was not observed in the present study.

4.3.2 Joint-Probability Density Functions

The joint-PDF (JPDF) is used to investigate the interaction between the fluctuating velocities (u' and v') at the maximum $\overline{u'v'}$ location and is presented in Figure 4.6 and Figure A.6. The axes

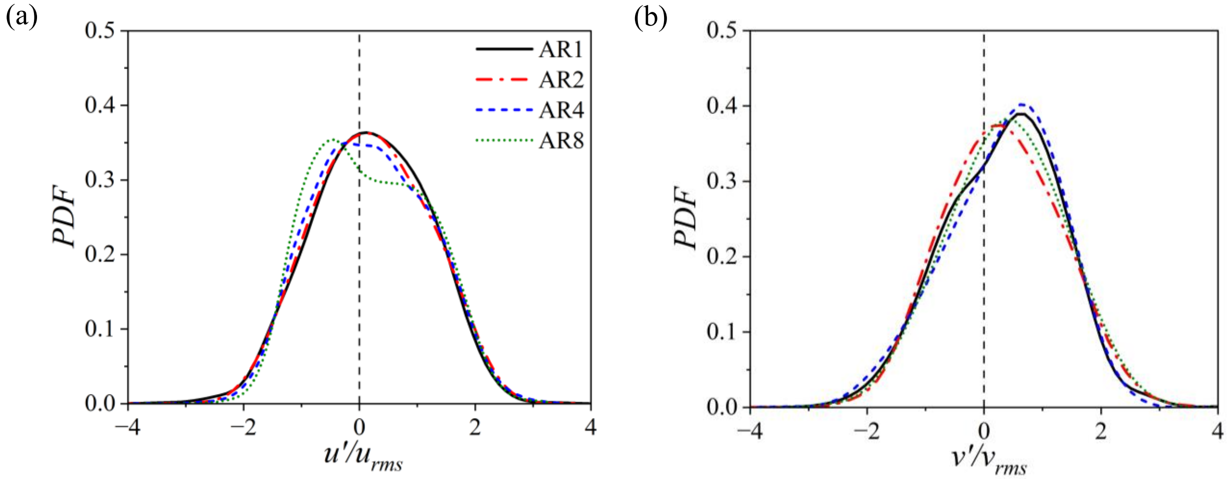

Figure 4.5 Probability density functions of u' at maximum $\overline{u'u'}$ (a) on top of the cylinder and (b) maximum $\overline{v'v'}$ in the wake for AR1, AR2, AR4, and AR8.

divide the JPDF into four quadrants: Q1$(+u', +v')$, Q2$(-u', +v')$, Q3$(-u', -v')$, and Q4$(+u', -v')$, and the percentage contributions of each quadrant is shown on the plot. Here, quadrants with positive u' (Q1 and Q4) indicate regions of high-momentum fluid, while those with negative u' (Q2 and Q3) represent low-momentum fluid. Considering the orientation of the shear layer, quadrants with positive v' (Q1 and Q2) signify fluid entrainment towards the cylinder or free surface, whereas negative v' quadrants (Q3 and Q4) indicate fluid ejection away from the cylinder or free surface.

In Figure 4.6, the JPDF show strong skewness towards the Q1-Q3 events, signifying the occurrence of intermittent entrainment of high-momentum fluid into the shear layer (Q1) and ejection of low-momentum fluid away from the cylinder or free surface (Q3). The dominance of Q1-Q3 events is consistent with the orientation of the present mean shear ($\partial U/\partial y$), as an opposite orientation, typically observed for wall-mounted cylinders, results in dominant Q2-Q4 events. The results show that Q1 and Q3 contribute almost equally as aspect ratio increases from AR1 to AR2,

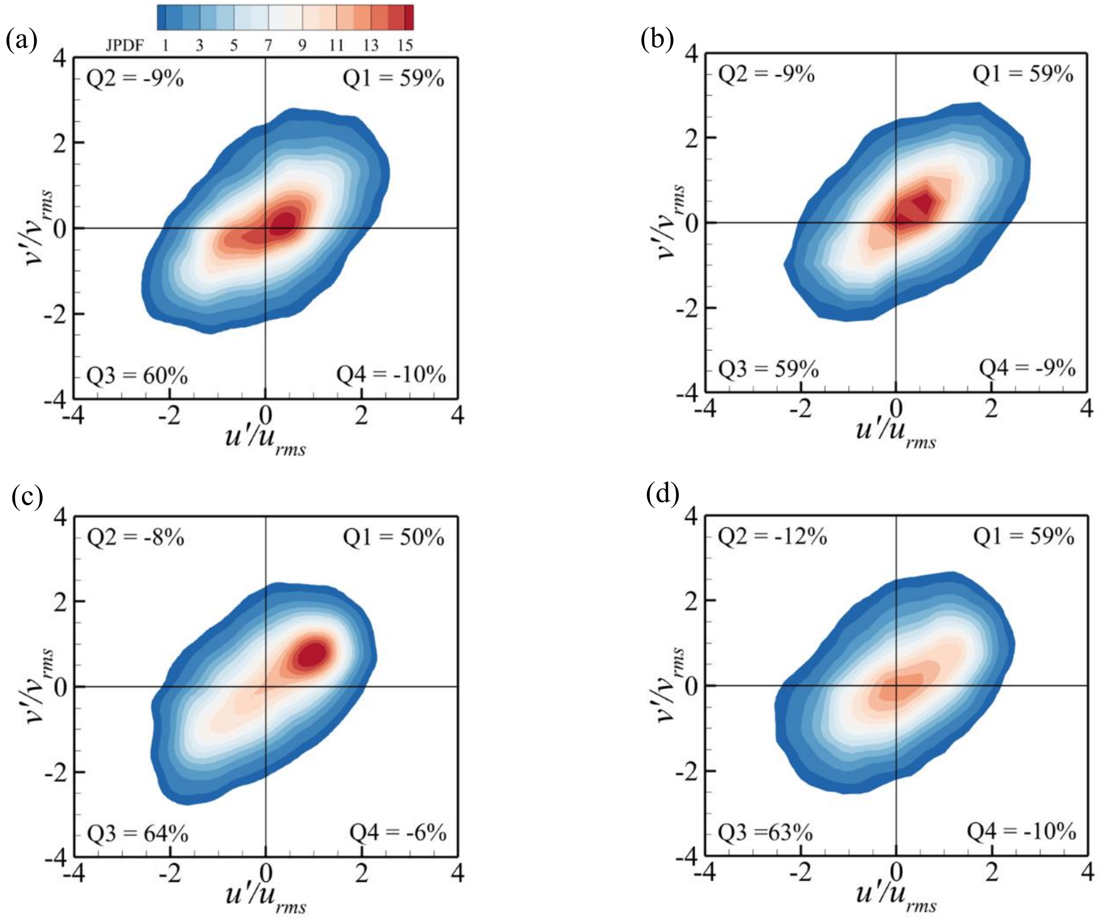

Figure 4.6 Joint probability density function of velocity fluctuations at maximum $\overline{u'v'}$ for (a) AR1, (b) AR2, (c) AR4, (d) AR8.

and the same is seen for Q2 and Q4. Meanwhile, for the cylinders in the reattachment regime (AR3-AR8), the contribution of Q3 events outweighs that of Q1 events.

4.4 Analysis on Streamwise evolution and comparison of Mean Velocities and Turbulence Statistics

The streamwise evolution of the maximum Reynolds stresses ($\overline{u'u'}$, $\overline{v'v'}$, and $\overline{u'v'}$) over the cylinder, and in the wake region are presented in Figure 4.7 and Figure A.7. The profiles on top of the cylinder are normalized by the length of the cylinder, *x*/*L* (Figure 4.7(a, c, e)), while in the

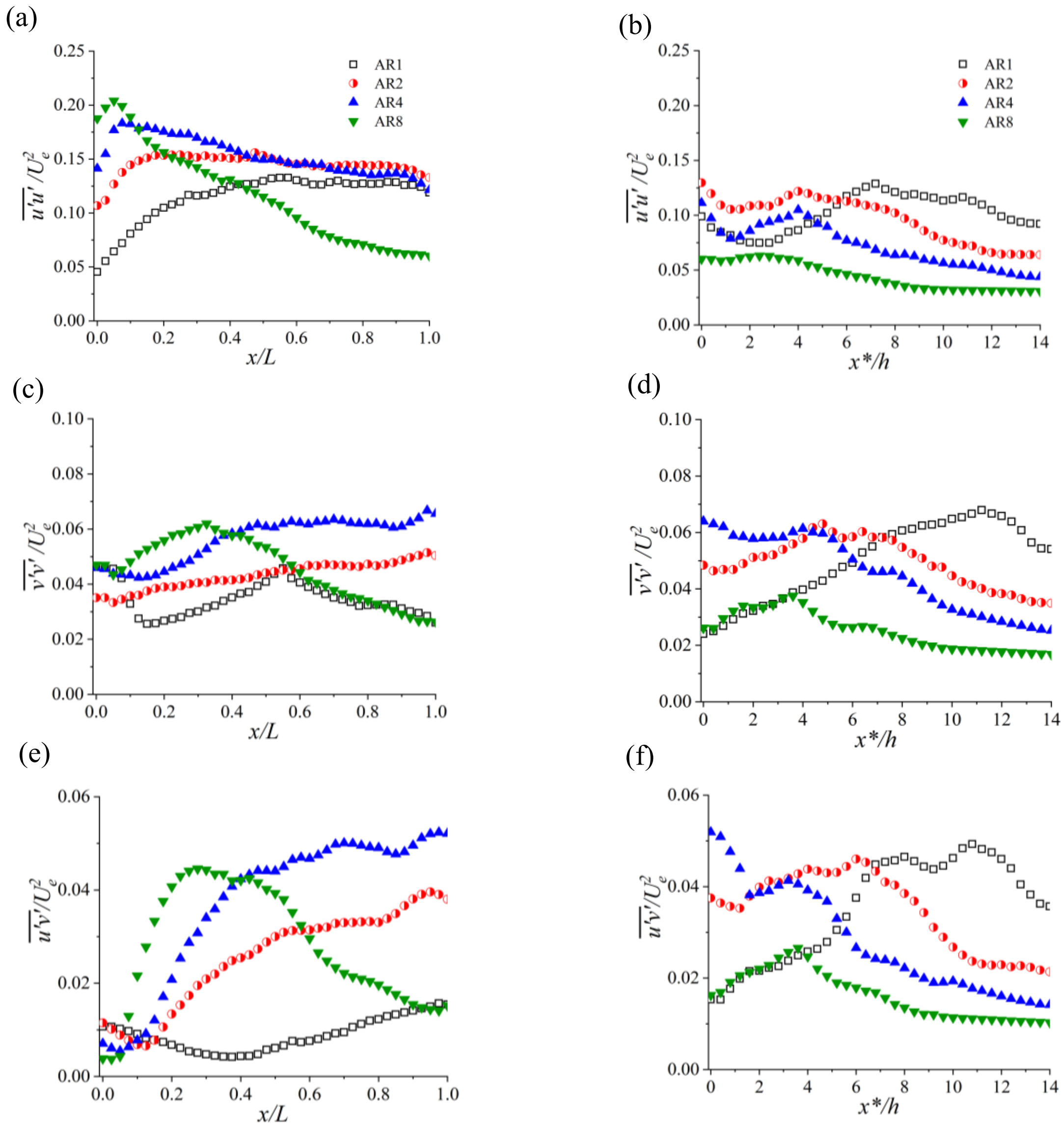

Figure 4.7 Streamwise variation of maximum Reynolds stresses for AR1, AR2, AR4, and AR8. *x/L* – Streamwise length along the cylinder length, *x*/h* – Streamwise length from the trailing edge of the cylinder.

wake region, the origin was set to the trailing edge ($x^*/h = 0$) and the profiles normalized by the cylinder height to facilitate comparison. The maximum Reynolds stresses exhibit a rapid increase from the leading edge to a peak on top of the cylinder, followed by a brief decay and then a second peak near the reattachment point on the free surface. Beyond this peak, the stress gradually decreases. The streamwise distance from the separation point to the peak of $\overline{u'u'}$ is often used to estimate the vortex formation length (Nakagawa et al., 1999; Liu et al., 2024). Figure 4.7(a) demonstrates that the vortex formation length on top of the cylinder decreases from $x/L = 1.00$ to 0.05 as the aspect ratio increases from AR1 to AR8. In the wake region, as the aspect ratio decreases, the second peak of $\overline{u'u'}$ is more pronounced and shifts further downstream.

Apart from AR8, the maximum $\overline{v'v'}$ and $\overline{u'v'}$ tend to increase with increasing aspect ratio along the length of the cylinder. Due to the shorter reattachment length relative to the length of the AR8 cylinder, $\overline{v'v'}$ and $\overline{u'v'}$ peaks decrease gradually from $x/L = 0.3$ towards the trailing edge as a boundary layer develops on the cylinder. In the wake, the maximum Reynolds stresses tend to decrease with increasing aspect ratio for $x^*/h \geq 6$. The $\overline{v'v'}$ peaks in the range $x^*/h \in [2, 6]$ for AR ≥ 4 show similar profiles but different magnitudes. The maximum $\overline{v'v'}$ and $\overline{u'v'}$ in the wake occur closer to the trailing edge as aspect ratio increases. Similar $\overline{v'v'}$ and $\overline{u'v'}$ peaks are observed for AR1 and AR8 within $x^*/h \in [2, 4]$. Chalmers et al. (2021) examined the streamwise evolution of the maximum Reynolds stresses for AR1, AR2, AR4 and AR6. A monotonic decrease in the magnitudes of the maximum Reynolds stresses was observed for $x/h > 2.5$, although the profiles at $x/h \leq 2.5$ were not significantly affected by aspect ratio. This is at variance with the present study due to the difference in the turbulence levels of the oncoming flow.

The streamwise evolution of the wall-normal location of the maximum Reynolds normal stresses can be used to characterize the trajectory of the separated shear layer (Moore et al., 2019a). Here, the trajectory of both the Reynolds normal and shear stresses are presented in Figure 4.8 and Figure A.8. On top of the cylinder, the profiles for AR1 and AR2 collapse on each other, whereas the profiles for AR4 and AR8 differ, particularly $\overline{u'u'}_{max}$ for AR8, due to the reattachment of the separated shear layer. In the wake, the trajectory of the Reynolds stresses shifts closer to the free

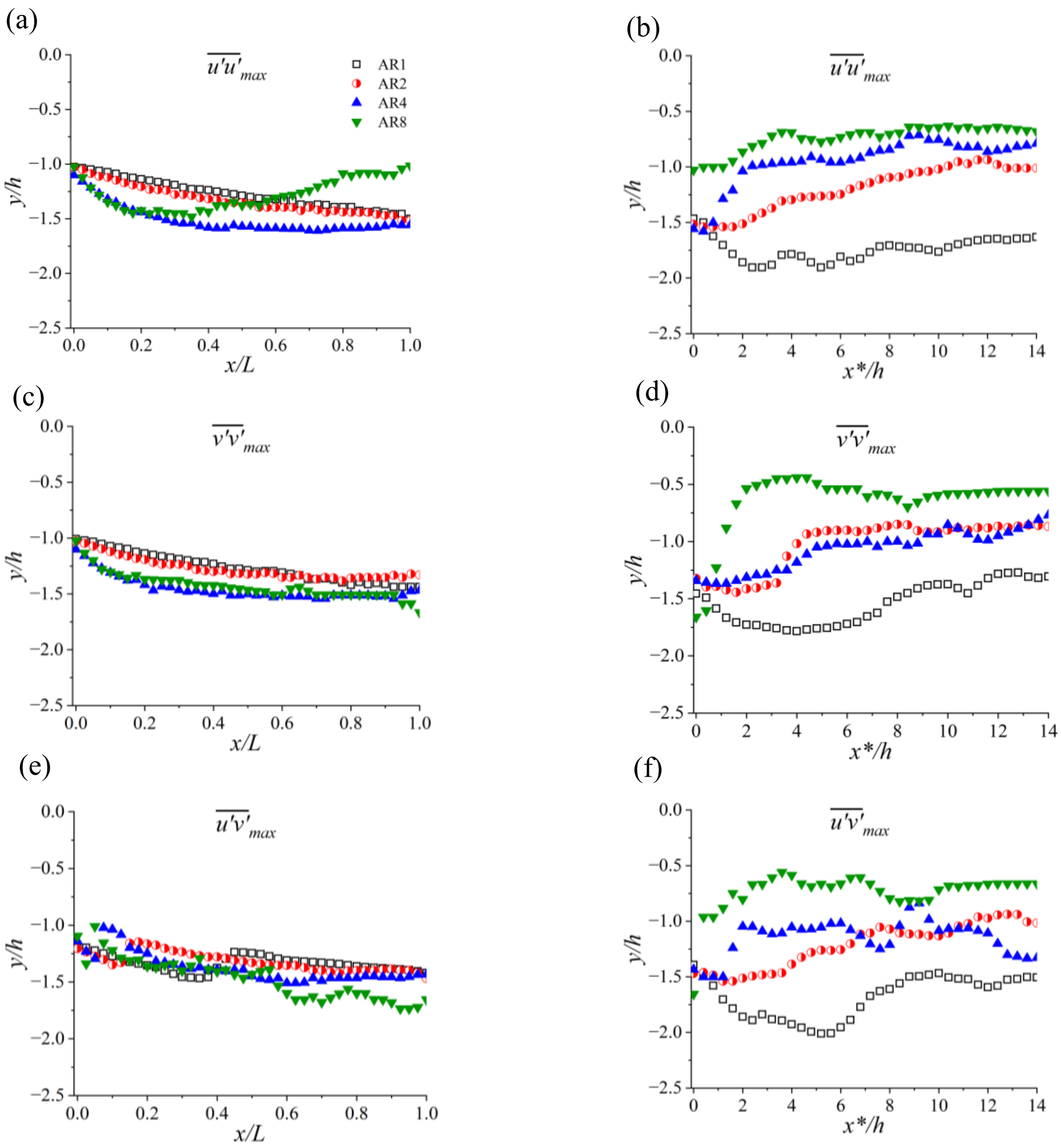

Figure 4.8 Streamwise variation of vertical location of the maximum Reynolds stresses for AR1, AR2, AR4, and AR8. *x/L* – Streamwise length along the cylinder length, *x*/h* – Streamwise length from the trailing edge of the cylinder.

surface with increasing aspect ratio. These observations are expected, as the trajectory of the separated shear layer is strongly influenced by the recirculation regions.

Figure 4.9 and Figure A.9 shows vertical profiles of the streamwise mean velocity and TKE at selected streamwise locations. The results for AR1 and AR4 are compared to profiles from the

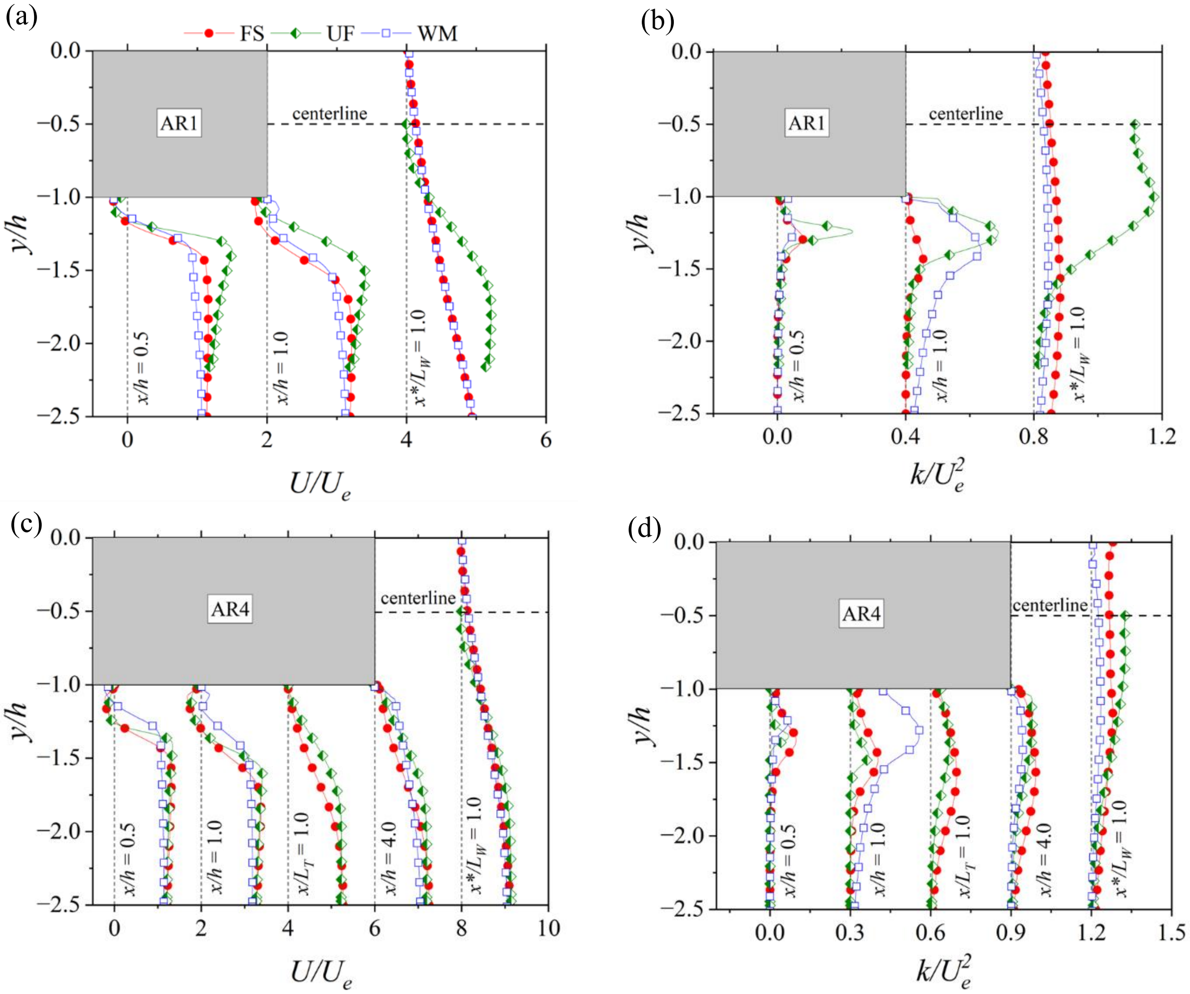

Figure 4.9 Profiles of streamwise mean velocity (*U*) (left), and TKE (right) at selected streamwise locations for AR1, and AR4, where $x/L_T = 1.0$ and $x^*/L_W = 1.0$ are the reattachment points on the cylinder and in the wake, respectively. FS (Free surface), WM (Wall-mounted) and UF (Uniform flow).

uniform flow case by Liu et al. (2024) and wall-mounted cylinder case by van der Kindere and Ganapathisubramani (2018) to highlight the major differences among the three boundary conditions for both unattached (AR1) and reattached (AR4) cylinders. Note that the TKE was evaluated as $k = 0.5(\overline{u'u'} + \overline{v'v'})$ in each study. The mean velocity profiles for AR4 are comparable for the three boundary conditions, however, for AR1, the profiles for the uniform flow cases are enhanced in the region $y/h \in [-1.30, -2.10]$ compared to the free surface and wall-mounted cases. For AR1, the TKE is strongest in the uniform flow, especially in the wake region, due to the enhancement of $\overline{v'v'}$ by the alternating vortex shedding from both sides of the cylinder. As expected, the peak of the TKE for AR1 is also larger for the wall-mounted case than the free surface-mounted case. However, for AR4, the disparity in the TKE profiles for the three boundary conditions is significantly reduced.

4.5 Turbulence Production and Transport of TKE

4.5.1 Turbulence Production

Contours of the production term (P_k) in the transport equation of TKE are shown in Figure 4.10 and Figure A.10. Since the mean flow is homogeneous in the spanwise direction, the production term reduces to:

$$P_k = -\overline{u'u'}\frac{\partial U}{\partial x} - \overline{v'v'}\frac{\partial V}{\partial y} - \overline{u'v'}\frac{\partial U}{\partial y} - \overline{u'v'}\frac{\partial V}{\partial x} \tag{1}$$

The peak regions of P_k are located along the shear layer and coincide with regions of elevated Reynolds stresses (particularly $\overline{u'u'}$) peak on top of the cylinder (Figure 4.3 and Figure 4.4). Apart from AR1, the peak magnitude is independent of aspect ratio and falls within $P_k = 0.49 \pm 0.03$. Another positive peak P_k occurs downstream of the trailing edge of the AR8 cylinder. Negative peaks of P_k occur in a small region close to the leading edge (*x/h* < 0.06). Liu et al. (2024) and Kumahor and Tachie (2022) examined the production term for rectangular cylinders in a uniform flow, and observed that majority of the flow field exhibited positive turbulence production (i.e., energy source), which is similar to the present study. They also observed negative regions of production (energy sink) close to the leading edge of a cylinder in a uniform flow (Cimarelli et al., 2018; Kumahor and Tachie, 2022; Liu et al., 2024). A similar observation was reported by

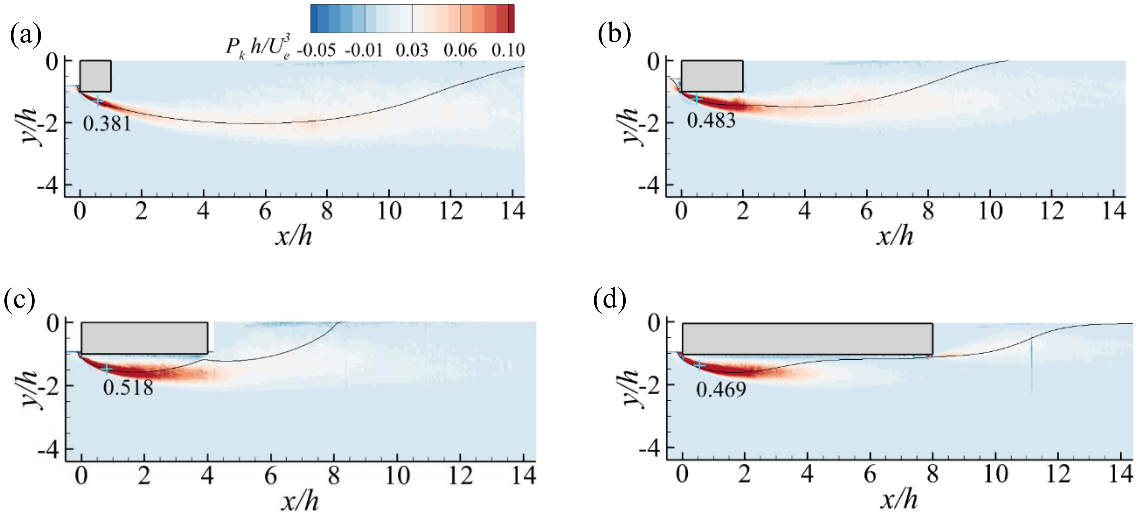

Figure 4.10 Contours of production of turbulent kinetic energy, P_k, and mean streamline for (a) AR1, (b) AR2, (c) AR4, and (d) AR8.

Essel et al. (2015) for a wall-mounted cylinder. Liu et al. (2024) and Kumahor and Tachie (2022) also observed the highest P_k peak for the AR1 cylinder and is an order of magnitude larger than the other cylinders. In contrast, AR1 for the present study exhibit the smallest peak value due to the weaker Reynolds stresses produced on top of the cylinder compared to AR > 1.

The contributions from the individual components in the production term extracted at the maximum P_k, maximum TKE on the cylinder and in the wake are investigated along the vertical direction as shown in Figure 4.11 and Figure A.11 to further investigate the effect of aspect ratio on the contributions of the individual components to the production of TKE. The contributions of these components are similar for cases in each regime, therefore the profiles for AR1, AR2, and AR4 are shown in Figure 4.11 for brevity. The results show that $-\overline{u'u'}\frac{\partial U}{\partial x}$ acts as the primary energy source irrespective of aspect ratio at both the peak locations of P_k and TKE on the cylinder. The positive contribution by $-\overline{u'u'}\frac{\partial U}{\partial x}$ at maximum P_k increases with increasing aspect ratio for AR ≤ 4 and is independent of aspect ratio for the other cylinders. The $-\overline{u'v'}\frac{\partial V}{\partial x}$ term contributes positively as a secondary energy source of turbulence production at the P_k peak location, due to the positively valued $\frac{\partial V}{\partial x}$ and negative $\overline{u'v'}$ close to the leading edge upon separation. Both the $-\overline{v'v'}\frac{\partial V}{\partial y}$ and $-\overline{u'v'}\frac{\partial U}{\partial y}$ terms contribute significantly as energy sinks at maximum P_k. For AR4 and AR8, the negative contribution of $-\overline{u'v'}\frac{\partial U}{\partial y} > -\overline{v'v'}\frac{\partial V}{\partial y}$. The TKE peak location on the cylinder coincides with a positive $\overline{u'v'}$, $\frac{\partial V}{\partial x} > 0$, and $\frac{\partial U}{\partial y} < 0$, which causes the $-\overline{u'v'}\frac{\partial V}{\partial x}$ term to act as an energy sink but negligible, and the $-\overline{u'v'}\frac{\partial U}{\partial y}$ term acts as a secondary energy source for AR1 but the primary source for AR ≥ 2. The contributions by the $-\overline{u'u'}\frac{\partial U}{\partial x}$ and $-\overline{v'v'}\frac{\partial V}{\partial y}$ terms are the greatest for AR1 at the TKE peak location on the cylinder since the peak location occurs close to the maximum $\overline{u'u'}$ and $\overline{v'v'}$ locations on the cylinder. The $-\overline{u'v'}\frac{\partial U}{\partial y}$ at the maximum TKE in the wake is the primary energy source, driven by the positive $\overline{u'v'}$ and negative $\frac{\partial U}{\partial y}$. This is in agreement with the observation by Addai et al. (2024) where the $-\overline{u'v'}\frac{\partial U}{\partial y}$ is the primary energy source in the wake of semi-submerged circular cylinders. Furthermore, the magnitudes of $-\overline{u'v'}\frac{\partial U}{\partial y}$ and total production in the wake are greater for AR ≤ 2 compared to the longer cylinders, and the magnitudes are nearly independent of aspect ratio within each of the two regimes (attached and unattached). In Figure 4.11(g - i), the $-\overline{u'u'}\frac{\partial U}{\partial x}$ and $-\overline{v'v'}\frac{\partial V}{\partial y}$ terms switch sign into energy sink and source, respectively. For cylinders in a uniform flow, it was reported that at the maximum P_k location above the cylinder, the $-\overline{u'u'}\frac{\partial U}{\partial x}$ as well as $-\overline{u'v'}\frac{\partial U}{\partial y}$ (AR ≥ 2) contribute significantly as the primary energy source, while $-\overline{u'v'}\frac{\partial V}{\partial x}$ acts as a secondary energy source but negligibly small (Liu et al., 2024). Addai et al. (2024) also found that $-\overline{u'v'}\frac{\partial V}{\partial x}$ is negligibly small at the

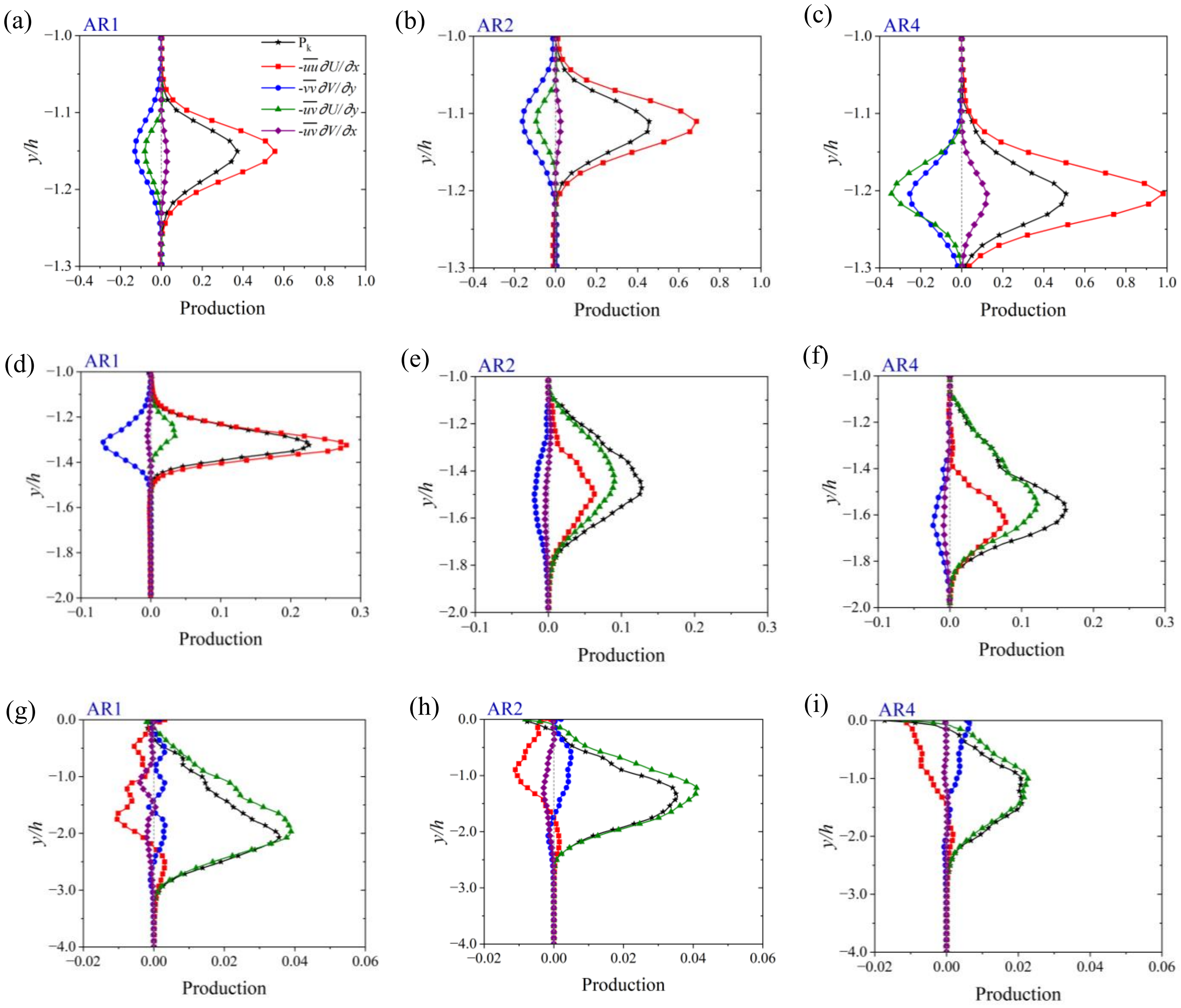

Figure 4.11 Profiles of the individual production terms at (a - c) maximum P_k, maximum (d - f) TKE on top of the cylinder and (g - i) in the wake for AR1 (left), AR2 (middle), and AR4 (right).

maximum TKE location for a semi-submerged circular cylinder. The contributions in the wake at maximum $\overline{v'v'}$ in the uniform flow are similar to the present study, except for $-\overline{v'v'}\frac{\partial V}{\partial y} > -\overline{u'v'}\frac{\partial U}{\partial y}$. The results from the present study indicate that the behavior observed at the free surface under the free slip condition closely resembles that of the centerline in a uniform flow.

4.5.2 Turbulence Transport

The transport of TKE has been used in previous investigations of turbulent shear flows to examine the turbulent transport of Reynolds stresses and TKE. Specifically, $\overline{ku'}$, estimated as ($\overline{u'u'u'}$ + $\overline{u'v'v'}$), measures the transport of TKE ($\overline{u'u'}$ + $\overline{v'v'}$) by u'. Similarly, $\overline{kv'}$, estimated as ($\overline{u'u'v'}$ + $\overline{v'v'v'}$), measures the transport of TKE by v'. Contours of $\overline{ku'}$ and $\overline{kv'}$, superimposed with traces of the center of the mean shear layer are presented in Figure 4.12 and Figure A.12. The center of the mean shear layer lies between the positive and negative regions irrespective of aspect ratio. The positive regions of both $\overline{ku'}$ and $\overline{kv'}$ are observed above the mean shear layer while the negative regions are observed below it. Since $\overline{u'u'}$and $\overline{v'v'}$ are both positive, positive regions signify sweep events (u'>0 and v'>0) or transport of TKE along the separated shear layer by high-speed fluid towards the free/cylinder surface. On the other hand, negative regions signify ejection events (u'<0 and v'<0) or transport of TKE by low-speed fluid downwards into the freestream. The switching of dominance between ejection and sweep events has been observed along the mean separating streamline in previous studies in the uniform flow (Kumahor and Tachie, 2022; Liu et al., 2024), wall-mounted (Fang and Tachie, 2020; Chalmers et al., 2021), submerged square cylinder in a TBL with varying gap ratios (Addai et al., 2022; Chalmers et al., 2023), and semi-submerged circular cylinders (Addai et al., 2024). Similar to the distribution of Reynolds stresses and TKE (Figure 4.3, Figure 4.4), higher levels of events, particularly ejection events, occur in the wake of the shorter cylinders but shift to beneath the cylinder as aspect ratio increases. Higher levels of sweep events occur in the AR2 case compared to the other cylinders. In all cases, the transport by sweep events is less intense than the transport by ejection events. In addition, the elevated regions of $\overline{ku'}$ are more intense than $\overline{kv'}$. This is consistent with the studies on semi-submerged circular cylinders (Addai et al., 2024).

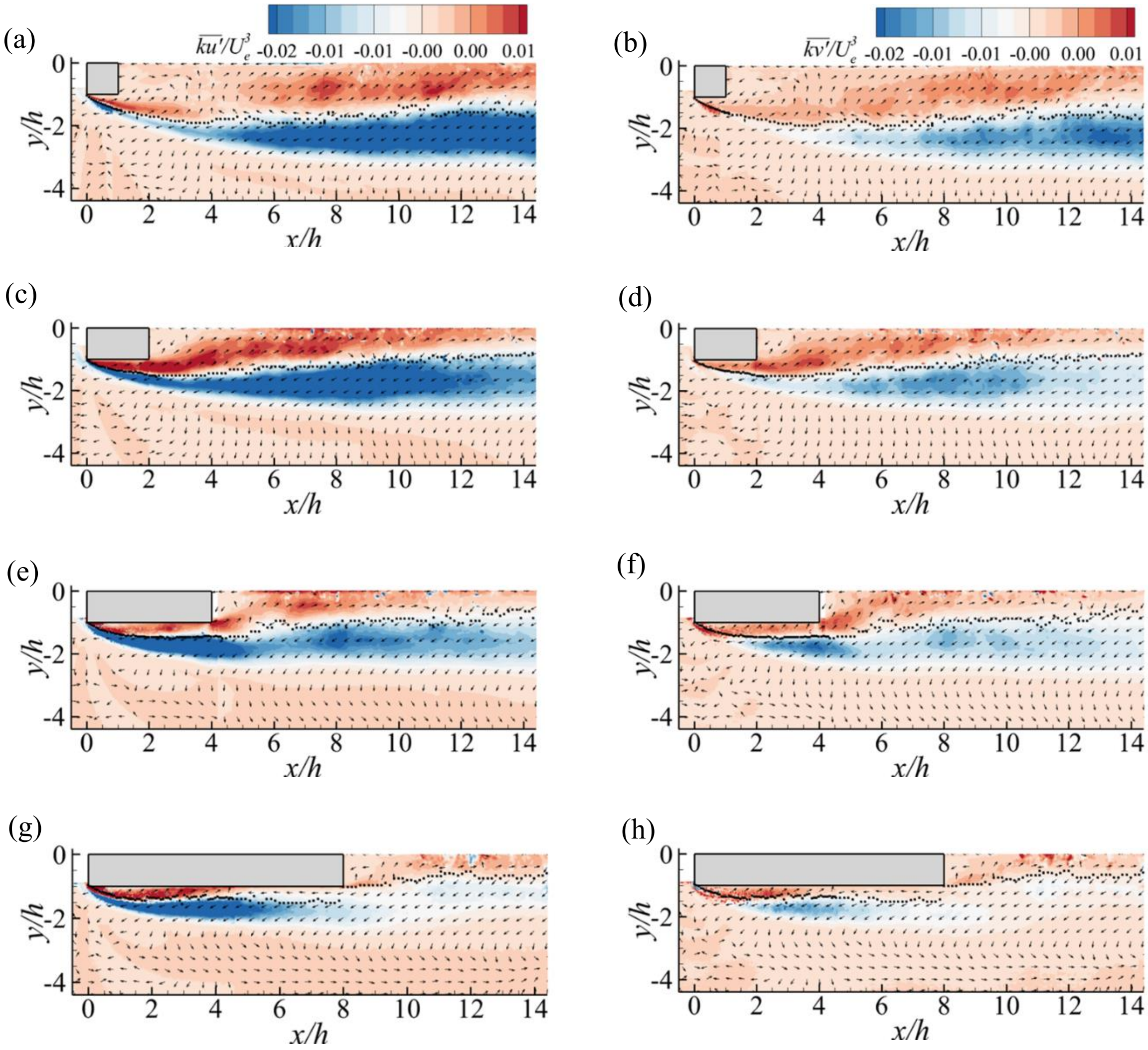

Figure 4.12 Contours of turbulence transport of TKE by velocity fluctuations u' (left) and v' (right) superimposed with the center of the mean shear layer (black dotted line) for (a, b) AR1, (c, d) AR2, (e, f) AR4, and (g, h) AR8.

4.6 Frequency Spectra and Proper Orthogonal Decomposition (POD)

4.6.1 Frequency Spectra

Frequency spectra of the streamwise velocity fluctuations at the maximum $\overline{u'u'}$ locations on the cylinder and in the wake are used to examine the vortex shedding behavior of the flow in Figure

4.13 and Figure A.13. As shown in Figure 4.13(a), the dominant frequencies in the separated shear layer on top of the cylinders with mean reattachment (AR4 and AR8) are similar, *St* ∈ [0.089, 0.097]. Similar dominant frequencies are also noted for AR1 and AR2. For the reattached cases (AR4 and AR8) the dominant frequencies in the wake coincide with those observed in the separated shear layer on these cylinders. Additionally, the shedding frequency of the AR4 cylinder is lower compared to the uniform flow case (*St* = 0.134) (Kumahor and Tachie, 2023a). The shedding frequency for the reattached cylinders is similar to the larger dominant shedding frequency (*St* = 0.089) for an infinite rectangular cylinder (AR33.3) by Fang et al. (2022). In contrast, the shedding frequencies in the wake of the unattached cylinders (AR1 and AR2) are significantly reduced in comparison to those found in the upstream shear layer. The dominant frequencies for the AR1 cylinder in Figure 4.13(a, b) are quite different from *St* = 0.138 reported for a square cylinder in a uniform flow (Kumahor and Tachie, 2022, 2023a). In Figure 4.13(b), the AR2 cylinder also reveal multiple frequencies including the shedding frequency, *St* = 0.097 in the reattached regime, which is less energetic compared to the other dominant frequencies (*St* = 0.032, 0.057, 0.154). This is reminiscent of the occurrence of intermittent reattachment of the shear layer onto the cylinder, and in qualitative agreement with the dual shedding mode *St* = 0.084 and *St* = 0.154 reported by Kumahor and Tachie (2023a), Okajima (1982) and Knisely (1990) on the AR2 cylinder in a uniform flow. The *St* = 0.154 for the AR2 cylinder at the free surface is in good agreement with *St* = 0.142 – 0.154 reported in a uniform flow (Okajima, 1982; Knisely, 1990; Kumahor and Tachie, 2023a).

4.6.2 Proper Orthogonal Decomposition

Proper orthogonal decomposition (POD) introduced by Lumley (1967) is employed to explore how aspect ratio influences the coherent structures and vortex shedding phenomenon. In this study,

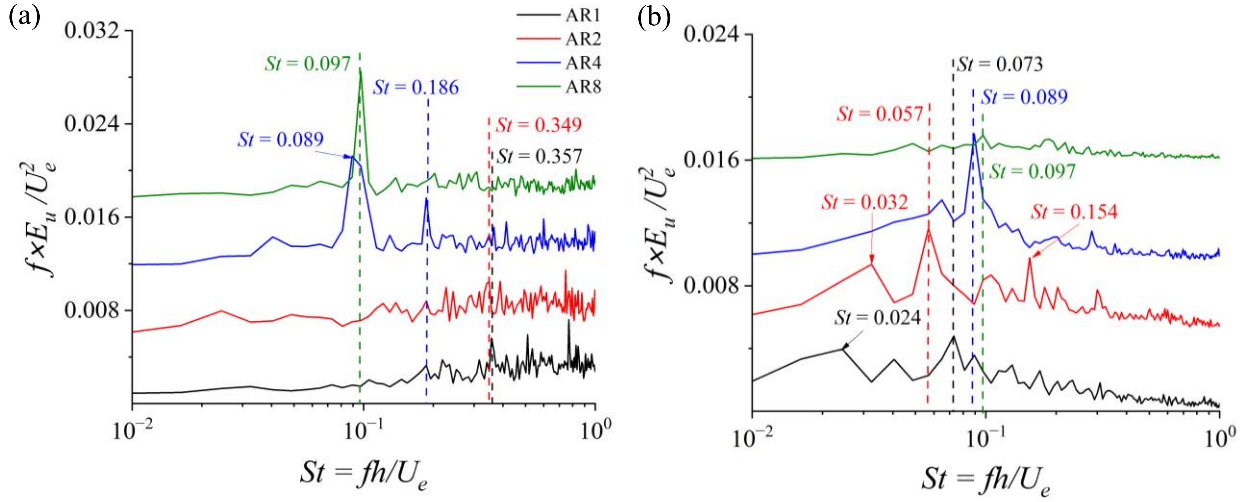

Figure 4.13 Pre-multiplied energy spectra of u' at maximum $\overline{u'u'}$ (a) on top of the cylinder and (b) in the wake for AR1, AR2, AR4, and AR8.

the snapshot method proposed by Sirovich (2016) was employed. The velocity vector field $u_i'(x, y, t)$ is expressed as a combination of deterministic spatial functions $\Phi_i^k(x, y)$ influenced by random time coefficients $a^k(t)$ given as:

$$u_i'(x, y, t) = \sum_{k=1}^{\infty} a^k(t) \Phi_i^k(x, y)$$

where the $\Phi_i^k(x, y)$ represents the spatial modes and the $a^k(t)$ are their time coefficients. POD analysis of the flow field spanning *x/h* ∈ [-0.05, 14.40] and *y/h* ∈ [0.05, -4.40] was conducted, while blanking the location of the cylinder in the fields of view.

Figure 4.14 and Figure A.17 presents the relative contribution of the streamwise and vertical velocity fluctuations to the total turbulent kinetic energy by the first four most dominant modes containing about 27±2% of the total energy. Unlike in uniform flow cases (Riches et al., 2018; Abdul-Salam et al., 2023; Kumahor and Tachie, 2023a), the energy contribution of u' dominates regardless of aspect ratio. The combined contribution of both velocity fluctuations from the first two modes for AR1, AR2, AR4 and AR8 are 19.4%, 17.1%, 15%, and 16% respectively. This is about 2 to 3 times less than the energy content observed in the first two modes of cylinders in a uniform flow at similar aspect ratios by Kumahor and Tachie (2023a) (AR1: 66.3%, AR2: 54.2%, and AR4: 54.7%). For the first four modes, the energy contributions are 28.2%, 26.7%, 26.8%, and 25.6%, respectively, for AR1, AR2, AR4 and AR8. These energy contents identified here are also lower than those associated with the first two modes in the uniform flow (Kumahor and Tachie, 2023a), suggesting that the majority of the energy content in the flow is not predominantly concentrated within the first four modes, owing to the weak large-scale vortex shedding around the cylinders. This could also be attributed to the shedding from the top and bottom leading edges of the cylinder in a uniform flow (Kumahor and Tachie, 2023a). The energy content by the first two POD modes of the present AR1, AR4, and AR8 is 13%, 7%, and 47%, respectively, larger than corresponding values for the wall-mounted cylinders by van der Kindere and Ganapathisubramani (2018). To investigate the effects of aspect ratio on the spatial dynamics of the coherent structures, contours of the first four POD modes of AR1 and AR2 are presented in Figure 4.15, and that for AR4 and AR8 in Figure 4.16. Massive regions of the spatial modes of the flow are displayed in the energetic (low order) modes, indicating that the strongest coherent structures are represented by the large-scale structures. These peak regions occur along the shear layer similar to the observation in the wall-mounted cylinders (van der Kindere and Ganapathisubramani, 2018). For AR1, the first POD mode exhibits unidirectional streamwise flow pattern with the largest region. The AR2 shows two opposing pulses (positive and negative) downstream the cylinder which are closer to the cylinder than that of AR1. As aspect ratio increases, the massive regions in the first mode are drawn close to the cylinder and these large-

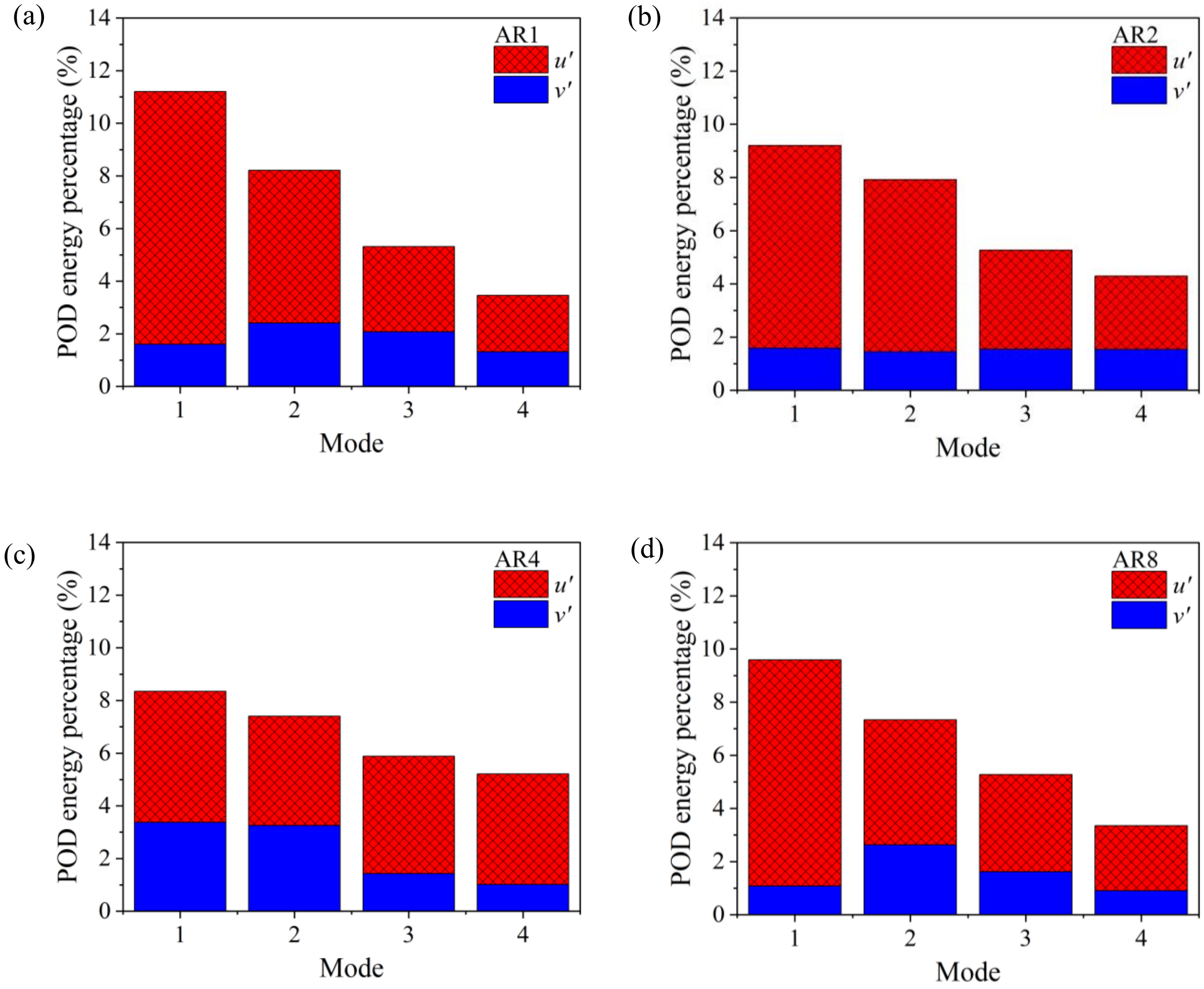

Figure 4.14 Relative contribution of streamwise and vertical velocity fluctuations to the total turbulent kinetic energy for the first four modes of (a) AR1, (b) AR2, (c) AR4, and (d) AR8.

scale structures interact with the cylinder in the reattached regime (Figure 4.16). The first two modes of AR4 display well-organized coherent structures which are transported downstream in a linear-like path. The structures in the longer cylinders (AR ≥ 3) elongate in the streamwise direction after reattachment as they are shed into the wake from the trailing edge. Compared to the shorter cylinders (Figure 4.15), the longer cylinders (Figure 4.16) reveal structures closer to the cylinder surface and do not grow vertically as much. With the exception of AR4 modes 3 and 4,

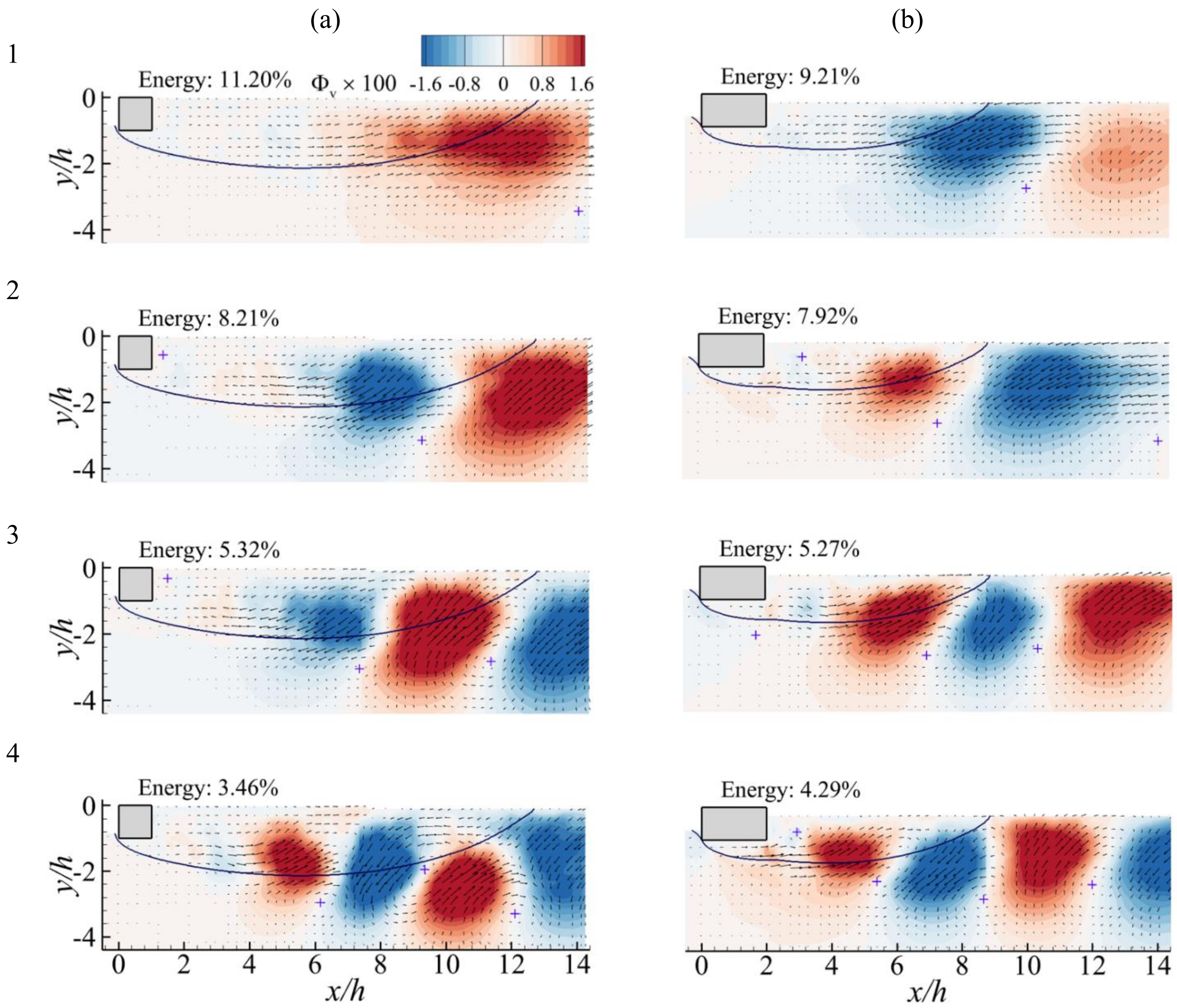

Figure 4.15 Contours of the first four spatial POD modes of the vertical velocity fluctuations superimposed with mean velocity streamline for (a) AR1, and (b) AR2. The (+) symbols mark the centres of the vortices in each mode.

which show larger-scale patches but have less energy than modes 1 and 2, this is consistent in all the cylinders with the observation by van der Kindere and Ganapathisubramani (2018) for cylinders mounted on a wall. It is interesting to note that the regions of the alternating peaks of the structures are closer to the shorter cylinders at higher modes. This suggests that the small-scale structures (higher mode numbers) tend to interact with the shorter cylinders than the large-scale

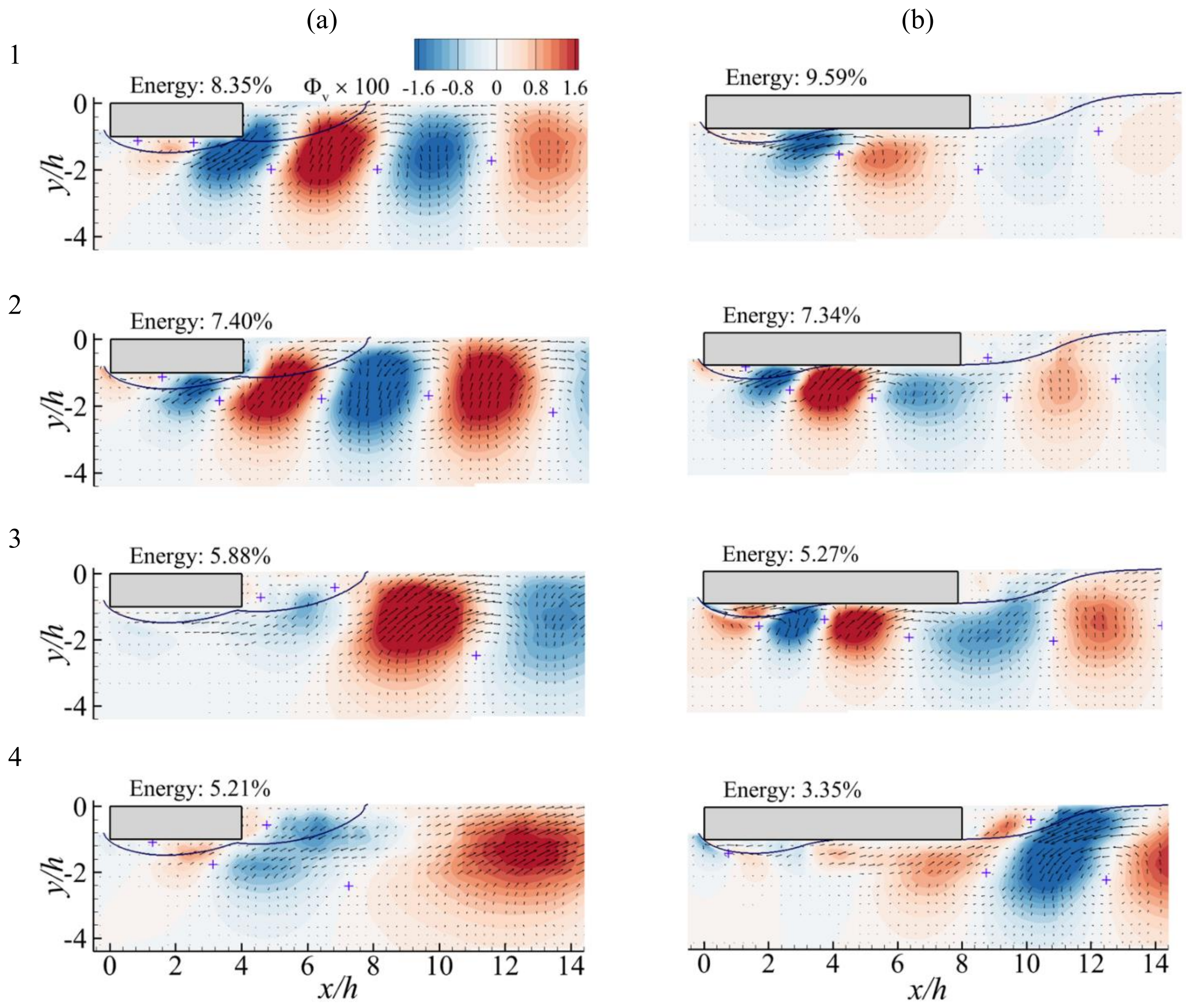

Figure 4.16 Contours of the first four spatial POD modes of the vertical velocity fluctuations superimposed with mean velocity streamline for (a) AR4, and (b) AR8. The (+) symbols mark the centres of the vortices in each mode.

structures. According to Figure 4.15 and Figure 4.16, the centres of the vortices downstream the cylinders appear closer to the free surface as aspect ratio increases. This implies that, the size of the large-scale vortices convected downstream are smaller in size at higher aspect ratios. The estimated wavelengths, λ/h, of the structures which defined as the distance between adjacent structures with like signs (Riches et al., 2018; Abdul-Salam et al., 2023; Kumahor and Tachie, 2023a), are λ/h = 8.78, 8.26, 6.4, and 6.52 for AR1 (mode 2), AR2 (mode 1), AR4 (mode 1), and

AR8 (mode 1) respectively. The convective velocity of the large-scale structures have been estimated in previous studies in a uniform flow (Riches et al., 2018; Abdul-Salam et al., 2023; Kumahor and Tachie, 2023a) as $U_c/U_e = St \times \lambda/h$. The estimated convective velocities associated with the large-scale structures in the present study are U_c/U_e = 0.21, 0.26, 0.57, and 0.63 for AR1, AR2, AR4, and AR8 respectively. This reveals that the convective velocity increases with increasing aspect ratio. However, these values are significantly lower than convective velocities (U_c/U_e = 0.81 ± 0.06) for cylinders in the uniform flow (Nakagawa et al., 1999; Abdul-Salam et al., 2023; Kumahor and Tachie, 2023a).

Figure 4.17 and Figure A.20 present the time signal of the mode coefficients ($a^{(i)}$, where i is the mode number), phase portraits, and the radius ($\sqrt{(a^{(1)})^2 + (a^{(2)})^2}$) of the first two POD modes, which are employed to examine the temporal characteristics of the first two POD modes. The time signals of the first two modes exhibit random patterns with no distinct phase shift between the two modes. However, AR4 and AR8 reveal a quasi-periodic sinusoidal pattern. The phase portrait of the first two modes of the AR4 cylinder produces a more closely defined circular pattern than the other cylinders, although not comparable to that of the uniform flow case. The radius of the first two modes reveals no regular and distinct pattern for all the cases and significantly varies in each cycle, but a mean radius of 0.886 ± 0.027. Kumahor and Tachie (2023a) also observed distinct circular phase portraits for AR1 and AR4, and attributed it to the regular vortex shedding around the cylinders. The results in this study indicate that the shedding pattern around the free surface-mounted rectangular cylinders exhibits irregularities, irrespective of aspect ratio. This irregular shedding pattern is influenced by the dynamic interactions between the cylinder, the free surface, and the surrounding flow conditions.

Figure 4.18 shows the pre-multiplied energy spectra of the first two POD mode coefficients,

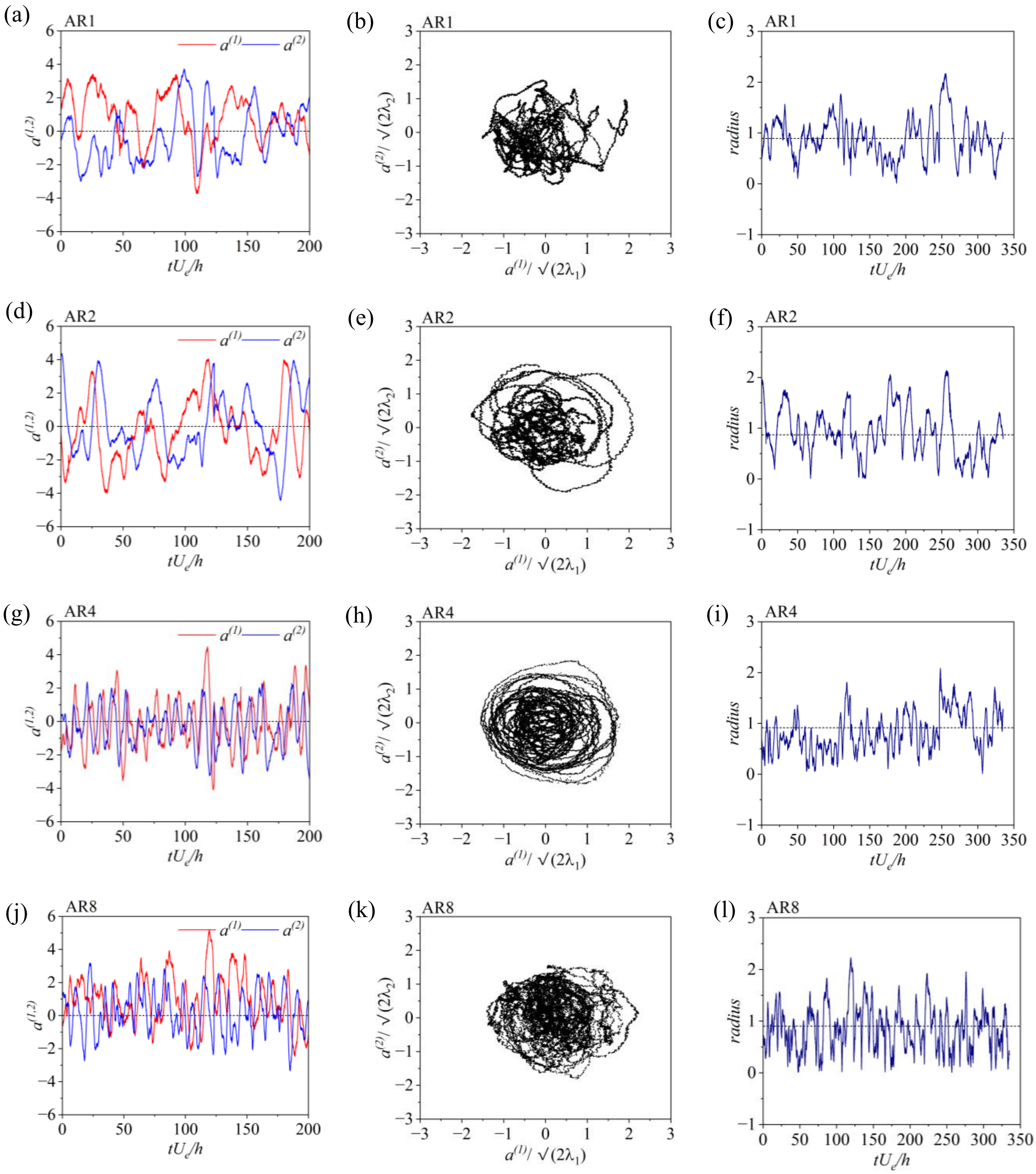

Figure 4.17 Time signal of the mode coefficients (left), phase portraits (middle) and radius (right) of the first two modes of (a – c) AR1, (d – f) AR2, (g – i) AR4, and (j – l) AR8.

providing insights into the unsteady characteristics of the coherent structures for AR1, AR2, AR4,

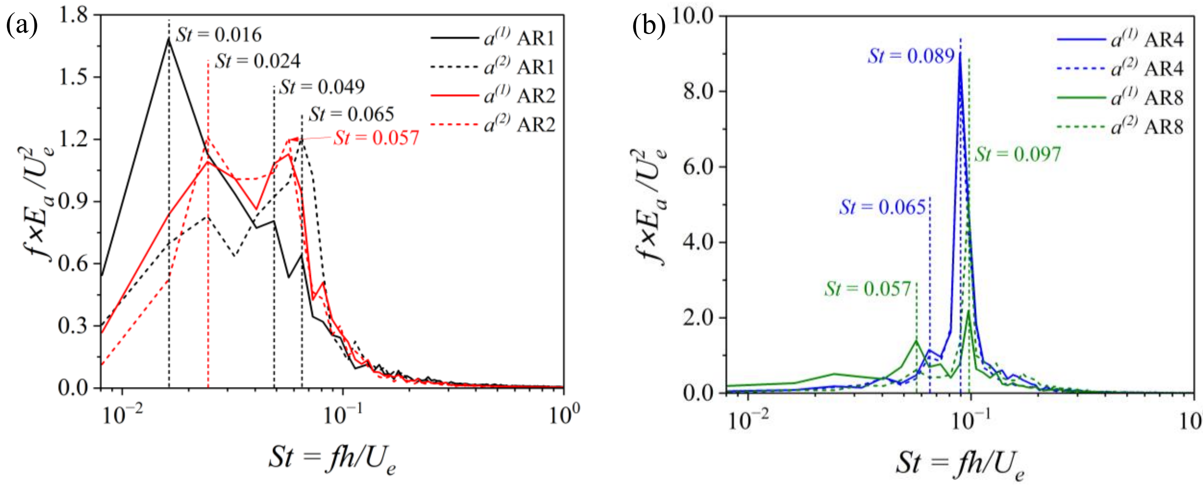

Figure 4.18 Pre-multiplied energy spectra of first two POD mode coefficients of (a) AR1 and AR2, and (b) AR4 and AR8.

and AR8. Comparing the energy spectra between unattached, i.e., AR1 and AR2 (Figure 4.18(a)) and attached, AR4 and AR8 (Figure 4.18(b)) cylinders reveal notable differences in dominant frequencies and energy levels. In Figure 4.18(a), the dominant shedding frequencies for AR1 and AR2 are lower than that of the velocity fluctuations (Figure 4.13). However, Figure 4.18(b) shows that the first two POD mode coefficients of AR4 and AR8 exhibit the same dominant frequencies as the corresponding velocity fluctuations (Figure 4.13). Furthermore, the dominant frequencies in AR1 and AR2 are significantly lower than that of AR4 and AR8. It is noted that the AR2 cylinder reveal two co-dominant frequencies *St* = 0.024 and 0.057, indicative of intermittent attachment onto the cylinder. The dominant frequency *St* = 0.024 in the AR2 is comparable to the dominant frequency (*St* = 0.03) for a wall-mounted AR2 cylinder by Chalmers et al. (2021).

5 Conclusions and Recommendations

This chapter presents the major findings of the present study as well as recommendations for future work.

5.1 Summary and Conclusions

Time-resolved PIV system was used to investigate the effects of streamwise aspect ratio (AR) on flow characteristics on free surface-mounted rectangular cylinders. In this study, seven different rectangular cylinders of aspect ratios, AR1, AR2, AR2.5, AR3, AR4, AR5, and AR8 were tested at a fixed Reynolds number of 11100, blockage ratio (BR = 7.0%), and freestream turbulence intensity (Tu ≈ 0.87%).

The results show that the separated shear layer is shed directly into the wake for AR1, intermittently reattaches on AR2 and AR2.5 but fully reattaches onto the cylinder with subsequent separation from the trailing edge and reattachment onto the free surface for AR ≥ 3. As a result, a large recirculation bubble is formed in the wake for AR1 but the size of this bubble decreases to an identical size for AR ≥ 4. The reattachment mechanism on the cylinder is similar to cylinders in a uniform flow, but the subsequent reattachment on the free surface is similar to a wall-mounted cylinder with low approach TBL thickness. The Reynolds stresses show significant aspect ratio dependency and are strongly influenced by the size of the recirculation regions formed on top of the cylinders and in the wake region. Based on the orientation of the mean shear, the production of Reynolds shear stress is induced by Q1 and Q3 events, but the contribution by the Q3 event is the greatest for AR > 2 due to the intermittent and permanent reattachment of the separated shear layer on the cylinder as aspect ratio increases. The maximum turbulence production is independent of aspect ratio, and the contributions by the individual components of the production term demonstrate no significant effect of aspect ratio for AR ≥ 2 at the maximum production location. However, the profiles of the production term at the TKE peak locations show strong dependence on aspect ratio. Greater levels of elevated regions of transport of TKE occur in the wake of the unattached cylinders and are drawn to the top of the cylinder as aspect ratio increases. Frequency spectra analysis showed that the dominant frequencies on the cylinder and in the wake decrease as aspect ratio increases for AR < 4. Similar frequencies were observed for the reattached cylinders (AR3 – AR8) and either of these frequencies emanated and co-dominated in the intermediate cases (AR2 – AR2.5) signifying dual mode shedding which is attributed to the intermittent reattachment of the separated shear layer onto the cylinder. Proper orthogonal decomposition analyses show that the u' dominates the contribution to production of turbulent kinetic energy. Massive regions of the coherent structures formed on, and in the wake, of the cylinders reveal strong dependence on aspect ratio. The time signal, phase portraits and radius reveal that the coherent structures are well organized in the AR4 cylinder than the other cylinders and not comparable to the behavior portrayed by AR4 cylinder in a uniform flow.

5.2 Recommendations for Future Work

Building on the scope and findings from the present study, the following recommendations are made for future work.

1. In this study, a planar PIV system was employed to measure the streamwise and vertical velocity components. The spanwise velocity component was not measured resulting in the unavailability of some of the Reynolds stress components. Consequently, the precise turbulent kinetic energy and production term could not be calculated. It is recommended that more advanced PIV systems such as stereo (2D3C) PIV or tomographic (3D3C) PIV,

which measure all three velocity components, be employed in future work to achieve a more comprehensive understanding of the flow behavior.

2. The effects of aspect ratio were analyzed at a fixed Reynolds number in the present study. Therefore, it is recommended to investigate the effects of Reynolds number for rectangular cylinders mounted at the free surface to provide more insight into the dynamics of the flow at the free surface.
3. It is recommended to study the effects of submergence ratio for fully submerged rectangular cylinders of different aspect ratios and Reynolds numbers. This will help to improve the understanding of the influence of the free surface on flow separation and reattachment around cylinders near a free surface.

References

Abdul-Salam, F. B., Fang, X., and Tachie, M. F. (2023). Blockage ratio and Reynolds number effects on flows around a rectangular prism. *Physics of Fluids*, *35*(9), 95137. https://doi.org/10.1063/5.0165627

Addai, S., Fang, X., Mante, A. A., and Tachie, M. F. (2022). The Wake Dynamics Behind a Near-Wall Square Cylinder. *Journal of Fluids Engineering, Transactions of the ASME*, *144*(5), 1–19. https://doi.org/10.1115/1.4052675

Addai, S., Tachie, M. F., Dow, K., Clark, S. P., and Israel, M. K. (2024). Separated flow around half-submerged horizontal circular cylinders at different Reynolds numbers. *Experiments in Fluids*, *65*(1), 1–22. https://doi.org/10.1007/s00348-023-03745-1

Arie, M., Kiya, M., Tamura, H., and Kanayama, Y. (1975). Flow over Rectangular Cylinders Immersed in a Turbulent Boundary Layer : Part 1, Correlation between Pressure Drag and Boundary-Layer Characteristics. *Bulletin of JSME*, *18*(125), 1260–1268. https://doi.org/10.1299/jsme1958.18.1260

Arslan, T., Malavasi, S., Pettersen, B., and Andersson, H. I. (2013). Turbulent flow around a semi-submerged rectangular cylinder. *Journal of Offshore Mechanics and Arctic Engineering*, *135*(4), 1–11. https://doi.org/10.1115/1.4025144

Bearman, P. W. (1969). On vortex shedding from a circular cylinder in the critical Reynolds number rágime. *Journal of Fluid Mechanics*, *37*(3), 577–585. https://doi.org/10.1017/S0022112069000735

Bendat, J. S., and Piersol, A. G. (2011). Random Data: Analysis and Measurement Procedures. In *Random Data* (4. Aufl., Vol. 729). Wiley.

Bergeles, G., and Athanassiadis, N. (1983). The Flow Past a Surface-Mounted Obstacle. *Journal of Fluids Engineering*, *105*(4), 461–463. https://doi.org/10.1115/1.3241030

Cermak, J. E. (1976). Aerodynamics of Buildings. *Annual Review of Fluid Mechanics*, *8*((1976)), 75–106. https://doi.org/10.1146/annurev.fl.08.010176.000451

Chalmers, H., Fang, X., Addai, S., and Tachie, M. F. (2022). The effects of wall roughness on the flow dynamics behind a near-wall square cylinder. *Experiments in Fluids*, *63*(8), 1–20. https://doi.org/10.1007/s00348-022-03472-z

Chalmers, H., Fang, X., and Tachie, M. F. (2021). Streamwise Aspect Ratio Effects on Turbulent Flow Separations Induced by Forward-Backward-Facing Steps. *Journal of Fluids Engineering, Transactions of the ASME*, *143*(2). https://doi.org/10.1115/1.4048686

Chalmers, H., Fang, X., and Tachie, M. F. (2023). Gap ratio effects on the coherent structures surrounding a near-wall square cylinder. *International Journal of Heat and Fluid Flow*, *100*(January), 109114. https://doi.org/10.1016/j.ijheatfluidflow.2023.109114

Chun, K. B., and Sung, H. J. (1996). Control of turbulent separated flow over a backward-facing step by local forcing. *Experiments in Fluids*, *21*(6), 417–426. https://doi.org/10.1007/BF00189044

Cimarelli, A., Leonforte, A., and Angeli, D. (2018). Direct numerical simulation of the flow around a rectangular cylinder at a moderately high Reynolds number. *Journal of Wind Engineering and Industrial Aerodynamics*, *174*, 39–49. https://doi.org/https://doi.org/10.1016/j.jweia.2017.12.020

Durão, D. F. G., Heitor, M. V., and Pereira, J. C. F. (1988). Measurements of turbulent and periodic flows around a square cross-section cylinder. *Experiments in Fluids*, *6*(5), 298–304. https://doi.org/10.1007/BF00538820

Essel, E. E., Nematollahi, A., Thacher, E. W., and Tachie, M. F. (2015). Effects of Upstream Roughness and Reynolds number on Separated and Reattached Turbulent Flow. *Journal of Turbulence*, *16*(9), 872–899. https://doi.org/10.1080/14685248.2015.1033060

Essel, E. E., and Tachie, M. F. (2015). Roughness effects on turbulent flow downstream of a backward facing step. *Flow, Turbulence and Combustion*, *94*(1), 125–153. https://doi.org/10.1007/s10494-014-9549-1

Essel, E. E., and Tachie, M. F. (2017). Upstream roughness and Reynolds number effects on turbulent flow structure over forward facing step. *International Journal of Heat and Fluid Flow*, *66*, 226–242. https://doi.org/10.1016/j.ijheatfluidflow.2015.11.004

Fang, X., Dow, K., Tachie, M. F., Jarrod, M., and Wang, S. (2023). Flow Characteristics beneath Ice Blocks with Smooth and Rough Undersurfaces. *Journal of Hydraulic Engineering*, *149*(4). https://doi.org/10.1061/jhend8.hyeng-13207

Fang, X., and Tachie, M. F. (2019a). Flows over Surface-Mounted Bluff Bodies with different Spanwise Widths submerged in a deep Turbulent Boundary Layer. *Journal of Fluid Mechanics*, *877*, 717–758. https://doi.org/DOI: 10.1017/jfm.2019.617

Fang, X., and Tachie, M. F. (2019b). On the Unsteady Characteristics of Turbulent Separations over a Forward–Backward-Facing Step. *Journal of Fluid Mechanics*, *863*, 994–1030.

Fang, X., and Tachie, M. F. (2020). Spatio-Temporal dynamics of flow separation induced by a forward-facing step submerged in a thick turbulent boundary layer. *Journal of Fluid Mechanics*, *892*, 1–30. https://doi.org/10.1017/jfm.2020.209

Fang, X., Tachie, M. F., and Dow, K. (2022). Turbulent Separations beneath Semi-submerged Bluff Bodies with Smooth and Rough Undersurfaces. *Journal of Fluid Mechanics*, *947*, 1–34. https://doi.org/10.1017/jfm.2022.661

Franke, R., Rodi, W., and Schönung, B. (1990). Numerical calculation of laminar vortex-shedding flow past cylinders. *Journal of Wind Engineering and Industrial Aerodynamics*, *35*(C), 237–257. https://doi.org/10.1016/0167-6105(90)90219-3

Kang, J., and Tachie, M. F. (2023). Experimental Study of Turbulent Wake Flow Around Trapezoidal Cylinders With Varying Streamwise Aspect Ratios. *Journal of Fluids Engineering, Transactions of the ASME*, *145*(8), 1–15. https://doi.org/10.1115/1.4062086

Kiya, M., and Sasaki, K. (1983). Structure of a turbulent separation bubble. *Journal of Fluid Mechanics*, *137*, 83–113. https://doi.org/10.1017/S002211208300230X

Knisely, C. W. (1990). Strouhal numbers of rectangular cylinders at incidence: A review and new data. *Journal of Fluids and Structures*, *4*(4), 371–393. https://doi.org/https://doi.org/10.1016/0889-9746(90)90137-T

Kumahor, S., and Tachie, M. F. (2022). Turbulent Flow Around Rectangular Cylinders With Different Streamwise Aspect Ratios. *Journal of Fluids Engineering, Transactions of the ASME*, *144*(5), 1–20. https://doi.org/10.1115/1.4052633

Kumahor, S., and Tachie, M. F. (2023a). Effects of streamwise aspect ratio on the spatio-temporal characteristics of flow around rectangular cylinders. *International Journal of Heat and Fluid Flow*, *101*(December 2022), 109133. https://doi.org/10.1016/j.ijheatfluidflow.2023.109133

Kumahor, S., and Tachie, M. F. (2023b). Turbulent flow around a short rectangular cylinder in uniform flow at moderate Reynolds numbers. *Experimental Thermal and Fluid Science*, *147*(March), 110960. https://doi.org/10.1016/j.expthermflusci.2023.110960

Kuroda, M., Tamura, T., and Suzuki, M. (2007). Applicability of LES to the turbulent wake of a rectangular cylinder-Comparison with PIV data. *Journal of Wind Engineering and Industrial Aerodynamics*, *95*(9–11), 1242–1258. https://doi.org/10.1016/j.jweia.2007.02.004

Le, H., Moin, P., and Kim, J. (1997). Direct numerical simulation of turbulent flow over a backward-facing step. *Journal of Fluid Mechanics*, *330*(September 2000), 349–374. https://doi.org/10.1017/S0022112096003941

Lin, J. C., Towfighi, J., and Rockwell, D. (1995). Instantaneous structure of the near-wake of a circular cylinder: On the effect of reynolds number. In *Journal of Fluids and Structures* (Vol. 9, Issue 4, pp. 409–418). https://doi.org/10.1006/jfls.1995.1023

Liu, J., Hussain, S., Wang, J., Wang, L., Xie, G., and Sundén, B. (2018). Heat transfer enhancement and turbulent flow in a high aspect ratio channel (4:1) with ribs of various truncation types and arrangements. *International Journal of Thermal Sciences*, *123*, 99–116. https://doi.org/https://doi.org/10.1016/j.ijthermalsci.2017.09.013

Liu, M., Kumahor, S., and Tachie, M. F. (2024). Reynolds Number Effects on Turbulent Wakes Generated by Rectangular Cylinders With Streamwise Aspect Ratios Between 1 and 4. *Journal of Fluids Engineering*, *146*(2), 1–21. https://doi.org/10.1115/1.4063434

Lumley, J. L. (1967). Similarity and the turbulent energy spectrum. *Physics of Fluids*, *10*(4), 855–858. https://doi.org/10.1063/1.1762200

Mashhadi, A., Sohankar, A., and Alam, M. M. (2021). Flow over rectangular cylinder: Effects of cylinder aspect ratio and Reynolds number. *International Journal of Mechanical Sciences*, *195*(January), 106264. https://doi.org/10.1016/j.ijmecsci.2020.106264

Miau, J. J., Wang, J. T., Chou, J. H., and Wei, C. Y. (2003). Low-frequency fluctuations in the near-wake region of a trapezoidal cylinder with low aspect ratio. *Journal of Fluids and Structures*, *17*(5), 701–715. https://doi.org/10.1016/S0889-9746(03)00007-0

Moore, D. M., Letchford, C. W., and Amitay, M. (2019a). Energetic scales in a bluff body shear layer. *Journal of Fluid Mechanics*, *875*, 543–575. https://doi.org/10.1017/jfm.2019.480

Moore, D. M., Letchford, C. W., and Amitay, M. (2019b). Transitional Shear Layers on

Rectangular Sections. *Lecture Notes in Civil Engineering*, *27*(Roshko 1954), 519–533. https://doi.org/10.1007/978-3-030-12815-9_40

Nakagawa, S., Nitta, K., and Senda, M. (1999). An Experimental Study on Unsteady Turbulent Near Wake of a Rectangular Cylinder in Channel Flow. *Experiments in Fluids*, *27*(3), 284–294. https://doi.org/10.1007/s003480050353

Nematollahi, A., and Tachie, M. F. (2018). Time-resolved PIV measurement of influence of upstream roughness on separated and reattached turbulent flows over a forward-facing step. *AIP Advances*, *8*(10). https://doi.org/10.1063/1.5063455

Norberg, C. (1993). Flow around rectangular cylinders: Pressure forces and wake frequencies. *Journal of Wind Engineering and Industrial Aerodynamics*, *49*(1–3), 187–196. https://doi.org/10.1016/0167-6105(93)90014-F

Okajima, A. (1982). Strouhal numbers of rectangular cylinders. *Journal of Fluid Mechanics*, *123*, 379–398. https://doi.org/10.1017/S0022112082003115

Riches, G., Martinuzzi, R., and Morton, C. (2018). Proper orthogonal decomposition analysis of a circular cylinder undergoing vortex-induced vibrations. *Physics of Fluids*, *30*(10). https://doi.org/10.1063/1.5046090

Samimy, M., and Lele, S. K. (1991). Motion of particles with inertia in a compressible free shear layer. *Physics of Fluids A*, *3*(8), 1915–1923. https://doi.org/10.1063/1.857921

Sciacchitano, A., and Wieneke, B. (2016). PIV uncertainty propagation. *Measurement Science and Technology*, *27*(8), 84006-. https://doi.org/10.1088/0957-0233/27/8/084006

Sherry, M., Lo Jacono, D., and Sheridan, J. (2010). An Experimental Investigation of the Recirculation Zone formed Downstream of a Forward Facing Step. *Journal of Wind Engineering and Industrial Aerodynamics*, *98*(12), 888–894. https://doi.org/10.1016/j.jweia.2010.09.003

Shi, L. L., Liu, Y. Z., and Yu, J. (2010). PIV measurement of separated flow over a blunt plate with different chord-to-thickness ratios. *Journal of Fluids and Structures*, *26*(4), 644–657. https://doi.org/10.1016/j.jfluidstructs.2010.02.001

Sirovich, L. (2016). *Turbulence and the Dynamics OF Coherent Structures Part II : Symmetries and Transformations Source : Quarterly of Applied Mathematics , Vol . 45 , No . 3 (October 1987), pp . 573-582*. *45*(3), 573–582. http://www.jstor.org/stable/43637458

Trias, F. X., Gorobets, A., and Oliva, A. (2015). Turbulent flow around a square cylinder at Reynolds number 22,000: A DNS study. *Computers & Fluids*, *123*, 87–98. https://doi.org/https://doi.org/10.1016/j.compfluid.2015.09.013

van der Kindere, J., and Ganapathisubramani, B. (2018). Effect of length of two-dimensional obstacles on characteristics of separation and reattachment. *Journal of Wind Engineering and Industrial Aerodynamics*, *178*, 38–48. https://doi.org/10.1016/j.jweia.2018.04.018

Wu, Y., Ren, H., and Tang, H. (2013). Turbulent flow over a rough backward-facing step. *International Journal of Heat and Fluid Flow*, *44*, 155–169. https://doi.org/10.1016/j.ijheatfluidflow.2013.05.014

Zhang, L., Liu, X., and Jiang, Y. (2013). Application of entransy in the analysis of HVAC systems in buildings. *Energy*, *53*, 332–342. https://doi.org/10.1016/j.energy.2013.02.015

Zhang, X., Zeng, Q., and Liu, Z. (2019). Hydrodynamic performance of rectangular heaving buoys for an integrated floating breakwater. *Journal of Marine Science and Engineering*, *7*(8). https://doi.org/10.3390/jmse7080239

A. Appendix

Convergence Analysis of TRPIV Measurements

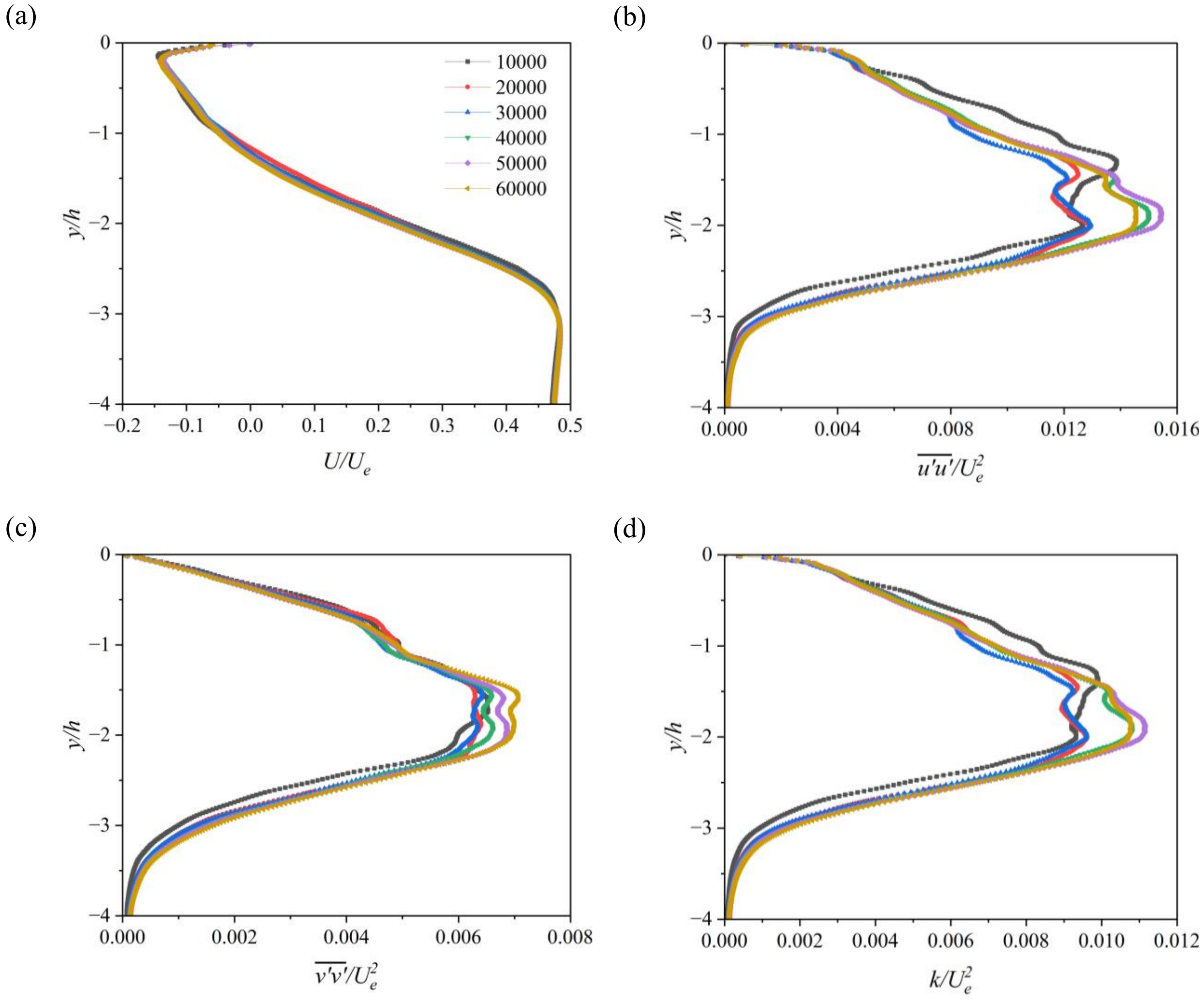

Figure A.1 Vertical profiles of (a) streamwise mean velocity, (b) streamwise Reynolds normal stress, (c) vertical Reynolds normal stress, and (d) turbulent kinetic energy at the midpoint of the recirculation region (*x/h* = 6.42) for AR1 at different samples sizes.

Additional Figures

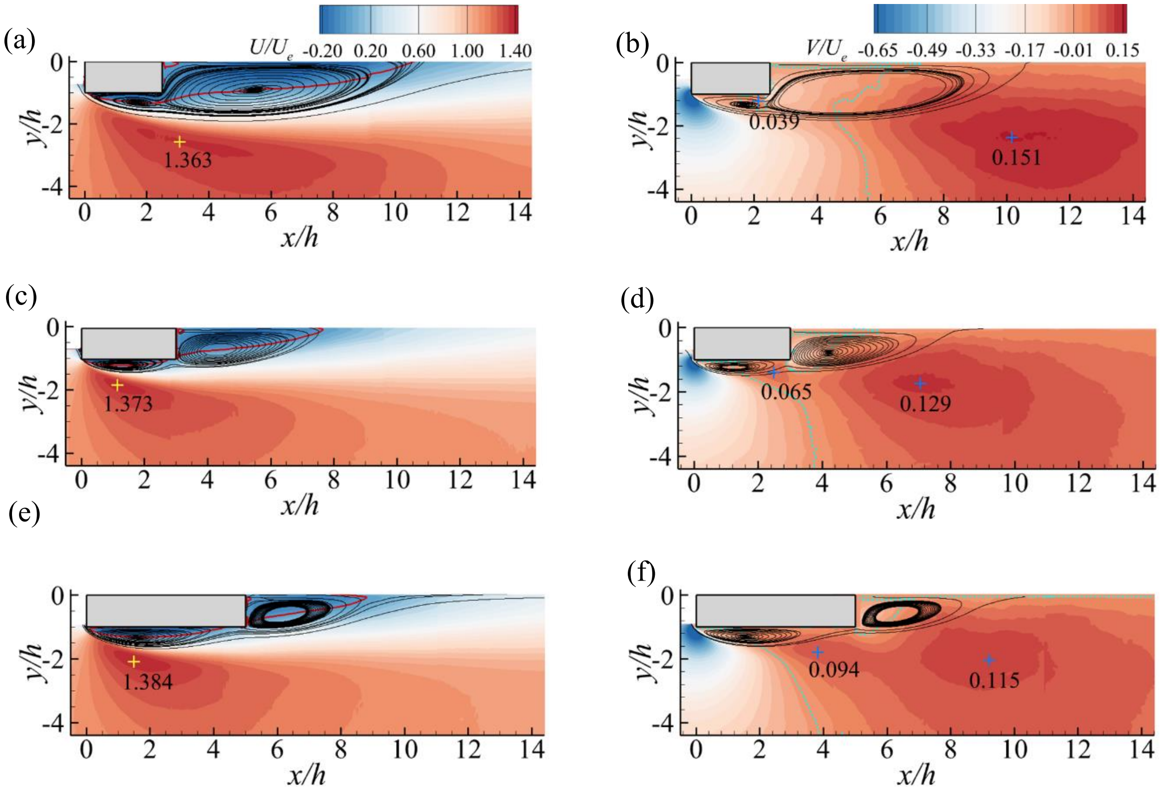

Figure A.2 Contours of streamwise mean velocity (left) with $U = 0$ (red solid line) isopleth and vertical mean velocity (right) with $V = 0$ isopleth (blue dashed line) and mean streamlines for (a, b) AR2.5, (c, d) AR3 and (e, f) AR5. The (+) symbol denotes the location of the peak streamwise mean velocity with the magnitude.

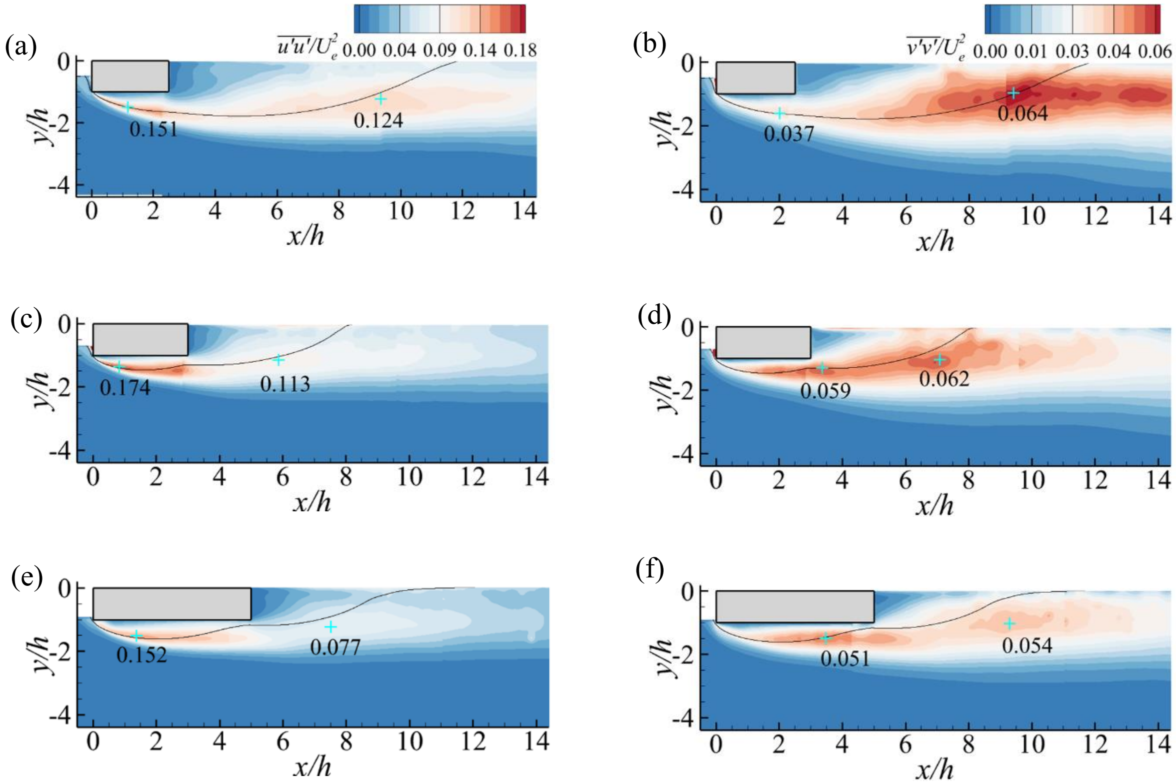

Figure A.3 Contours of streamwise Reynolds normal stress, $\overline{u'u'}$ (left) and vertical Reynolds normal stress, $\overline{v'v'}$ (right) and mean streamline for (a, b) AR2.5, (c, d) AR3, and (e, f) AR5.

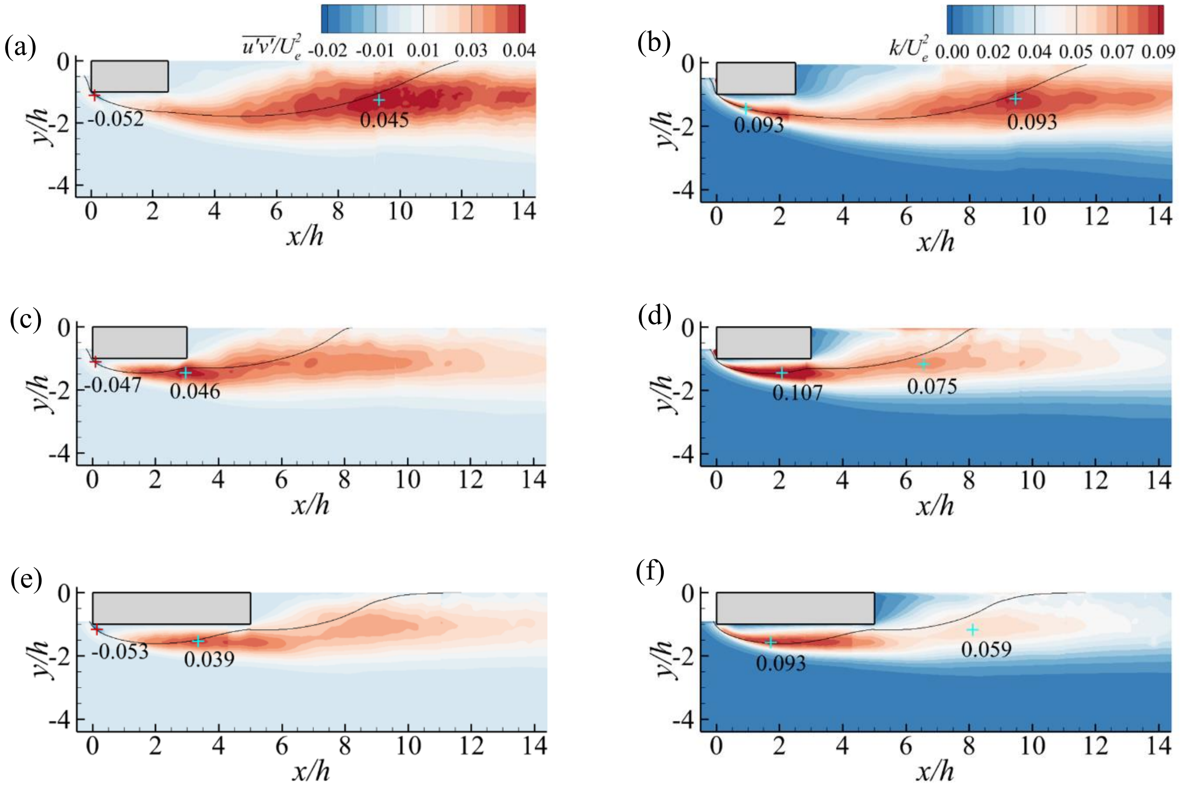

Figure A.4 Contours of Reynolds shear stress, $\overline{u'v'}$ (left) and turbulent kinetic energy, $k = 0.5(\overline{u'u'} + \overline{v'v'})$ (right) and mean streamline for (a, b) AR2.5, (c, d) AR3, and (e, f) AR5.

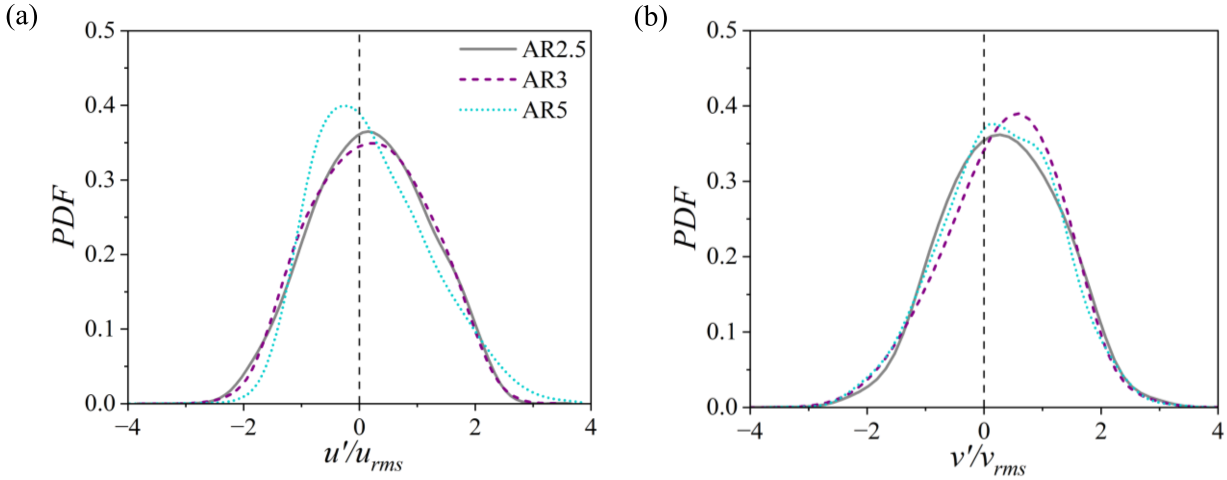

Figure A.5 Probability density functions of u' at maximum $\overline{u'u'}$ (a) on top of the cylinder and (b) maximum $\overline{v'v'}$ in the wake for AR2.5, AR3, and AR5.

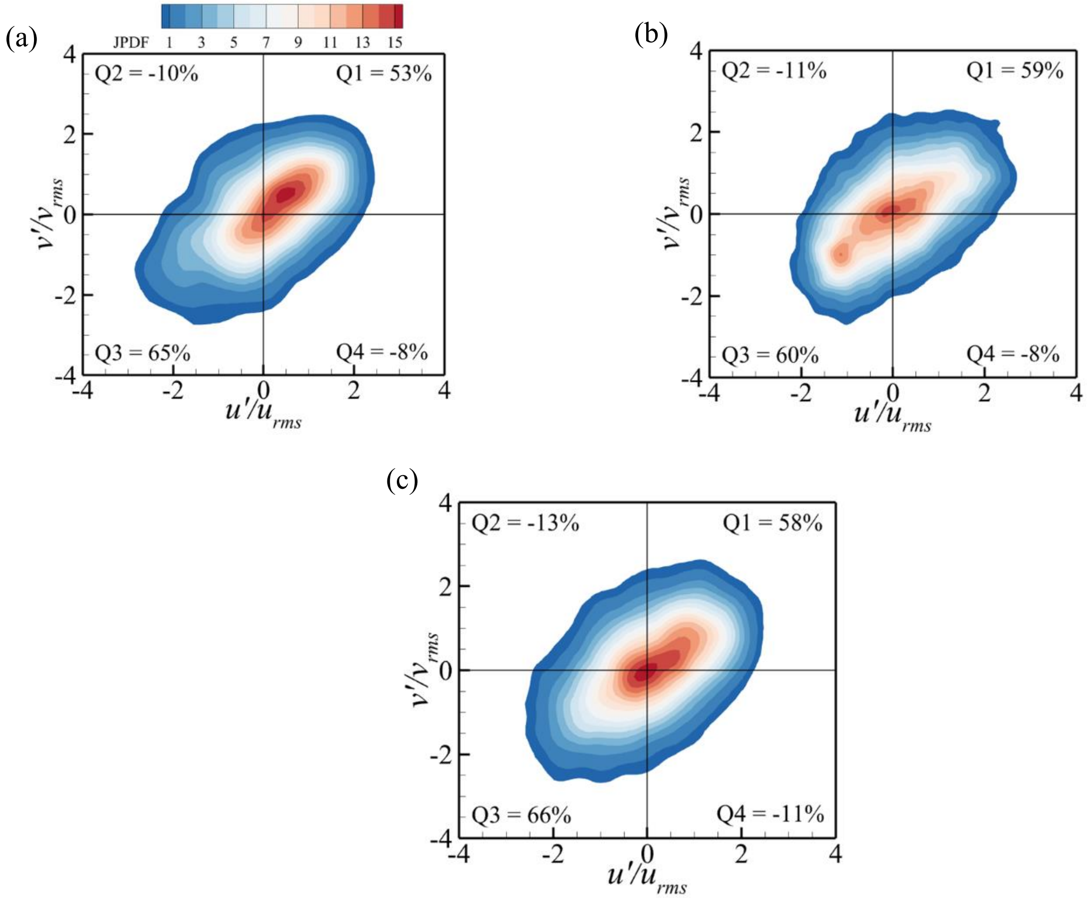

Figure A.6 Joint probability density function of velocity fluctuations at maximum $\overline{u'v'}$ for (a) AR2.5, (b) AR3, (c) AR5.

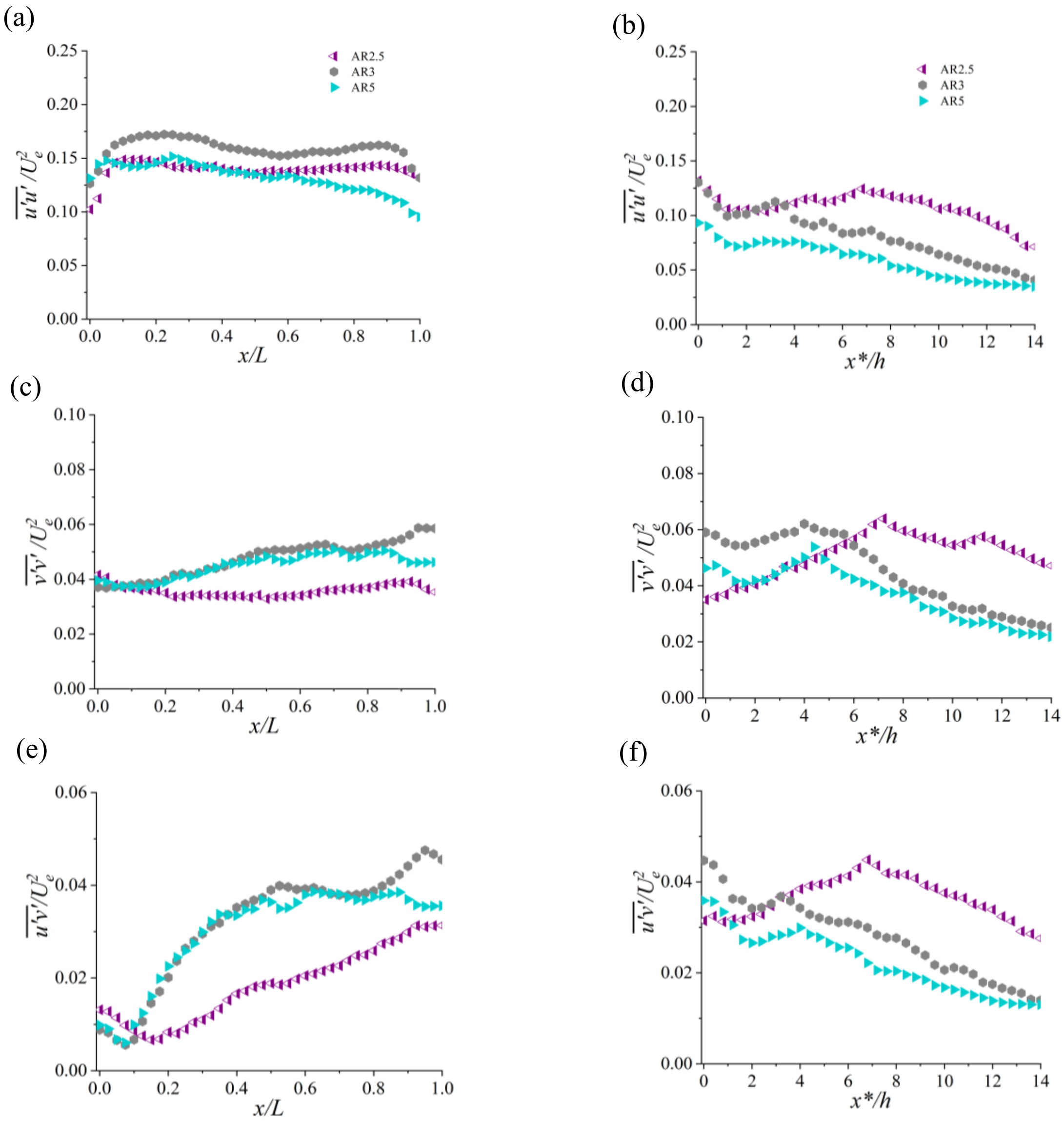

Figure A.7 Streamwise variation of maximum Reynolds stresses for AR2.5, AR3, and AR5. *x/L* – Streamwise length along the cylinder length, *x*/h* – Streamwise length from the trailing edge of the cylinder.

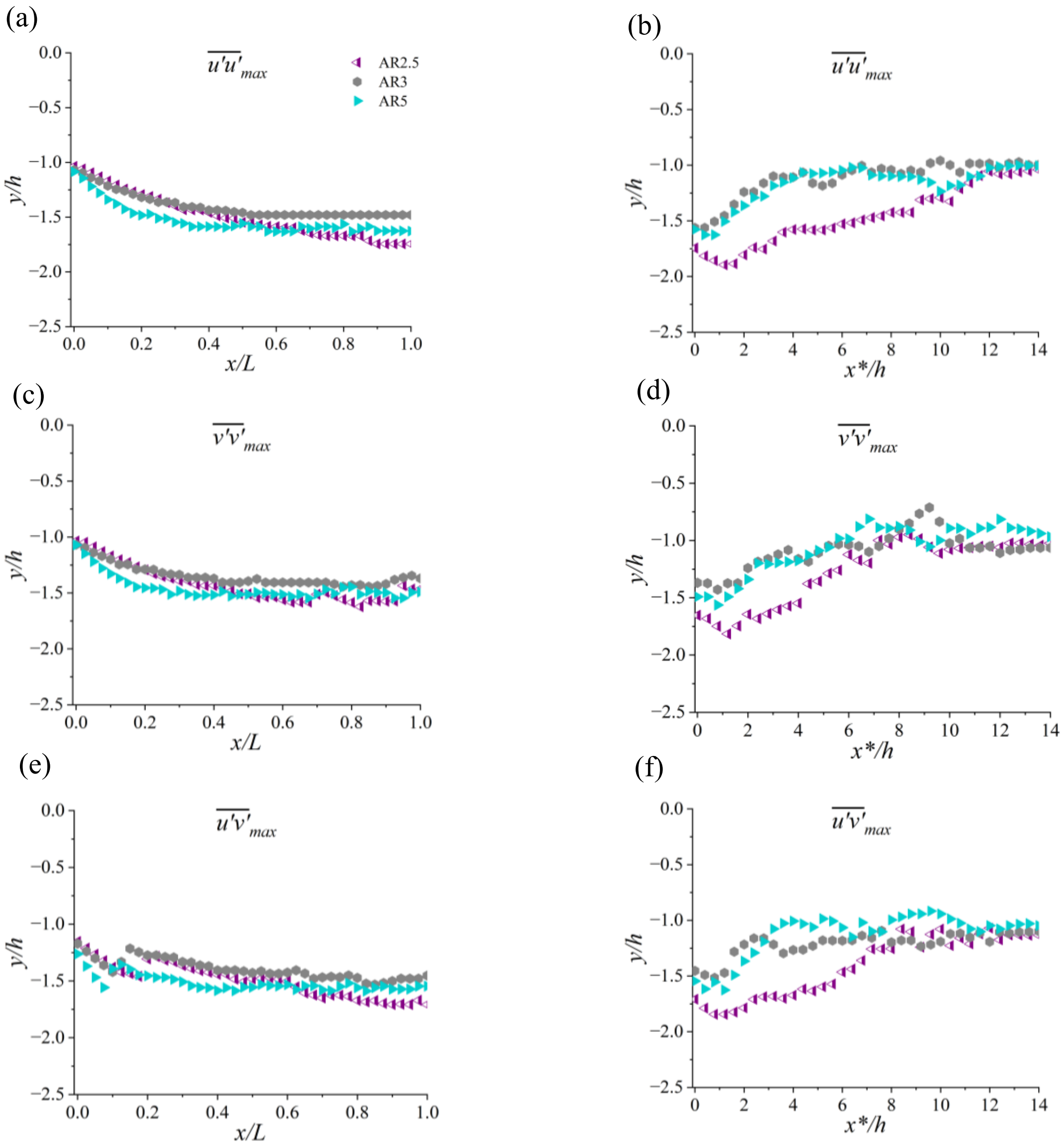

Figure A.8 Streamwise variation of vertical location of the maximum Reynolds stresses for AR2.5, AR3, and AR5. *x/L* – Streamwise length along the cylinder length, *x*/h* – Streamwise length from the trailing edge of the cylinder.

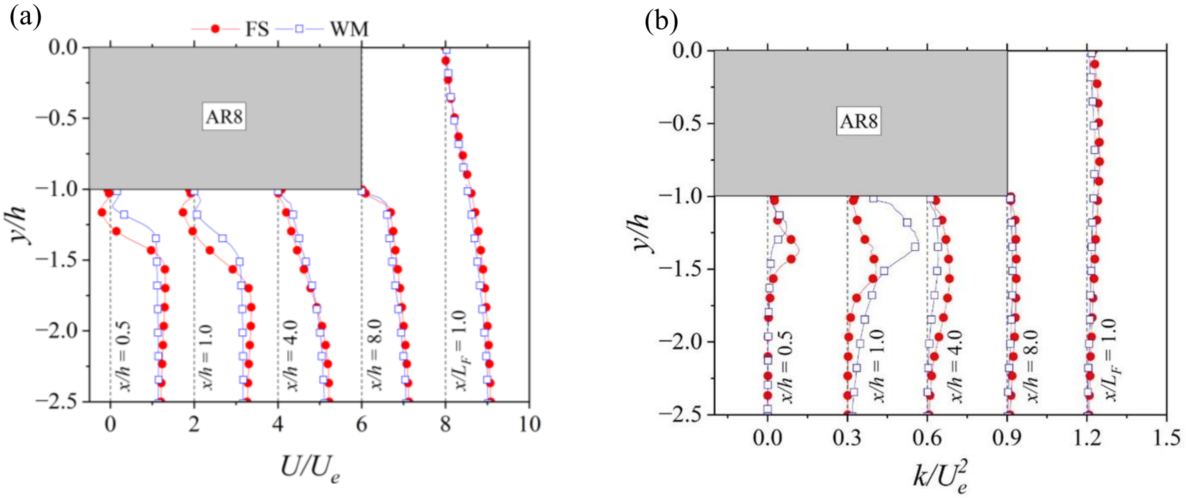

Figure A.9 Profiles of streamwise mean velocity (*U)* (left), and TKE (right) at selected streamwise locations for AR8, where $x/L_T = 1.0$ and $x^*/L_W = 1.0$ are the reattachment points on the cylinder and in the wake, respectively. FS (Free surface), and WM (Wall-mounted).

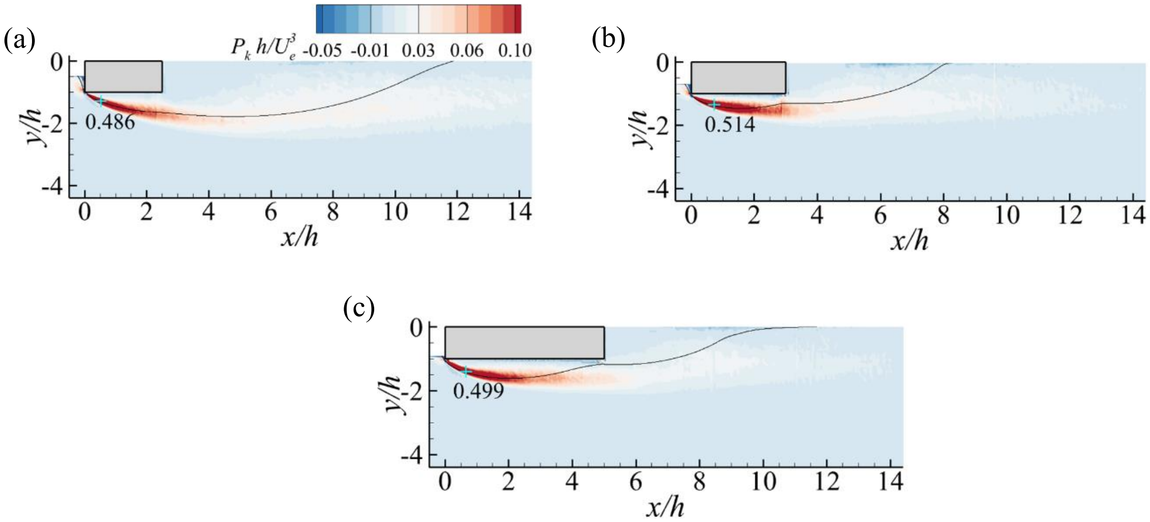

Figure A.10 Contours of production of turbulent kinetic energy, P_k, and mean streamline for (a) AR2.5, (b) AR3 and (c) AR5.

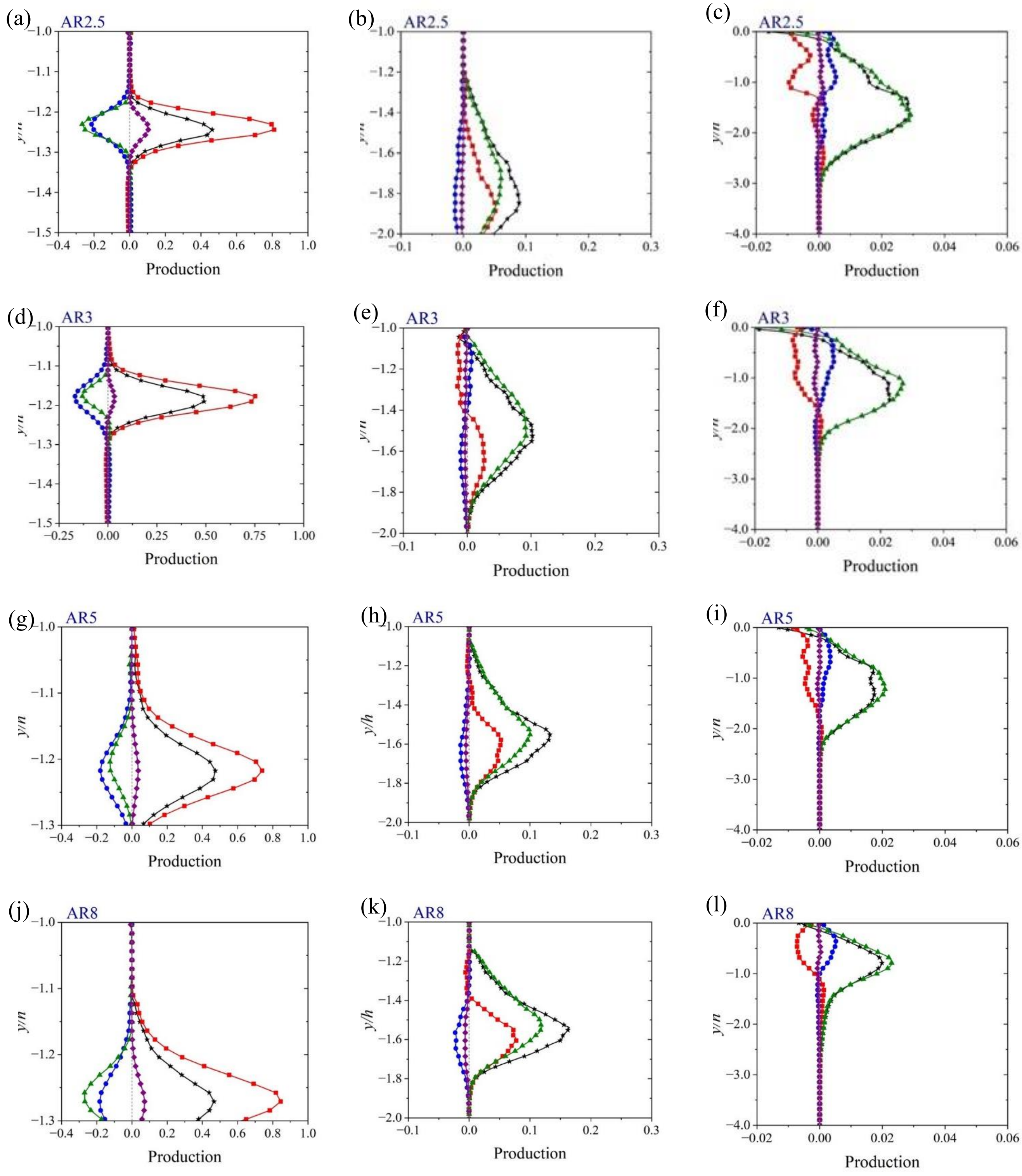

Figure A.11 Profiles of the individual production terms at (a, d, g, j) maximum P_k, maximum TKE (b, e, h, k) on top of the cylinder and (c, f, i, l) in the wake for AR2.5 (a - c), AR3 (d - f), AR5 (g – i), and AR8 (j - l).

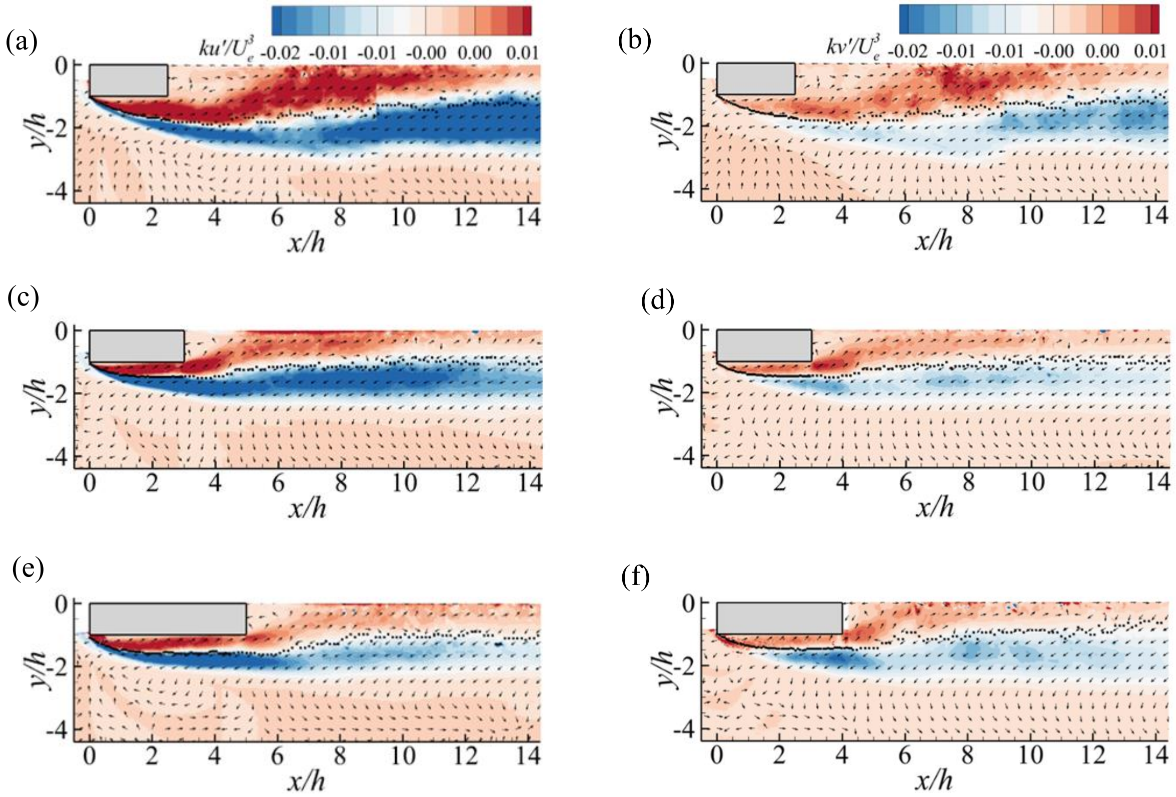

Figure A.12 Contours of turbulence transport of TKE by velocity fluctuations u' (left) and v' (right) for (a, b) AR2.5, (c, d) AR3, and (e, f) AR5.

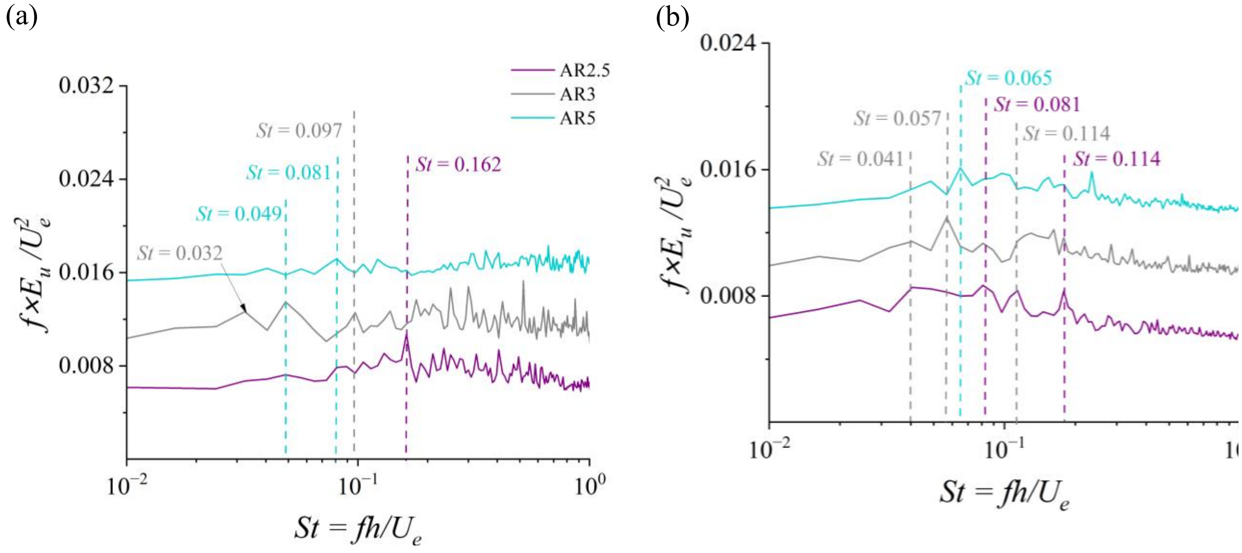

Figure A.13 Pre-multiplied energy spectra of u' at maximum $\overline{u'u'}$ (a) on top of the cylinder and (b) in the wake for AR2.5, AR3, and AR5.

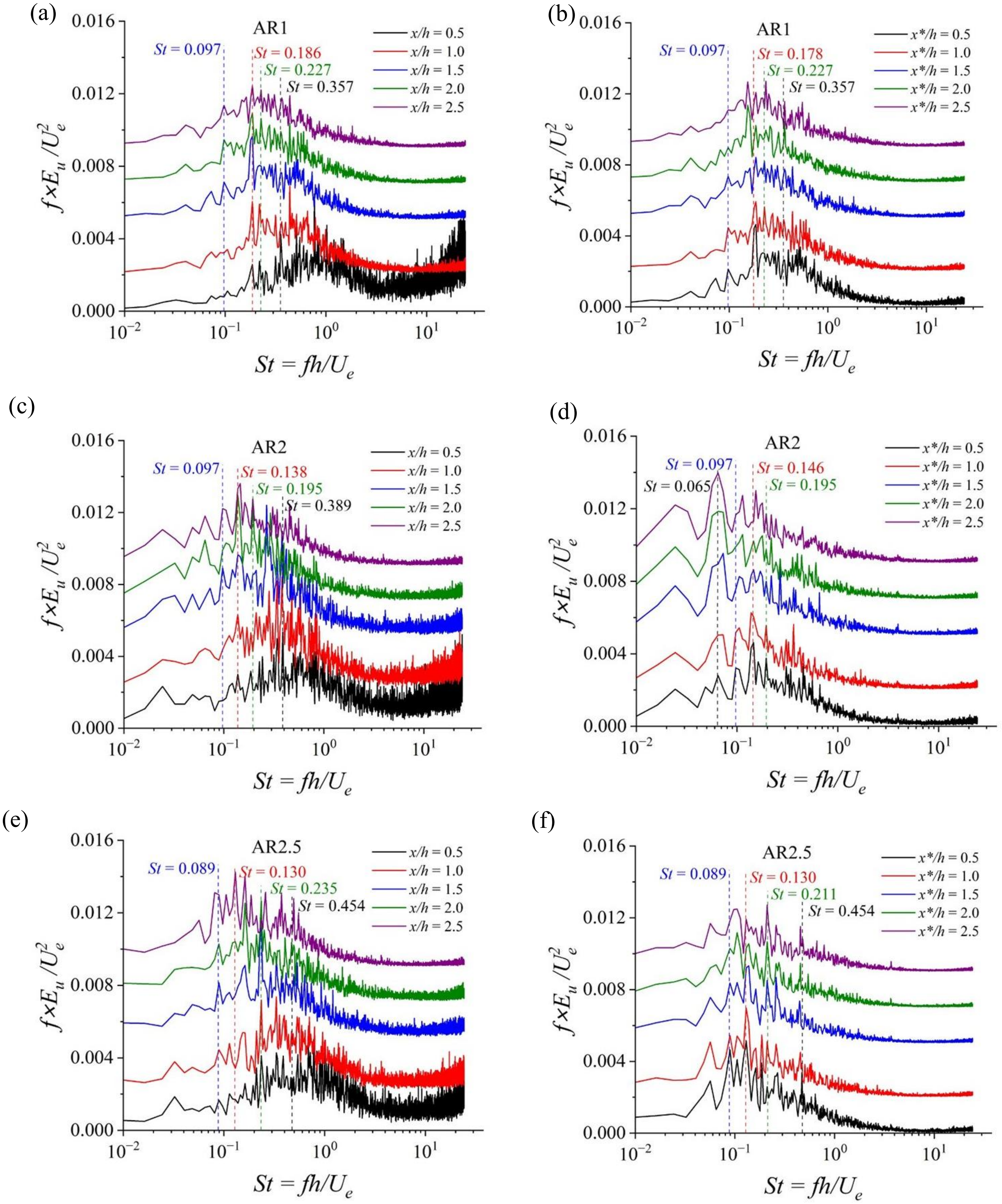

Figure A.14 Pre-multiplied energy spectra of u' along the mean streamline (a, b) AR1, (c, d) AR2, and (e, f) AR2.5.

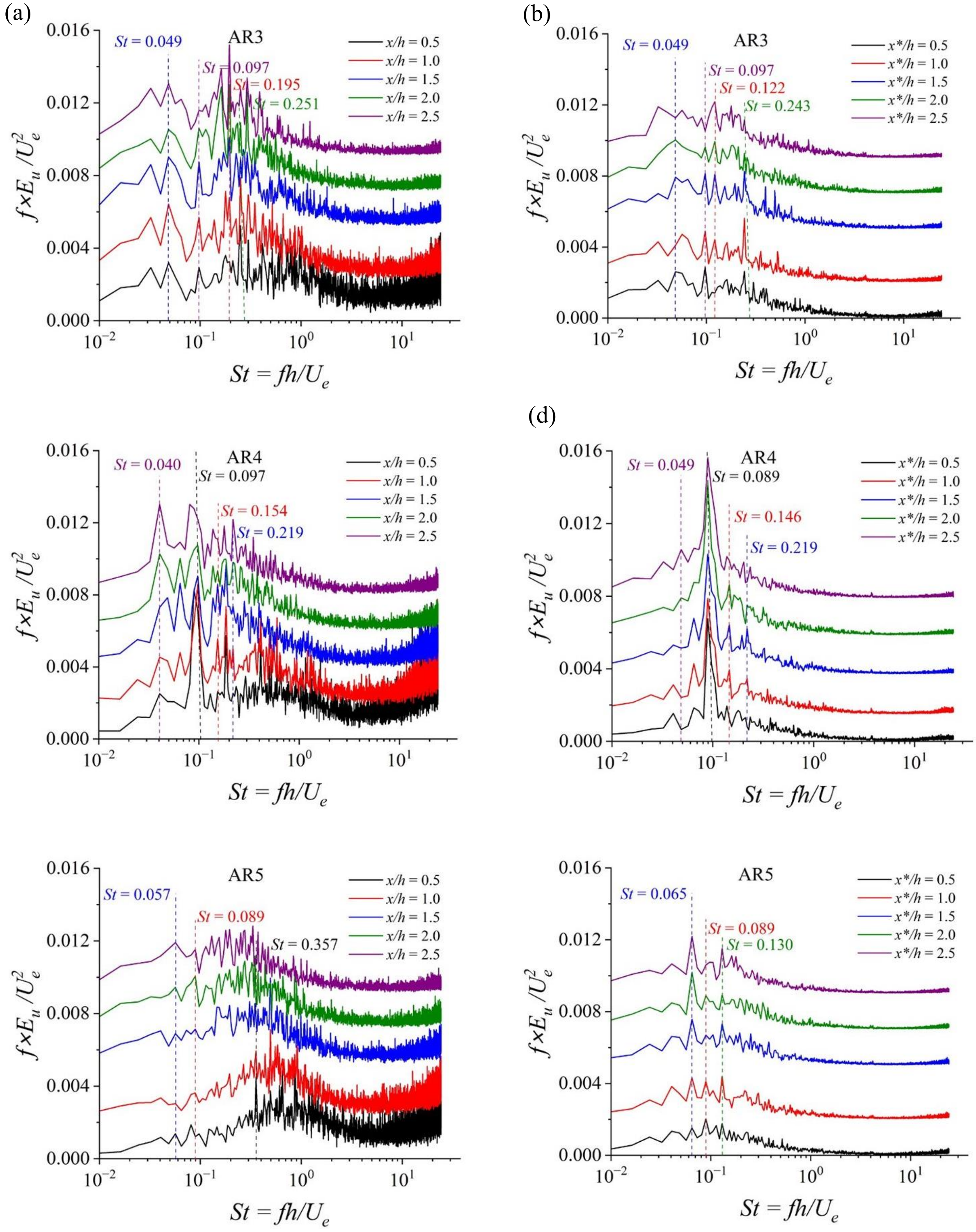

Figure A.15 Pre-multiplied energy spectra of u' along the mean streamline for (a, b) AR3, (c, d) AR4, and (e, f) AR5.

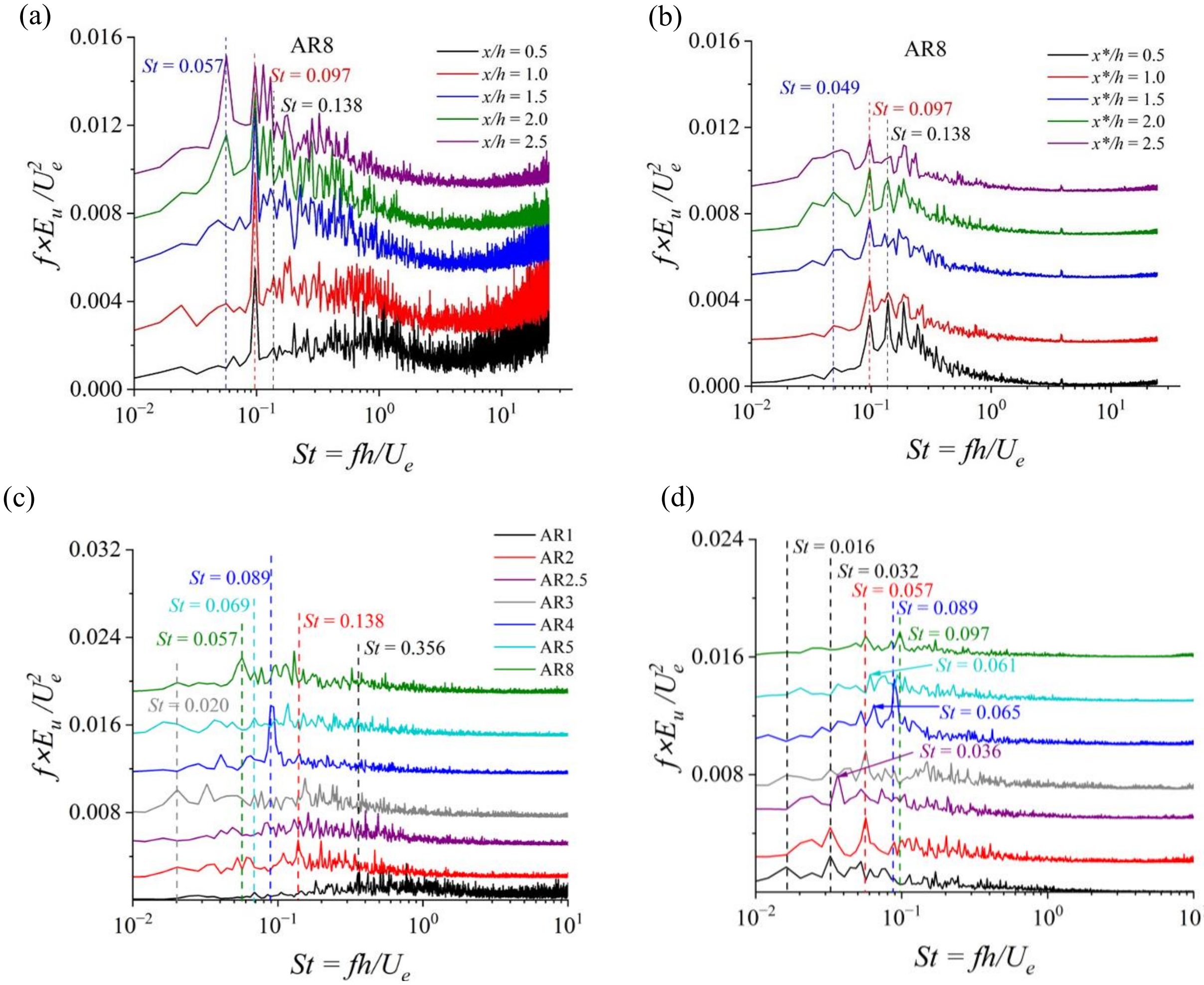

Figure A.16 Pre-multiplied energy spectra of u' (a, b) along the mean streamline for AR8, and (c, d) at maximum $\overline{v'v'}$ on the cylinder, and in the wake, respectively, for all aspect ratios.

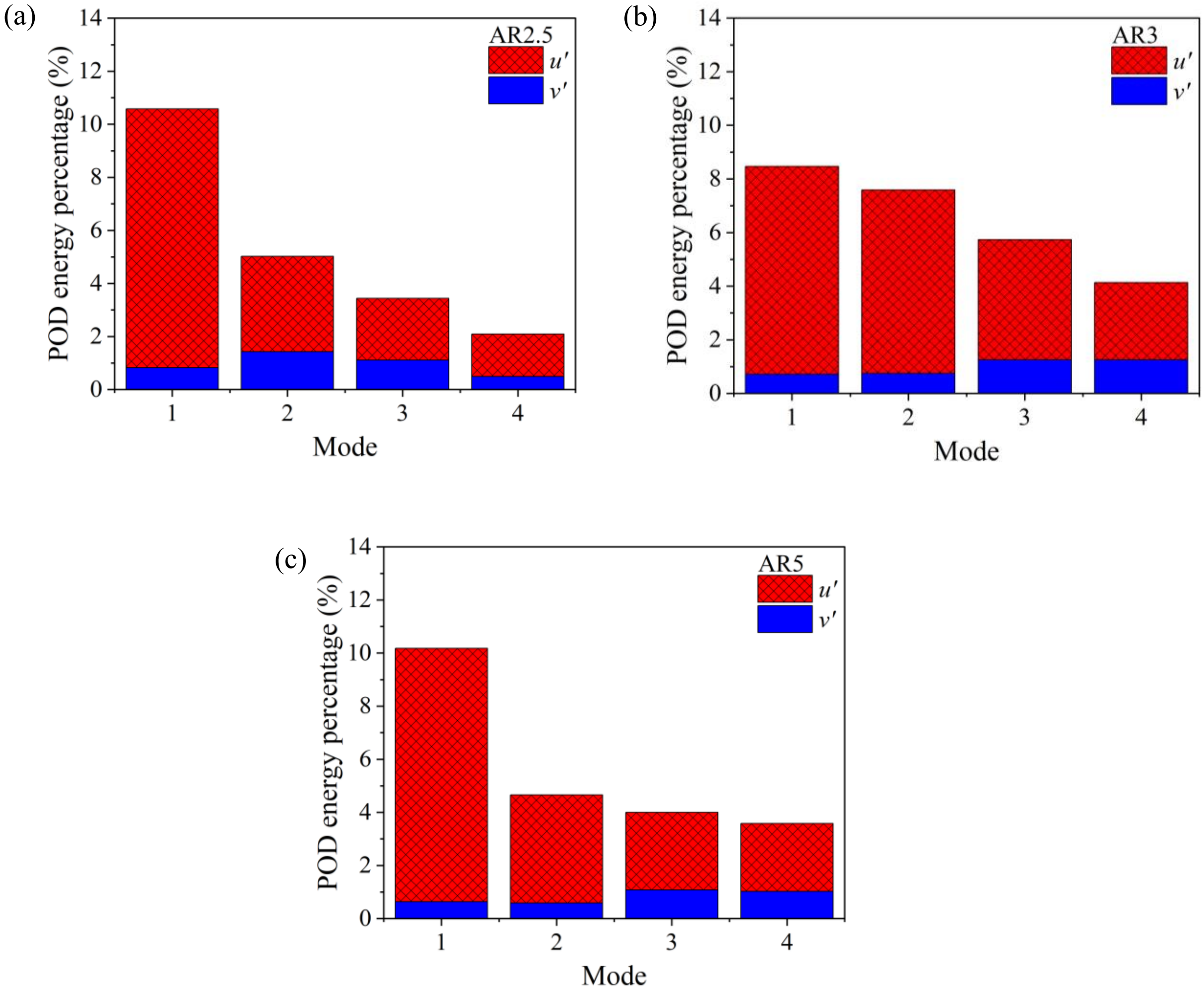

Figure A.17 Relative contribution of streamwise and vertical velocity fluctuations to the total turbulent kinetic energy for the first four modes of (a) AR2.5, (b) AR3, and (c) AR5.

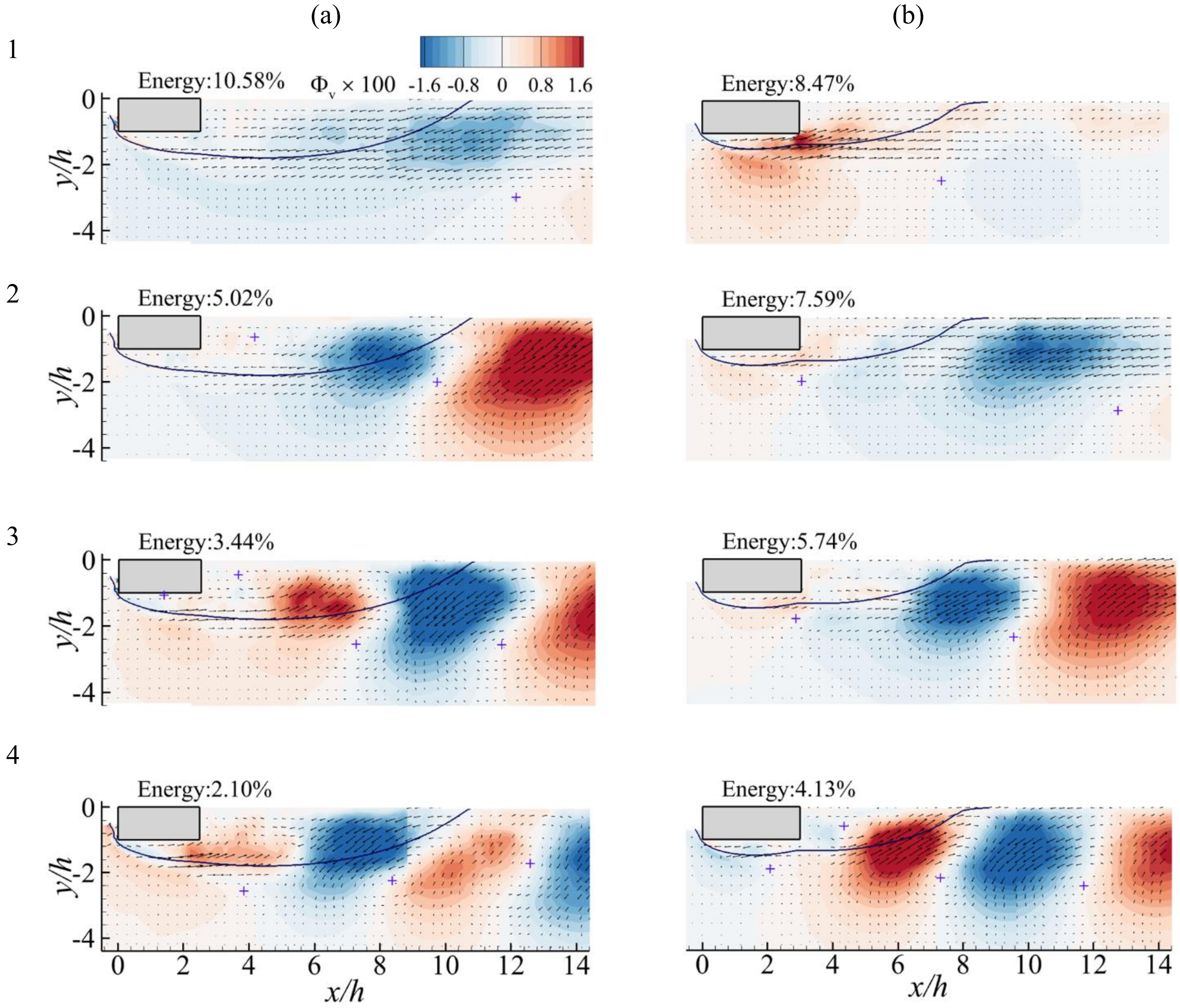

Figure A.18 Contours of the first four spatial POD modes of the vertical velocity fluctuations superimposed with mean velocity streamline for (a) AR2.5, and (b) AR3. The (+) symbols mark the centres of the vortices in each mode.

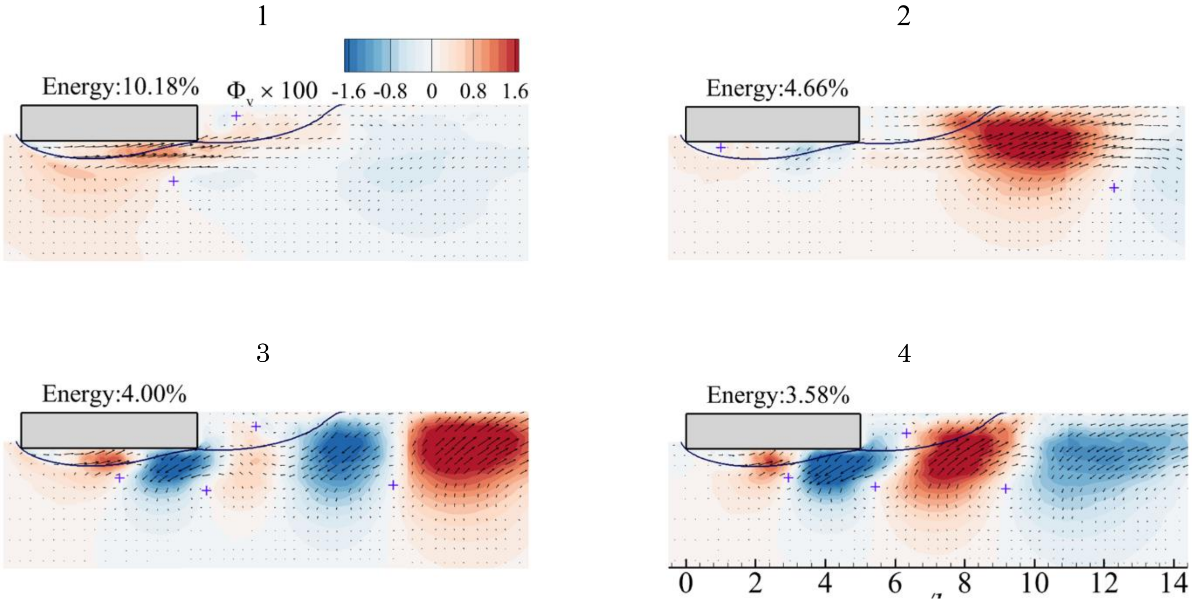

Figure A.19 Contours of the first four spatial POD modes of the vertical velocity fluctuations superimposed with mean velocity streamline for AR5. The (+) symbols mark the centres of the vortices in each mode.

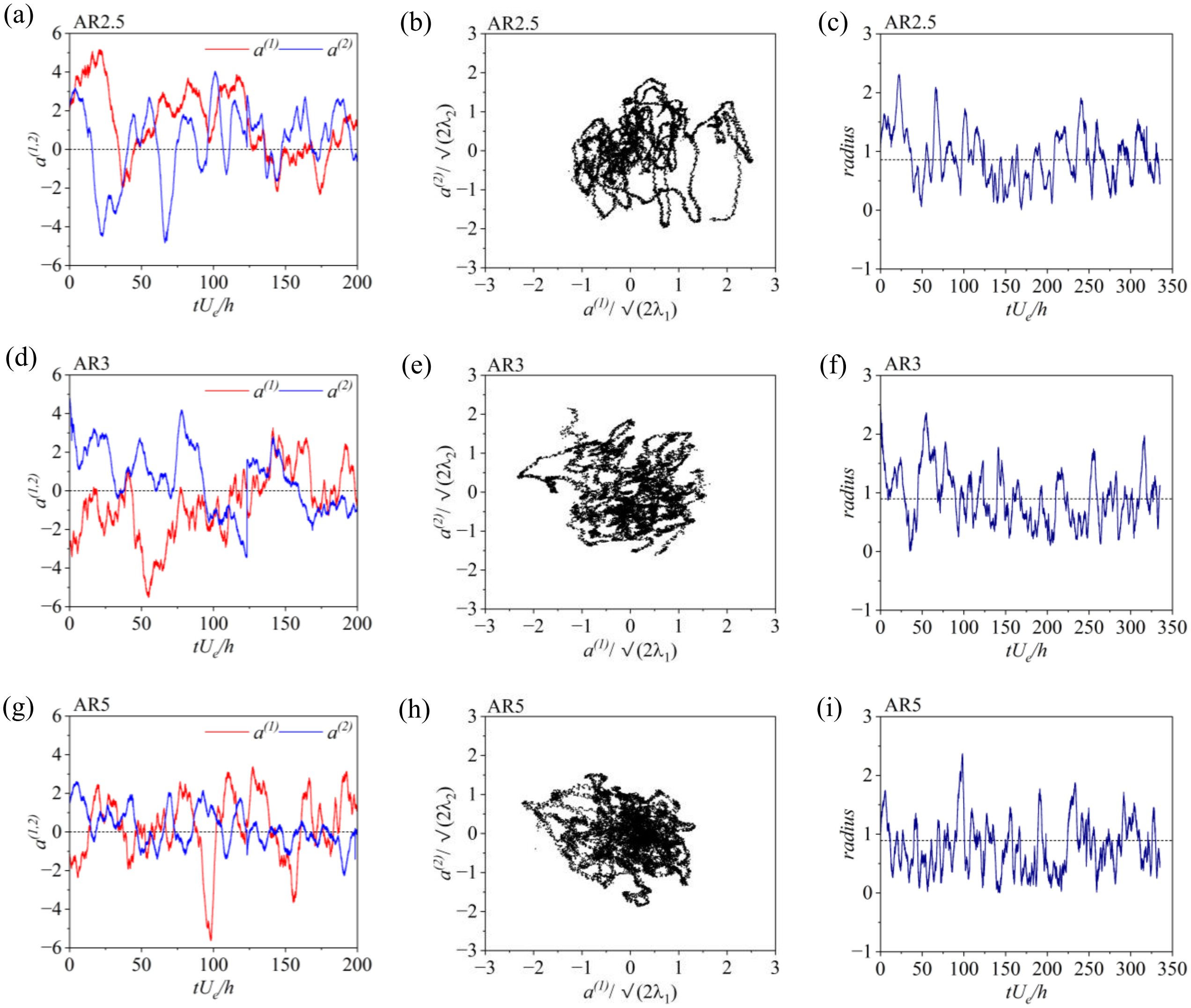

Figure A.20 Time signal of the mode coefficients (left), phase portraits (middle) and radius (right) of the first two modes of (a – c) AR2.5, (d – f) AR3, and (g – i) AR5.

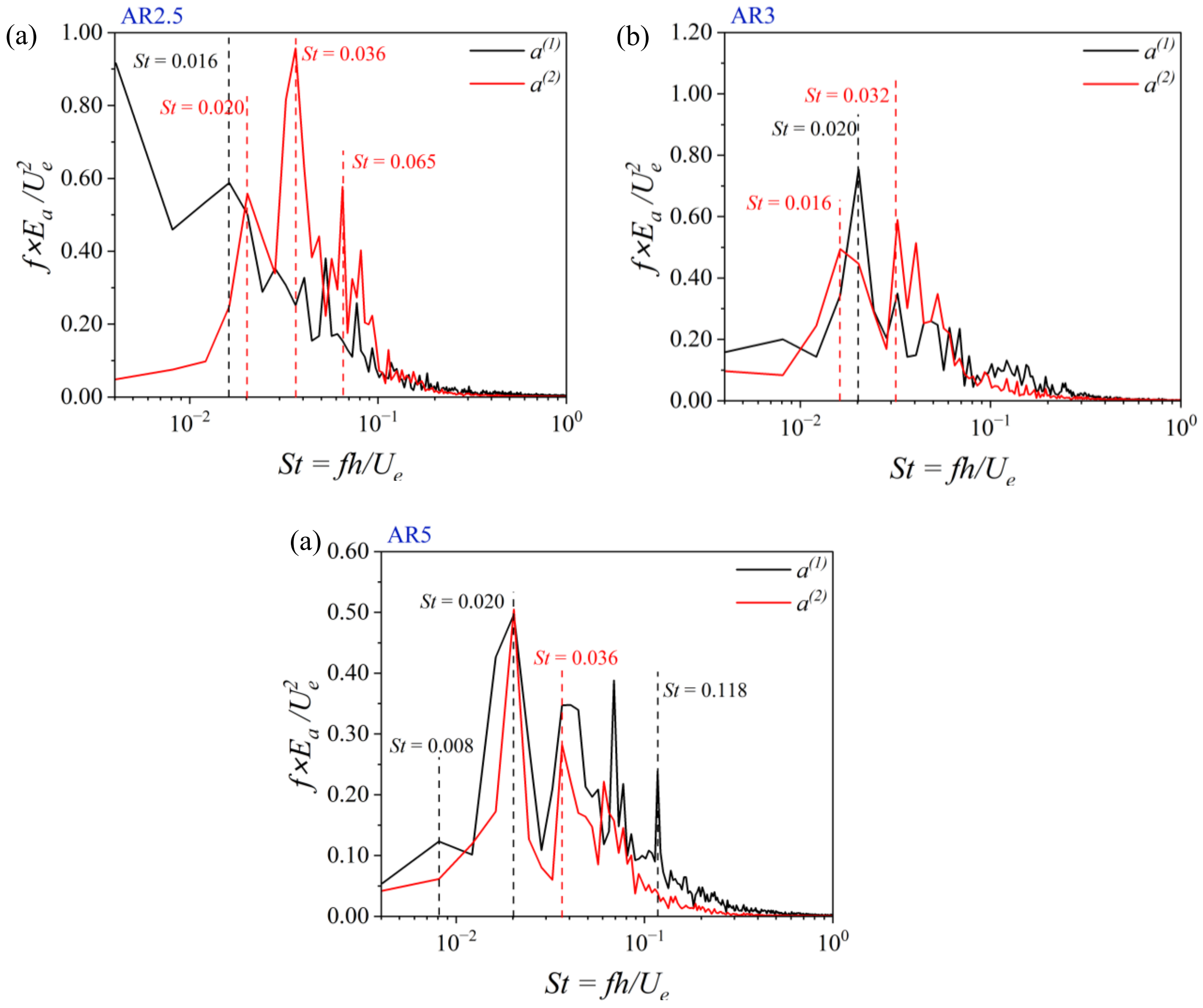

Figure A.21 Pre-multiplied energy spectra of first two POD mode coefficients of (a) AR2.5, (b) AR3, and (c) AR5.

Copyright Details

CCC Marketplace

This is a License Agreement between Kwasi Hyiah Agyei-Agyemang ("User") and Copyright Clearance Center, Inc. ("CCC") on behalf of the Rightsholder identified in the order details below. The license consists of the order details, the Marketplace Permissions General Terms and Conditions below, and any Rightsholder Terms and Conditions which are included below.

All payments must be made in full to CCC in accordance with the Marketplace Permissions General Terms and Conditions below.

Order Date	20-Aug-2024	**Type of Use**	Republish in a thesis/dissertation
Order License ID	1517331-1	**Publisher**	ELSEVIER INC.
ISSN	0142-727X	**Portion**	Chapter/article

LICENSED CONTENT

Publication Title	The International journal of heat and fluid flow	**Country**	United States of America
Article Title	Effects of aspect ratio on flow characteristics on free surface-mounted rectangular cylinders	**Rightsholder**	Elsevier Science & Technology Journals
Author / Editor	INSTITUTION OF MECHANICAL ENGINEERS (GREAT BRITAIN	**Publication Type**	Journal
Date	01/01/1979	**Start Page**	109535
Language	English	**Volume**	109

REQUEST DETAILS

Portion Type	Chapter/article	**Rights Requested**	Main product
Page Range(s)	1-17	**Distribution**	Worldwide
Total Number of Pages	17	**Translation**	Original language of publication
Format (select all that apply)	Print, Electronic	**Copies for the Disabled?**	No
Who Will Republish the Content?	Academic institution	**Minor Editing Privileges?**	Yes
Duration of Use	Life of current edition	**Incidental Promotional Use?**	No
Lifetime Unit Quantity	Up to 499	**Currency**	CAD

NEW WORK DETAILS

Title	Effects of aspect ratio on flow characteristics on free surface-mounted rectangular cylinders	**Institution Name**	University of Manitoba
Instructor Name	Kwasi Hyiah Agyei-Agyemang	**Expected Presentation Date**	2024-08-23

ADDITIONAL DETAILS

Order Reference Number	N/A	**The Requesting Person / Organization to Appear on the License**	Kwasi Hyiah Agyei-Agyemang

REQUESTED CONTENT DETAILS

Title, Description or Numeric Reference of the Portion(s)	10.1016	**Title of the Article / Chapter the Portion Is From**	Effects of aspect ratio on flow characteristics on free surface-mounted rectangular cylinders
Editor of Portion(s)	Agyei-Agyemang, K.H.; Essel, E.E.; Tachie, M.F.	**Author of Portion(s)**	Agyei-Agyemang, K.H.; Essel, E.E.; Tachie, M.F.
Volume / Edition	109	**Issue, if Republishing an Article From a Serial**	N/A
Page or Page Range of Portion	109535	**Publication Date of Portion**	2024-09-30

RIGHTSHOLDER TERMS AND CONDITIONS

Elsevier publishes Open Access articles in both its Open Access journals and via its Open Access articles option in subscription journals, for which an author selects a user license permitting certain types of reuse without permission. Before proceeding please check if the article is Open Access on http://www.sciencedirect.com and refer to the user license for the individual article. Any reuse not included in the user license terms will require permission. You must always fully and appropriately credit the author and source. If any part of the material to be used (for example, figures) has appeared in the Elsevier publication for which you are seeking permission, with credit or acknowledgement to another source it is the responsibility of the user to ensure their reuse complies with the terms and conditions determined by the rights holder. Please contact permissions@elsevier.com with any queries.

Marketplace Permissions General Terms and Conditions

The following terms and conditions ("General Terms"), together with any applicable Publisher Terms and Conditions, govern User's use of Works pursuant to the Licenses granted by Copyright Clearance Center, Inc. ("CCC") on behalf of the applicable Rightsholders of such Works through CCC's applicable Marketplace transactional licensing services (each, a "Service").

1) **Definitions.** For purposes of these General Terms, the following definitions apply:

"License" is the licensed use the User obtains via the Marketplace platform in a particular licensing transaction, as set forth in the Order Confirmation.

"Order Confirmation" is the confirmation CCC provides to the User at the conclusion of each Marketplace transaction. "Order Confirmation Terms" are additional terms set forth on specific Order Confirmations not set forth in the General Terms that can include terms applicable to a particular CCC transactional licensing service and/or any Rightsholder-specific terms.

"Rightsholder(s)" are the holders of copyright rights in the Works for which a User obtains licenses via the Marketplace platform, which are displayed on specific Order Confirmations.

"Terms" means the terms and conditions set forth in these General Terms and any additional Order Confirmation Terms collectively.

"User" or "you" is the person or entity making the use granted under the relevant License. Where the person accepting the Terms on behalf of a User is a freelancer or other third party who the User authorized to accept the General Terms on the User's behalf, such person shall be deemed jointly a User for purposes of such Terms.

"Work(s)" are the copyright protected works described in relevant Order Confirmations.